Summer 8-1-2017

Large Payload HIAD Systems: Development of Computationally Efficient Modeling Strategies and Structural Investigations

Andrew C. Young
University of Maine, andrew.c.young1@maine.edu

Follow this and additional works at: http://digitalcommons.library.umaine.edu/etd

     Part of the Structural Engineering Commons

LARGE PAYLOAD HIAD SYSTEMS: DEVELOPMENT OF

COMPUTATIONALLY EFFICIENT MODELING

STRATEGIES AND STRUCTURAL

INVESTIGATIONS

By

Andrew Young

B.S. University of Maine, 2011

M.S. University of Maine, 2013

A DISSERTATION

Submitted in Partial Fulfillment of the

Requirements for the Degree of

Doctor of Philosophy

(in Civil Engineering)

The Graduate School

The University of Maine

August 2017

Advisory Committee:

William G. Davids, Chair of Civil and Environmental Engineering, Advisor

Andrew J. Goupee, Assistant Professor of Mechanical Engineering, Advisor

Eric Landis, Professor of Civil Engineering

Roberto Lopez-Anido, Professor of Civil Engineering

F. McNeil Cheatwood, NASA Senior Engineer for Advanced Planetary Entry, Descent, and Landing Systems

LARGE PAYLOAD HIAD SYSTEMS: DEVELOPMENT OF

COMPUTATIONALLY EFFICIENT MODELING

STRATEGIES AND STRUCTURAL

INVESTIGATIONS

By Andrew Young

Dissertation Co-Advisors: Dr. William G. Davids, P.E.

Dr. Andrew J. Goupee

An Abstract of the Dissertation Presented

in Partial Fulfillment of the Requirements for the

Degree of Doctor of Philosophy

(in Civil Engineering)

August 2017

The hypersonic inflatable aerodynamic decelerator (HIAD) system under development by the National Aeronautics and Space Administration (NASA) has the potential to deliver the size of payloads to the Martian surface that will be necessary for future human-scale missions. An important step in realizing the promise of the HIAD system is to understand the structural behavior of this inflatable, textile, relatively compliant system. This is accomplished through structural testing and the development of structural modeling and analysis methodologies and tools. The structural modeling tools that have been developed to date utilize a continuum, shell-based finite element (FE) analysis approach. This methodology is capable of capturing the structural response of the HIAD system, but the models are time intensive to develop, difficult to parameterize and computationally intensive to run. In this dissertation a computationally efficient, beam-

based FE modeling approach is developed. The beam-based modeling methodology addresses the challenges that are encountered in analyzing an inflatable, textile system, such as the effect of internal inflation pressure, nonlinear material response, the loss of pretension due to inflation pressure during loading, and the large deformations that occur as a result of having relatively compliant system. Material models are developed for use with both shell and beam-based FE models. A three-dimensional, corotational, flexibility-based, fiber beam modelling methodology is developed for the inflatable, braided members with axial reinforcing cords. The modeling methodology and tools are applied to the analysis of component level inflatable tubes and the single torus structures that make up the HIAD system. Initial validation of the modeling strategy is accomplished by comparing model predictions and parallel experiments conducted by others at the University of Maine. The modeling tools are then extended to analyze the full HIAD system, composed of multiple, stacked tori with straps. The interactions between tori are accounted for, along with the strap sets that connect tori to each other and to the center-body of the decelerator. The modeling methodology is then further validated by comparison with results from pressure tub testing of a full HIAD system conducted by NASA researchers. Following model development and validation, the analysis methodologies are used to investigate structural response of full-scale HIAD devices. A number of configurations are investigated, including the influence of strap pretension and non-axisymmetric configurations and loading. The structural modeling tools are then coupled to optimization techniques to better understand the structural response drivers and demonstrate the feasibility of using the tools developed here in optimization studies.

ACKNOWLEDGMENTS

There are a number of people who must be thanked and acknowledged for their guidance, encouragement and inspiration in my pursuit of this PhD degree. I would like to first and foremost thank my advisors, Dr. Bill Davids and Andy Goupee for the constant support throughout my graduate career and the opportunities to pursue the research that we have been engaged in. Along with Josh Clapp, I am confident I could not have been part of a better research group. After nine years in the University of Maine's Civil and Environmental Engineering department I have been afforded opportunities that I would not have imagined. Thank you to the faculty.

I would like to particularly thank and acknowledge my family. My parents have provided continuous support throughout my educational career. The same is true of my parents-in-law. I hope to be able to pass on the same kind of support and encouragement that has been given to me. My wife and partner Kathleen has been a source of constant support and encouragement. There is no question that it would not have happened without her. And of course Anika and Charlie, who have made it worthwhile.

TABLE OF CONTENTS

LIST OF TABLES

LIST OF FIGURES

Chapter 1

INTRODUCTION

1.1   The HIAD Structure

The Hypersonic Inflatable Aerodynamic Decelerator (HIAD) structure under

development by the National Aeronautics and Space Administration (NASA) is designed

to decelerate a payload as it travels through the atmosphere of a planet during reentry

(Hughes et al. 2011; Johnson et al. 2016). The structure consists of multiple, slender,

inflatable torus members. The tori are stacked to form a cone shape (see Figure 1.1).

Each torus is strapped to adjacent tori while the innermost torus is strapped to the

relatively rigid center-body. Additional radial straps extend from the center-body to

outer tori. The outer cone, or fore side of the HIAD, is covered with a flexible thermal

protection system (TPS). The TPS protects and insulates the inflatable structure from the

extreme heating that is encountered during atmospheric reentry.
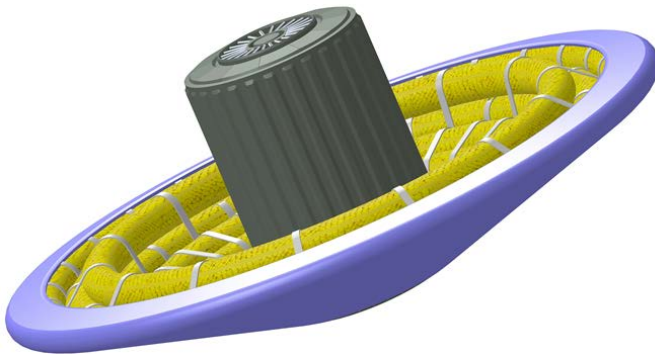
Figure 1.1. Conceptual rendering of the HIAD structure.

The individual torus members consist of a braided fabric shell covering a non-structural

gas barrier. Discrete, axial reinforcing cords are braided into the shell and provide the

majority of the axial and flexural rigidity of the tori. The inflatable system is deflated

and packed within the confines of a launch vehicle. The system in only inflated on the

way to the destination planet or before atmospheric reentry. The inflated cone creates a large surface area to slow down the payload as it travels through the atmosphere during reentry.

There are several advantages to using the HIAD system in place of a traditional rigid decelerator. Primarily, the inflatable system will be of significantly lower mass than a comparably sized rigid aeroshell, which can lead to decreases in fuel requirements. Further, the ratio of system mass to decelerator area is not constrained by size limitations imposed by the launch vehicle, and the inflated major diameter of the HIAD system can be much larger than the diameter of the launch shroud. For these reasons, the HIAD system has the potential to significantly increase payload delivery capacity from orbit to the surface of a planet with an atmosphere, such as Mars (Wright et al. 2012).

There has been a great deal of study on the structural response of the HIAD system including flight tests conducted in the earth's atmosphere (Wright et al. 2012) and large scale wind tunnel experimentation (Cassell et al. 2013). Finite element (FE) modeling of the HIAD system and components to date has utilized shell based continuum elements (Lindell et al. 2006; Li et al. 2015; Lyle 2014 and 2015) to model the shell and integral reinforcing cords. Although these models can accurately capture the response of the HIAD structure and components, they require significant development time and are computationally intensive to run.

The HIAD system is constructed from stacked, slender members, and is therefore a good candidate for modeling using beam-based FE models. Beam FE models are capable of accurately capturing the large displacement response of structural members with

composite cross-sections composed of materials having highly nonlinear constitutive relationships, and are very computationally efficient. In particular, flexibility- or force-based fiber-beam elements have been used successfully to model the highly nonlinear behavior of reinforced concrete frames composed of nonlinear materials that exhibit hysteretic behavior (Spacone et al. 1996a, 1996b). When material nonlinearities or plasticity are present in a frame analysis, finding polynomial displacement FE interpolation functions that correctly describe the displaced shape is quite difficult without a very refined discretization of the structure. On the other hand, it is straightforward to obtain force interpolation functions that satisfy equilibrium in the element exactly.

Inflatable structures present unique modeling challenges in handling internal pressure, material response and behavior after the fabric loses prestress, or "wrinkles". These modeling challenges must be overcome as the scale of the HIAD system (up to a 20 meter major diameter) makes them impractical to test experimentally. An important step in realizing the great potential of inflatable structures and the HIAD system is the development of effective and reliable modeling tools that will allow for the design space to be efficiently explored.

1.2 Research Objectives

The objectives of the current research are to:

- Improve our understanding of the structural behavior of slender, braided, inflatable members with discrete axial reinforcing cords by developing computationally efficient modeling methodologies and analyzing the inflatable structures;

3

- Develop methods for linking constitutive properties of the braid and cord with FE models;

- Develop computationally efficient, beam-based FE modeling and analysis methodologies appropriate for use with slender, inflatable members in general and the HIAD system in particular;

- Validate the FE modeling tools through comparison with experimental results from inflatable beam, torus and HIAD tests;

- Apply the FE analysis methodologies to the study of full-scale HIAD systems;

- Demonstrate the effectiveness of these beam-based FE analysis tools for exploring the HIAD design space and facilitating HIAD structural optimization studies.

Specific questions that the research addresses to achieve these objectives include:

- How can material test data of the compliant, inflatable system constituent materials be incorporated into various modeling methodologies?

- How can the braided, inflatable members with reinforcing cords that make up the HIAD system be efficiently modeled and analyzed?

- What drives the structural response of inflatable, braided members with axial reinforcing cords?

- How can the HIAD system be effectively modeled using a beam-based FE modeling methodology?

- How can the HIAD system be refined and optimized to achieve design goals and objectives?

1.3   Organization of Dissertation

This dissertation is organized into six chapters. The focus of Chapter 2 is the mechanics of the braided shell, and how to best incorporate material test data from the inflated, braided membrane and axial reinforcing cords into both shell and beam-based FE models. Material models must be handled very differently depending on the type of analysis that is being conducted.

In Chapter 3 a description of both shell and beam-based FE modeling of inflatable, braided members with discrete axial reinforcing cords located around the cross-section of the member is presented. Shell-based FE modeling tools were developed using the commercial FE code ABAQUS. The beam-based FE modeling tools were developed for the purpose of this research in the MATLAB environment. Although it would be possible to incorporate the beam-based FE modeling methodology into a commercial FE code, such as ABAQUS, developing the analysis tools in-house allowed for significantly more flexibility in the development process.

In Chapter 4 the shell and beam-based FE modeling tools are applied to the analysis of component level tests conducted at the University of Maine's Advanced Structures and Composites Center. The results of straight-tube, four-point-bend tests are compared to shell and beam modeling results. The beam-based FE modeling tools are also applied to the analysis of single torus load testing.

In Chapter 5 the beam-based FE modeling tools are extended to the analysis of a full HIAD structure. The HIAD modeling methodology is developed and the results of

analyses are compared to test data from static testing of a HIAD device previously conducted by NASA.

In Chapter 6 the beam-based FE modeling tools developed in Chapter 3 and validated in Chapter 4 and Chapter 5 are applied to the analysis of full-scale HIAD structures. The influence of strap prestress is investigated and compared to a simplified modeling approach that does not require the solving of an inverse problem in order to put the HIAD in the correct prestressed state. The structural response of 16.7 meter major diameter HIAD structures, with and without an aerodynamic tab, is investigated in order to assess the structural impact of tab loading on the system and demonstrate the use of the modeling tools with non-axisymmetric structural configurations and loading. A 12 meter HIAD structure is investigated. The baseline design is considered and the analysis tools that have been developed are coupled with structural optimization techniques in order to refine the system and understand the design sensitivities.

Finally, Chapter 7 provides a summary of the research that was conducted for this dissertation along with some conclusions. Potential areas of future research and logical extensions of the modeling and analysis methodology and tools are also discussed.

Chapter 2

BRAID MECHANICS AND MATERIAL MODELS

This chapter includes details on the response of the braided shell and the axial reinforcing

cords that make up the cross-section of the inflatable members. Netting theory, which

explains the axial response of a braided, inflatable tube, is explained in detail. Novel

methods are developed for the determination of effective braid and cord constitutive

models from independent tests that are suitable for direct implementation in shell and

beam FE models.

2.1   Braid Mechanics

The shell of the slender, inflatable members that make up the beams and tori that are

utilized in the current research is composed of braided Technora fabric tows, as shown in

Figure 2.1. An impermeable polyurethane membrane layer is included on the inside of

the braided shell to make the assembly airtight.

Figure 2.1. Detail of braided shell.

Understanding the response of the braided shell is a critical step in understanding the response of the inflatable members that will be discussed in more detail in subsequent chapters. As a thin-walled cylinder is inflated, the shell is put into the well-known stress state where the hoop stress (σ_L) is twice that of the longitudinal stress (σ_L), or

$$\sigma_L = \frac{pr}{2t},$$

Equation 2.1

and,

$$\sigma_H = \frac{pr}{t}.$$

Equation 2.2

The radius of the cylindrical pressure-vessel is r, the internal inflation pressure is p and the shell thickness is t.

Neglecting the compliant adhesive that bonds the braid fibers, the braided shell is composed of off-axis fibers that are only capable of carrying longitudinal stress. Therefore, only one equilibrium braid angle can stably accommodate the specific stress state of an inflated cylinder without any axial restraint. When axial constraint is present (as provided by reinforcing cords, straps or mechanical constraint from a load-frame), the percentage of the pressure resultant carried by the braid and the restraint can be calculated directly as a function of braid angle. Netting theory is used to describe the stress state of the braided shell and to calculate quantities such as the equilibrium braid angle and percentage of force that is accommodated by the axial restraint. Netting theory principles have been applied to other applications such as pneumatic actuators and airbags (Davis and Caldwell 2006). Others have derived the fundamental netting theory equations (Zu 2012; Evans and Gibson 2002) by considering the biaxial stress state of the braided shell and applying stress transformations in order to determine the critical braid

8

angle and percentage of axial force that must be accommodated by axial restraint. Those

same quantities are derived below in a simplified and intuitive manner using a unit cell

approach.

2.1.1   Critical Braid Angle

A unit cell of braid is considered in the derivation of the critical braid angle for a

cylindrical pressure vessel made of a braided fabric. Figure 2.2 illustrates the braid unit

cell. The individual fibers form a parallelogram oriented at an angle β measured from an

axis aligned with the longitudinal axis of the cylindrical pressure vessel. Also shown is

the origin of the reference coordinate system and the longitudinal (L) and hoop (H) axes

that will be used in subsequent calculations. The arbitrary length of a fiber tow is l. The

fibers are assumed to be capable of only accommodating tensile forces and are able to

freely rotate at all joints.
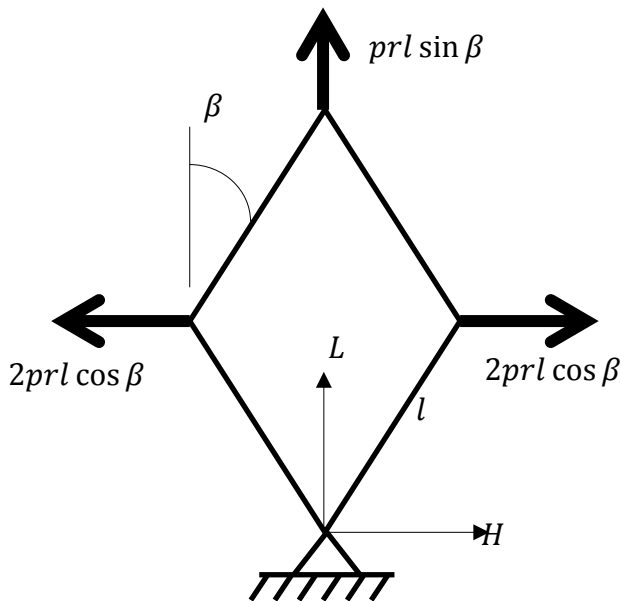
Figure 2.2. Braid unit cell.

The longitudinal and hoop force resultants are calculated using the tributary width and height of the unit cell and the shell stress (Equation 2.1 and Equation 2.2),

$$F_L = \frac{pr}{2} 2l \sin \beta = prl \sin \beta, \qquad\qquad \text{Equation 2.3}$$

and,

$$F_H = pr2l \cos \beta = 2prl \cos \beta. \qquad\qquad \text{Equation 2.4}$$

Note that membrane quantities are utilized throughout. All shell stress quantities, along with all shell moduli E_L, E_H and G_{LH}, are assumed to be pre-multiplied by the shell thickness, giving units of force per length. Likewise, all shell cross-sectional areas include a pre-multiplication by the shell thickness, giving units of length. Using membrane quantities allows for the thickness of the shell to be removed from all calculations, which will be done consistently throughout this document.

The free body diagram shown in Figure 2.2 is only in a state of stable equilibrium at one braid angle. In order to calculate this braid angle the principle of virtual work is applied. The coordinates of the longitudinal and hoop pressure resultants are determined as a function of the braid angle,

$$y_L = 2l \cos \beta \qquad\qquad \text{Equation 2.5}$$

and,

$$x_H = l \sin \beta \qquad\qquad \text{Equation 2.6}$$

The variation of the coordinate locations with a virtual change in braid angle can then be determined,

$$\delta y_L = -2l \sin \beta \, \delta\beta \qquad\qquad \text{Equation 2.7}$$

and,

$$\delta x_H = l \cos \beta \; \delta\beta \hspace{4cm} \text{Equation 2.8}$$

The principle of virtual work states that the sum of all forces acting on a body is zero for

any virtual displacement (e.g., see Hibbeler 2016), or for the current system,

$$\delta U = 0 = F_L \delta y_L + 2F_H \delta x_h. \hspace{3cm} \text{Equation 2.9}$$

Substituting in Equation 2.3, Equation 2.4, Equation 2.7 and Equation 2.8 yields,

$$prl \sin \beta \left(-2l \sin \beta \; \delta\beta\right) + 2(2prl \cos \beta)\left(l \cos \beta \; \delta\beta\right) = 0. \hspace{1.5cm} \text{Equation 2.10}$$

Simplifying and solving for β provides the well-known netting theory result for the

critical, equilibrium braid angle, $\beta = \tan^{-1} \sqrt{2}$, or approximately 54.7°.

Without axial restraint the braid will return to the critical braid angle when pressurized.

This behavior is taken advantage of by utilizing braid angles greater than the critical braid

angle, and including axial reinforcing in the form of braided Technora cords. Once

pressurized the axial reinforcing cords are tensioned, preventing the braid angle from

changing and giving the inflated member some degree of axial and bending rigidity. The

amount of pretension that the axial reinforcing members accommodates can also be

calculated using a unit cell.

2.1.2 Pretension of Reinforcing Members

Another braid unit cell is shown in Figure 2.3, below. Also shown in Figure 2.3 is an

axial reinforcing cord that restrains the braid from deforming significantly. The same

longitudinal and hoop pressure resultants are included as in Figure 2.2.
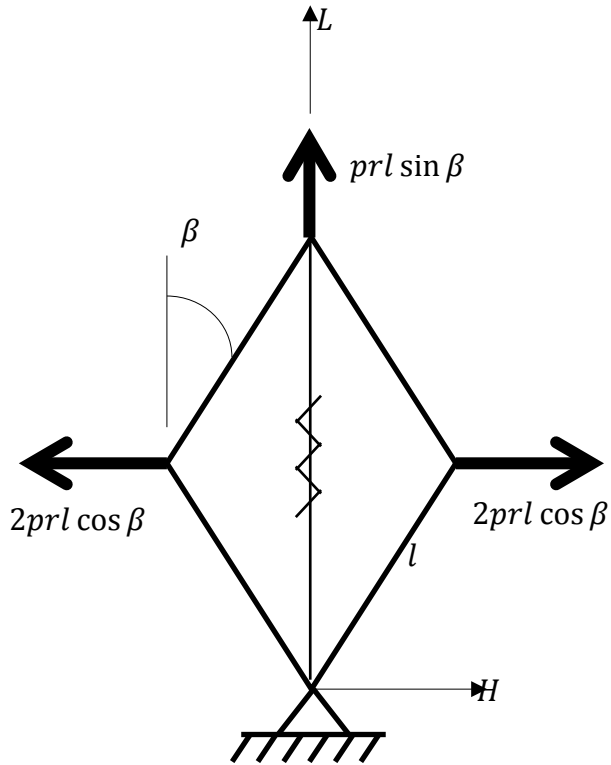
Figure 2.3. Braid unit cell with axial reinforcing.

The force in a fiber can be calculated using statics and by taking a cut that includes the

hoop resultant force and the internal tensile force of two fibers, (Figure 2.4, below).
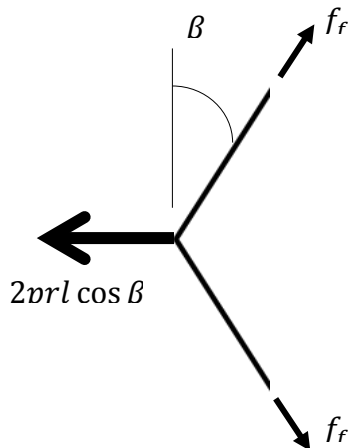
Figure 2.4. Free body diagram with hoop resultant force and internal fiber tow tensile

force.

12

Enforcing static equilibrium in the hoop direction yields,

$$\sum F_H = -2prl \cos\beta + 2f_f \sin\beta = 0.$$

Equation 2.11

Solving for the force in the fiber,

$$f_f = prl \frac{\cos\beta}{\sin\beta}.$$

Equation 2.12

With the fiber tension known a second cut including the longitudinal resultant force, fiber tows and axial reinforcing cord can be taken, as in Figure 2.5.
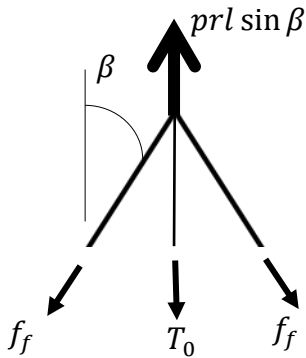
Figure 2.5. Free body diagram with longitudinal resultant force, internal fiber tow tensile force and cord force.

Static equilibrium can then be enforced in the longitudinal direction,

$$\sum F_L = prl \sin\beta - 2prl \frac{\cos\beta}{\sin\beta} \cos\beta - T_0 = 0.$$

Equation 2.13

The force in a cord, T_0, can be solved for,

$$T_0 = prl \left(\sin\beta - 2 \frac{\cos^2\beta}{\sin\beta} \right).$$

Equation 2.14

13

The arbitrary length of the fibers in a unit cell can be calculated as a function of the geometry of the pressurized cylinder and the number of reinforcing cords that are utilized (m) on the cylindrical cross-section of the member,

$$2l \sin \beta = 2\pi r \left(\frac{1}{m}\right),$$ Equation 2.15

or,

$$l = \frac{\pi r}{m \sin \beta}.$$ Equation 2.16

The quantity l can then be substituted into Equation 2.13,

$$T_0 = \frac{p \pi r^2}{m}(1 - 2 \cot^2 \beta).$$ Equation 2.17

The results yield the well-known netting theory expression for the force in an axial reinforcing cord as a function of the pressure resultant and braid angle (Zu 2012).

2.1.3   Netting Theory and the Shell Constitutive Relationship

It is also possible to relate netting theory results to Hooke's Law for an orthotropic membrane in a state of biaxial, plane stress. While netting theory can be used to describe the stress state of a pressurized braided shell, it cannot be used directly in the shell-based FE modeling of the pressurized membrane as any sort of material model. Relating netting theory to Hooke's Law will serve as a link between the two analysis types.

The starting point is to consider a pressurized cylinder made up of a thin, orthotropic membrane. Axial forces (F_{Hooke}) are developed as a result of restraining the pressurized shell longitudinally (at the desired braid angle) and keeping the shell in a state of equilibrium, as shown in Figure 2.6.
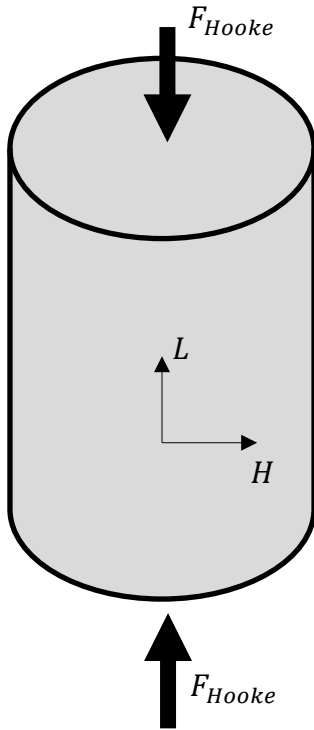
Figure 2.6. Pressure vessel with restraining forces.

Hooke's Law, a constitutive relationship for an orthotropic material, is used to relate the

strain in the material to the stress in the material,

$$\varepsilon_L = \frac{\sigma_{LL}}{E_L} - \nu_{LH} \frac{\sigma_H}{E_H}.$$
<div align="right">Equation 2.18</div>

The modulus of elasticity in the longitudinal and hoop directions are E_L and E_H,

respectively. The Poisson's ratio in the longitudinal and hoop directions is ν_{LH} and the

longitudinal and hoop stress in the restrained, pressurize cylinder are σ_{LL} and σ_H,

respectively. Two subscripts are used for the longitudinal stress to differentiate it from

Equation 2.1.

Next, equations of equilibrium are applied to the restrained pressure vessel. A cut

through the pressure vessel is shown in Figure 2.7, below.
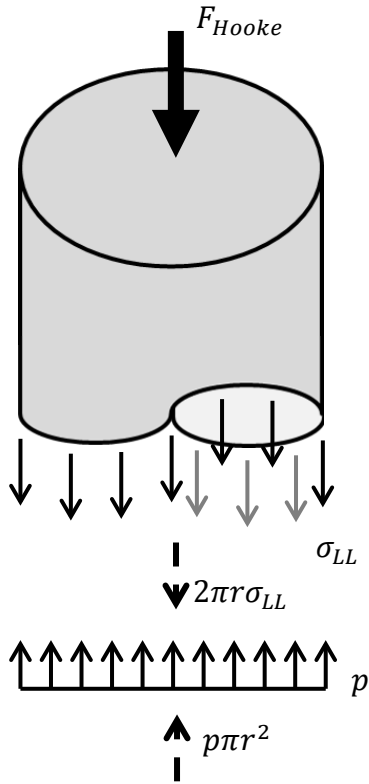
Figure 2.7. Pressure vessel equilibrium cut.

Summing forces in the longitudinal direction yields,

$$\sum F_L = p\pi r^2 - 2\pi r\sigma_{LL} - F_{Hooke} = 0,$$

Equation 2.19

and can be rearranged for σ_{LL},

$$\sigma_{LL} = \frac{rp}{2} - \frac{F_{Hooke}}{2\pi r}.$$

Equation 2.20

The compatibility equation is supplied with the assumption that the pressure vessel is

restrained from expanding or contracting in the longitudinal direction; therefore,

$$\varepsilon_L = 0.$$

Equation 2.21

Equation 2.2, Equation 2.18, Equation 2.19 and Equation 2.21 can be combined to form,

$$\frac{rp}{2E_L} - \frac{F_{Hooke}}{2\pi r E_L} - \frac{v_{LH}}{E_H}pr = 0. \qquad \text{Equation 2.22}$$

Recognizing that for an orthotropic material,

$$v_{LH} = \frac{E_L}{E_H}v_{HL}, \qquad \text{Equation 2.23}$$

Equation 2.22 can be rearranged to form,

$$F_{Hooke} = p\pi r^2(1 - 2v_{LH}). \qquad \text{Equation 2.24}$$

It is clear that Equation 2.24 is of the same form as Equation 2.17 (for $m = 1$, or one restraining member). Equating the two restraining forces relates netting theory and Hooke's Law and yields,

$$v_{LH} = \cot^2\beta. \qquad \text{Equation 2.25}$$

This expression will be used later in the chapter to determine the braided shell orthotropic properties (that satisfy netting theory), using tension-torsion test data presented by Clapp et al. (2016a).

2.2   Material Model Development

The inflatable members are composed of a braided shell, an impermeable, non-structural gas barrier and discrete axial reinforcing cords that are braided into the shell. An inflatable member, along with a detail of the braided shell and an axial reinforcing cord can be seen in Figure 2.8. Extensive material experimentation was performed as part of the University of Maine NASA EPSCoR program and is further described in Clapp et al. (2015), Clapp et al. (2016a) and Clapp et al. (2016b). Extracting information from experimentation for use as input into FE analyses is a critical a critical step in obtaining accurate analysis results.
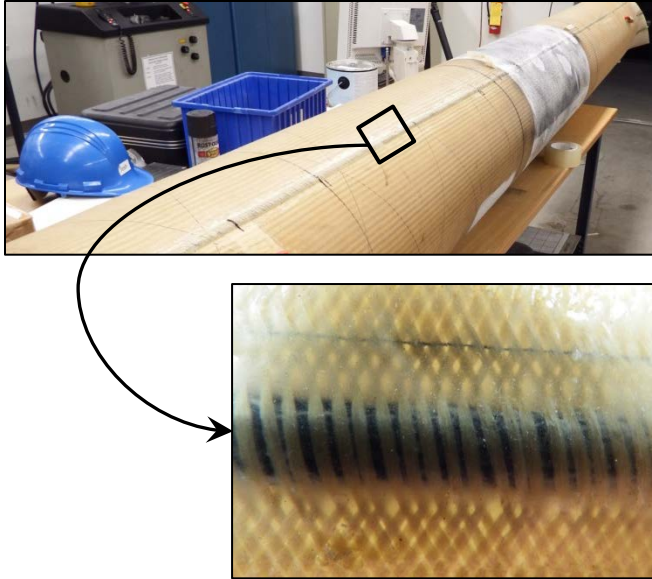
Figure 2.8. Straight, inflatable, braided tube with integral reinforcing cord detail.

2.2.1 Inflatable Shell Material Model

The inflatable shell material model must be handled very differently depending on whether a shell-based FE model or a beam-based FE model is under development. In both model types the work done by the internal inflation pressure undergoing a volume change must be accounted for. This can be accomplished by using pressure follower loads, as in the case of a shell-based FE model, or by integrating the pressure volume-change component of work into the constitutive relationship of the shell, as in the case of beam-based FE modeling.

2.2.1.1 Shell-Based Finite Element Model Properties

The primary results of tension-torsion testing (Clapp et al. 2016a) were reliable measurements for the longitudinal stiffness (E_L) and the in-plane shear stiffness (G_{LH}) of the fabric membrane. However, incorporating the measured test data into a structural FE model of an inflated tube simulated as an orthotropic shell also requires both the stiffness

in the hoop direction (E_H) and the Poisson ratio (ν_{HL}) in the hoop and longitudinal plane. Accurate shell properties are critical model inputs. Although the axial and bending behavior of braided inflatable tubes with axial reinforcing cords are driven by the stiffness of the cords, the relative values of E_L, E_H and ν_{LH} drive the amount of pretension that the reinforcing elements experience due to inflation pressure and therefore strongly influences the axial and bending behavior of the inflatable members.

The Poisson's ratio, ν_{LH}, can be found directly by equating netting theory and Hooke's law for an orthotropic material and netting theory (Equation 2.25). Given E_L, G_{LH} and ν_{LH}, the hoop stiffness E_H must be calculated in order to have all stiffness parameters of the orthotropic stiffness tensor for use in a shell based FE analysis. Using lamination theory and straightforward, realistic assumptions about the braid and fiber behavior E_H can be estimated.

The braided fabric was idealized as a three-layer laminate. The inner lamina layer was the isotropic bladder with known properties determined from the independent experiments ($E = 9.6$ N/mm and $\nu = 0.44$, Clapp et al. 2016a). The braid was treated as two lamina having fibers oriented in the positive and negative β directions, respectively. The transverse stiffness of a fiber layer (E_2) was assumed to be essentially zero (the value $1.8 \cdot 10^{-4}$ N/mm was used for numeric stability), as a sheet of unidirectional fibers will not have any transverse stiffness. Likewise, the in-plane Poisson's ratio was set to zero as enforcing a tensile strain in a sheet of unidirectional fibers will not induce a transverse strain. The effective braid lamina properties, (E_1 and G_{12}) were found such that when

incorporated into a three ply laminate at the correct braid angle the laminate properties,

(E_L, G_{LH} and v_{LH}) matched test data and netting theory.

An optimization routine was employed with a two parameter objective function, F given

in Equation 2.26, to minimize the error between the predicted laminate properties, test

data and netting theory.

$$F(E_1, G_{12}) = \left(1 - \frac{E_L(E_1, G_{12})}{E_L}\right)^2 + \left(1 - \frac{G_{LH}(E_1, G_{12})}{G_{LH}}\right)^2$$

$$+ \left(1 - \frac{v_{LH}(E_1, G_{12})}{\cot^2(\beta)}\right)^2$$

Equation 2.26

Following the determination of the braid lamina properties E_1 and G_{12} via minimization

of F, the hoop stiffness of the braided tube E_H is easily computed from laminate analysis

using classical lamination theory. It is worth noting that while laminate properties could

be input directly into the FE model for analysis, it is often more convenient in practice to

obtain effective lamina properties, (E_1 and G_{12} for each braid lamina and the bladder

properties) and use them as FE model inputs. Defining the shell section as a laminate

consisting of multiple lamina at user-specified orientations allows the stresses and strains

in the FE model to be easily transformed to the fiber direction. Further, this facilitates

comparisons to published and tested fiber properties, which is of interest because it

permits the effects of braid geometry, de-crimping, and inter-tow friction to be estimated.

Extracting effective lamina properties also allows for the influence of the bladder to be

isolated.

Table 2.1 presents the results of the lamina optimization analysis for varying internal

inflation pressures and braid angles. The columns E_L and G_{LH} were taken from tension

20

torsion test data (Clapp et al. 2016a). E_1 and G_{12} were determine using Equation 2.26. E_H was forward-calculated using classical lamination theory and optimized lamina properties. The in-plane Poisson's ratio, ν_{LH}, was determined using netting theory from Equation 2.25.

Table 2.1. Calculated lamina and laminate properties for a braided, inflated shell at various inflation pressures and braid angles.

| Measured Braid Angle | Inflation Pressure (kPa) | Modulus (N/mm) | | | | | ν_{LH} |
		Apparent E_1	Apparent G_{12}	E_L	E_H	G_{LH}	
60.0°	3	267	0.8	12	81	104	0.33
59.5°	34	1424	1.5	14	109	549	0.35
59.6°	69	2016	1.9	15	120	773	0.34
59.7°	103	2439	1.9	15	123	931	0.34
59.8°	138	2868	2.7	17	142	1090	0.34
62.9°	3	278	1.9	14	132	96	0.26
64.7°	34	1197	2.7	15	255	363	0.22
64.7°	69	1970	2.1	14	253	594	0.22
64.7°	103	2521	2.1	14	258	759	0.22
64.7°	138	2877	2.1	14	261	865	0.22
70.9°	3	316	3.3	14	333	68	0.12
70.9°	34	1128	3.3	14	625	224	0.12
70.9°	69	1629	3.3	14	701	320	0.12
70.9°	103	2159	2.3	13	707	420	0.12
70.9°	138	2404	3.3	14	771	468	0.12

FE models of the tension-torsion test specimens (Clapp et al. 2016a), were generated to evaluate the effectiveness of the lamina properties. The models were analyzed in the commercial FE program ABAQUS (Hibbett et al. 2014). Quadratic shell elements were

used to model the fabric membrane. The ends of the tube were fully constrained while internal pressure was applied to the membrane by means of a distributed follower force. Lamina properties derived from bladder testing and tension-torsion test data (Table 2.1) were defined at the measured braid angle, and ABAQUS generated the effective orthotropic material properties using standard, built-in functionality for laminate analysis. The diameter of the tube was input from test specimen measurements. An analysis of the inflation process was performed to compare the fixed end reactions to test and theoretical values (Equation 2.17). The FE results agree well with measured reactions and netting theory, as can be seen in Figure 2.9.
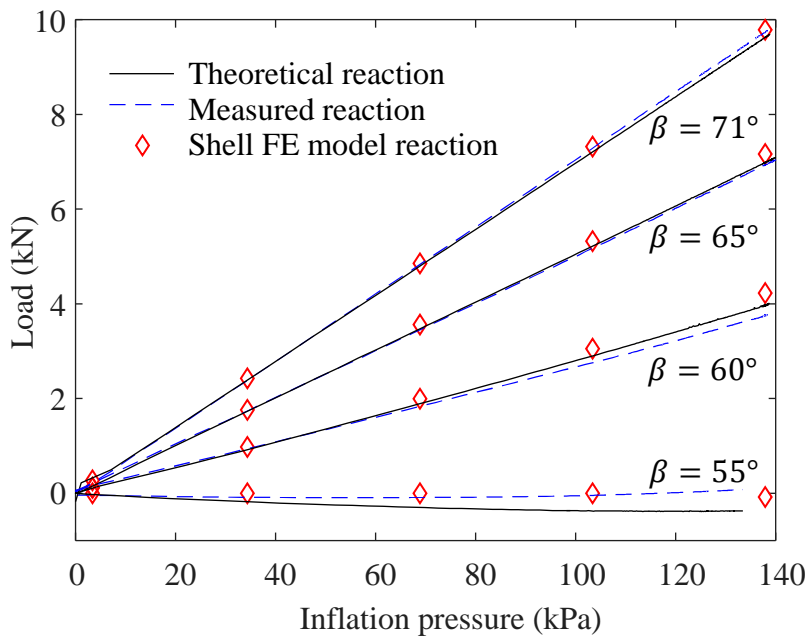
Figure 2.9. Comparison of measured and predicted pressure resultant forces (Clapp et al. 2016a).

2.2.1.2 Beam-Based Finite Element Model Properties

When analyzing the inflatable structures using a beam-based FE approach, the shell inputs must be handled differently. The longitudinal and shear modulus of the inflatable

23

shell were obtained from tension-torsion testing of the braided fabric shell in the pressurized state. In order to isolate the longitudinal stiffness of the shell the biaxial plane-stress state of the braided membrane was considered as,

$$E_L = \frac{1}{\varepsilon_L}(\sigma_{LL} - \nu_{LH}\sigma_H).$$

<div style="text-align:right">Equation 2.27</div>

The longitudinal strain (ε_L), as well as the longitudinal and hoop stress (σ_{LL} and σ_H), and the in-plane Poisson's ratio (ν_{LH}) were tracked throughout the duration of the tests of Clapp et al. (2016a) using photogrammetry techniques and the measured reaction of the pressurized cylinder on the load frame. When developing shell-based FE models of the inflatable system the orthotropic material properties derived from the tension-torsion testing must be utilized. With pressure follower forces and a pressurization step the membrane is put into the correct state of pretension and the gross axial stiffness of the braided shell is obtained because of the work done by the pressure loads. However, in the case of the beam-based FE analysis, using E_L directly will under-predict the shell's response in extension and bending because the shell is not in the correct prestressed state and the work done by the pressure follower forces is not accounted for. For use in the beam-based FE modeling methodology the stiffening effect of braid geometry changes must be added back into the extensional response to obtain the gross extensional stiffness of the inflated member. The changes in geometry are accounted for using netting theory.

The braided textile fabric serves primarily to carry the hoop stress induced by the internal inflation pressure while the longitudinal reinforcing cords restrain the inflated member longitudinally. To calculate the gross stiffness of the braided, inflatable member the compressive reaction force on the shell (usually accommodated by the axial reinforcing

cords) is calculated in two states using netting theory. The reaction is first calculated in

the initial, pressurized configuration,

$$F_0 = -p\pi r^2(1 - 2cot^2\beta),$$ Equation 2.28

and again after enforcing a small longitudinal strain ($\Delta\varepsilon_L$),

$$F_1(\Delta\varepsilon_L) = -p\pi r_1^2(1 - 2cot^2\beta_1) + 2\pi r E_L \Delta\varepsilon_L.$$ Equation 2.29

After the application of $\Delta\varepsilon_L$, the new radius and braid angle (r_1 and β_1, respectively), can

be calculated directly from the geometry of the braided shell assuming that the length of

braided fiber (l_F) does not change, as shown in Figure 2.10.
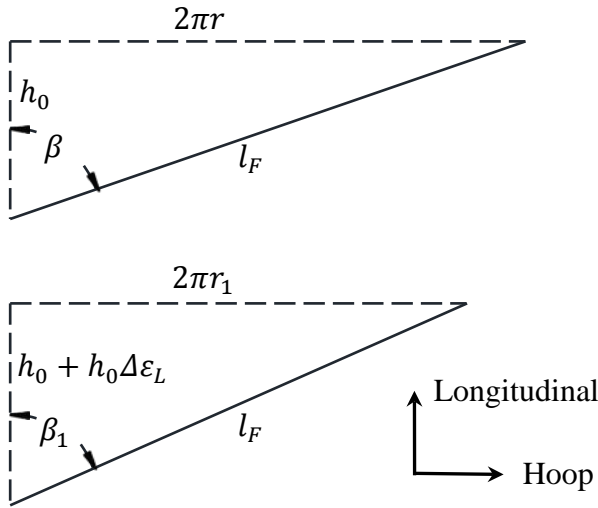
Figure 2.10. Geometry of an inextensible fiber in a braided pressure vessel before and

after the application of a small longitudinal strain (not to scale).

Finally, a secant modulus can be calculated using the initial and perturbed reaction force,

$$E_{gross} = \frac{(F_1 - F_0)}{2\pi r_0 \Delta\varepsilon_L}.$$ Equation 2.30

The gross extensional modulus is used in all beam-based FE analyses. Table 2.2, below,

presents the gross extensional stiffness calculated for two straight-tube specimens at

various inflation pressures. Also shown is the internal inflation pressure, tube geometry

and longitudinal shell stiffness that were used in the calculation of E_{gross} (Equation

2.30). The in-plane shear modulus (G_{LH}) is shown for completeness, although E_L, and

G_{LH} values presented in Table 2.2 are identical to the values found in Table 2.1.

Table 2.2. Shell properties for use with beam-based FE modeling tools.

Specimen		p	β	r	E_L	E_{gross}	G_{LH}
		(kPa)	(deg.)	(mm)	(N/mm)	(N/mm)	(N/mm)
Nominal 60°	**Straight Tube**	34	59.8	170.4	14	20	549
		69	59.7	170.4	15	27	773
		103	59.8	170.7	15	33	931
		138	59.8	170.8	17	41	1090
Nominal 71°	**Straight Tube**	34	70.6	169.0	14	16	224
		69	70.6	169.0	14	18	320
		103	70.6	169.3	13	20	420
		138	70.6	169.5	14	23	468

For the current analysis, the gross extensional stiffness could have been taken directly

from load-strain tension test data of the pressurized tube and normalized by the

circumferential length where the diameter of the tension torsion specimens and straight

tube specimens analyzed in later chapters are nominally equal. However, using netting

theory to calculate the gross extensional modulus allows for the effects of geometry to be

isolated so that orthotropic shell properties can be obtained for use in either a shell or

beam-based FE model. Further, the netting theory approach allows for the gross

properties of the inflated shell to be scaled. The gross stiffness of the inflated tube

obtained from testing cannot simply be normalized by the circumferential length and scaled to different diameter cross-sections without neglecting the influence of geometric changes, as was done in Brayley et al. (2012).

The braided shell is assumed to be capable of carrying loads even after the longitudinal strain in the shell cross-section due to bending has overcome the initial longitudinal strain due to inflation. The off-axis shell fibers are in tension even when the braided shell is in a state of longitudinal compression since the fibers must continue to accommodate the hoop stress due to inflation pressure. Experimental observations have confirmed that inflatable, braided tubes with axial reinforcing cords do not wrinkle during bending in the same manner as tubes with woven shells, but instead remain taut, even with longitudinal strains less than zero (Brayley et al. 2012; Clapp et al. 2016a).

2.2.2 Cord Model

In addition to the braided fiber shell and impermeable bladder, the inflatable members are also composed of axial reinforcing cords that are located at discrete locations around the member cross-section (see Figure 2.8). The stiffness contribution of the internal reinforcing cords drives the extensional and bending response of the inflatable members and understanding their response is important. From tension testing of the axial reinforcing cords, the cord force-strain relationship was observed to be nonlinear at low tensile strain and linear at high tensile strain. The cords are incapable of carrying any compressive force. Further, the cords exhibit hysteretic behavior, following different loading and unloading paths.

27

Figure 2.11 presents the results of cord testing on three pristine Technora cords and one

cord that was extracted from an inflatable member after it had experienced repeated load

cycling (the extracted cord was otherwise identical to the pristine cords in material and

geometry).
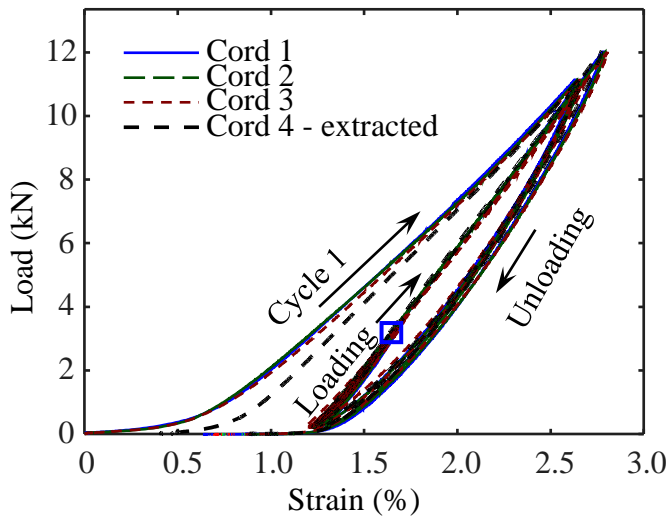
Figure 2.11. Cord force-strain relationship from tension testing of pristine cords and a

cord extracted from an inflatable member (Clapp et al. 2016a).

The cords were subjected to repeated load cycling up to the approximate maximum

expected cord load from straight tube testing (described later) and the expected load at

inflation pressure for a range of braid angles and inflation pressures. The response of the

cords was highly nonlinear at the beginning of the loading regime and zero strain is not

easily quantifiable. As such the curves in Figure 2.11 were shifted in order to all be

coincident with each other at 3.2 kN of load, shown with the blue square. The 3.2 kN

load level was chosen as the expected cord force for a 71° specimen with three cords at

138 kPa of inflation pressure and a nominal radius of 170 mm (see Equation 2.17). As

can be seen from Figure 2.11, the response is highly repeatable. Even for the case of the

extracted cord, after a single load cycle the load-strain response closely matches the pristine cords.

Also clear from Figure 2.11 is the cord hysteretic response. The unloading response was significantly stiffer than the loading response and the loading and unloading path creates an open loop. Incorporating both the loading and unloading response of the cords is necessary to capturing the load-deformation behavior of the inflatable, braided members with integrated axial reinforcing cords (Clapp et al. 2015, 2016b). With simple boundary conditions and loading regimes it is possible to know the load path that a particular cord on the cross-section will take *a priori*. Knowing the cord load path allows each cord to be independently pre-programed with the correct one-dimensional force-strain relationship.

2.2.2.1 Simplified Cord Model

The same cord model was used for both shell and beam-based FE modeling. The one-dimensional cord force-strain relationship was saved as a lookup table for interpolation within the FE routine for both shell and beam-based FE analysis methodologies. A unique cord force-strain relationship can be used for each cord. In the current study a force-strain relationship was used that allows cords that are above the neutral axis (NA) of bending, or that are expected to accommodate compressive forces to follow the cord unloading path, while cords that are below the NA of bending, or that are expected to accommodate tensile forces are allowed to follow the cord loading path. The third cord loading cycle was used in all analyses as it was repeatable. Utilizing the third loading cycle allowed consistency between analyses when specimens were loaded multiple times. The initial tensile force in each cord was calculated using netting theory (Equation 2.17).

29

Once the initial cord force was obtained a cord force-strain lookup table was generated

from tension test data of the reinforcing cord. At load levels above the initial cord force

the cord loading path was used. At load levels below the initial cord force a cord

unloading path was interpolated from unloading tension test data. Figure 2.12 shows a

representative cord force-strain relationship used as model input for a tube with three

cords, a 71^0 braid angle, 138 kPa of inflation pressure and a 170 mm minor radius. The

circle indicates the initial cord load (T_0) where the slope of the load-strain response

changes. The response of the cord below zero strain had a slope of essentially zero (an

axial rigidity (EA) of 444 N was generally used for numerical stability).
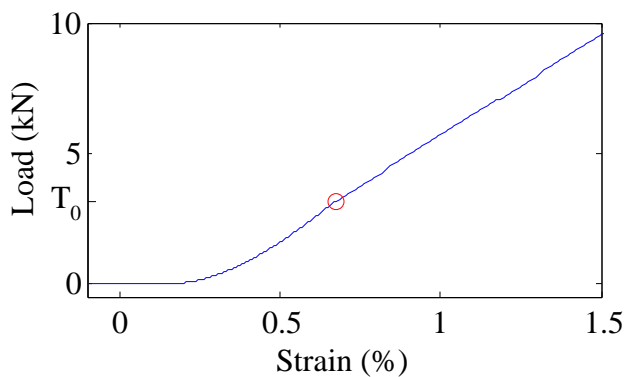
Figure 2.12. Cord force-strain relationship for an inflatable tube with three cords, a 71°

braid angle, 138 kPa of inflation pressure and a 170 mm minor radius.

2.2.2.2 Hysteresis Algorithm

When the path of cord loading cannot be predicted a-priori (as in the case of buckling or

analyses of more complex structures with multiple load cases that involve loading and

unloading), a cord model that tracks the strain history of the cord response and is able to

incorporate the observed hysteretic effects must be utilized. Analogous one-dimensional

models for elements exhibiting plastic or softening response have been developed by

others (e.g. see Taucer et al. 1991). Development of a cord hysteretic algorithm that could be implemented in future shell or beam based FE modeling approaches is presented here.

Preliminary inputs to the cord hysteresis algorithm are a cord loading curve and a cord unloading curve that are generated from test data. At any given step the model inputs include the current cord strain, whether the cord is loading or unloading (strain direction) and the location of previous points where the loading direction changed (pivot points). An unloading pivot point occurs when the load direction changes from loading to unloading. A loading pivot point occurs when the cord changes from unloading to loading. The output of the model is simply the current cord force and stiffness. Although the stiffness and hysteretic response of the cords could also be influenced by the loading rate, time-dependent material properties are not considered here.

The goal of the hysteresis algorithm development is to provide a way to reasonably estimate the current force and stiffness of a cord subjected to a loading history. The current hysteresis algorithm follows simple rules based on phenomena observed from cord testing to determine when an unloading or loading pivot point is created or removed, and how the calculation of the cord force and stiffness should be handled for various combinations of strain magnitude, strain direction and location of pivot points. A brief summary of the algorithm is as follows:

If: The cord strain is less than zero (COMPRESSION)

Then: The cord is linear elastic with a small stiffness

If: The cord strain is greater than zero, and

the cord strain is greater than all of the loading and unloading pivot points, and

the cord strain direction is greater than zero (TENSILE LOADING)

Then: Use loading curve

If: The cord strain is greater than zero, and

the cord strain direction is less than zero (TENSILE UNLOADING)

Then: Scale unloading curve between current unloading and loading pivot points

If: The cord strain is greater than zero, and

the cord strain is between the current loading and unloading pivot points, and

the cord strain direction is greater than zero (TENSILE RELOADING)

Then: The cord force-strain relationship is taken as a linear secant between

current loading and unloading pivots points

The creation of loading and unloading pivot points is controlled with the following rules:

Unloading Pivot Points

- A new unloading pivot point is created when the strain direction goes from positive to negative (when the cord starts to unload)

- An unloading pivot point is eliminated when the strain in the cord goes back above the unloading pivot point

- Unloading pivot points are reset if the cord goes into compression

Loading Pivot Points

- A new loading pivot point is created when the strain direction goes from negative to positive (when the cord starts to load)

- A loading point is eliminated when the strain in the cord goes above the corresponding unloading pivot point

- Loading pivot points are reset if the cord goes into compression

The updated cord force-strain relationship is a function of the current strain in the cord, whether the cord is loading or unloading and the location of pivot points, or where the cord load path changes directions (updated at each load step). Simple logic is utilized to determine what cord force-strain relationship is utilized. If the cord strain is less than zero the stiffness of the cord is zero (or a small number for numerical stability). If the cord is loading and the strain in the cord is greater than all previous unloading pivot points, then the cord follows a single loading curve derived directly from cord tension tests. If the cord is unloading a single unloading curve derived from tension tests is scaled from the unloading pivot point to zero strain. If the cord is loading and the cord

strain is less than a previous unloading pivot point, then the cord force-strain relationship

follows a secant line between the previous loading pivot point and unloading pivot point.

Figure 2.13 conceptually illustrates the cord hysteresis model. The cord starts at zero

strain and force and is loaded along the solid line. If the cord is unloaded at 3.16 kN of

load (unloading pivot point), the force-strain relationship would follow the dashed line

until the cord completely unloads. If the cord were to instead start reloading at 0.33 kN

of load (loading pivot point) the force-strain relationship would follow the dotted secant

line between the two pivot points. Once the force in the cord is greater than the

unloading pivot point the cord force-strain relationship would revert to the original

loading curve.
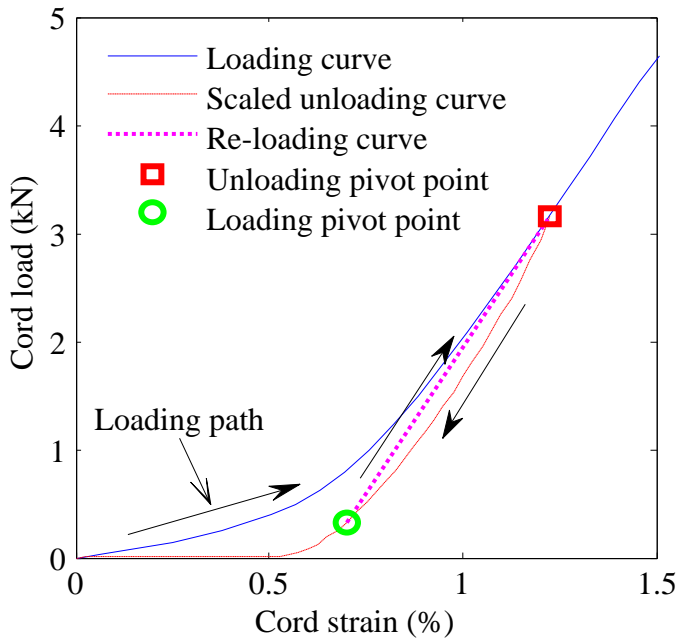
Figure 2.13. Illustration of cord hysteresis model including location of pivot points and

load path directions.

Using the above relatively simple rules it is possible to make comparisons with cord tests. Cords were subjected to repeated loading and unloading in a load controlled tensile test (Figure 2.11). Cord strain was measured by means of an extensometer. Since the hysteresis model requires cord strain as the input, the measured cord strain from the tension test was used directly to see if a reasonable cord force could be extracted.

The loading curve was taken as the force strain relationship for the first cycle of loading (up to the maximum recorded load, a linear, tangent extrapolation was utilized afterwards). The unloading curve was taking from the first cycle of unloading. Figure 2.14 shows the results of cord testing and a comparison with the cord hysteresis model. Even after the application of the first load cycle (where the model essentially utilizes the test output directly), the model accurately captures the load/unload response of the cord test.
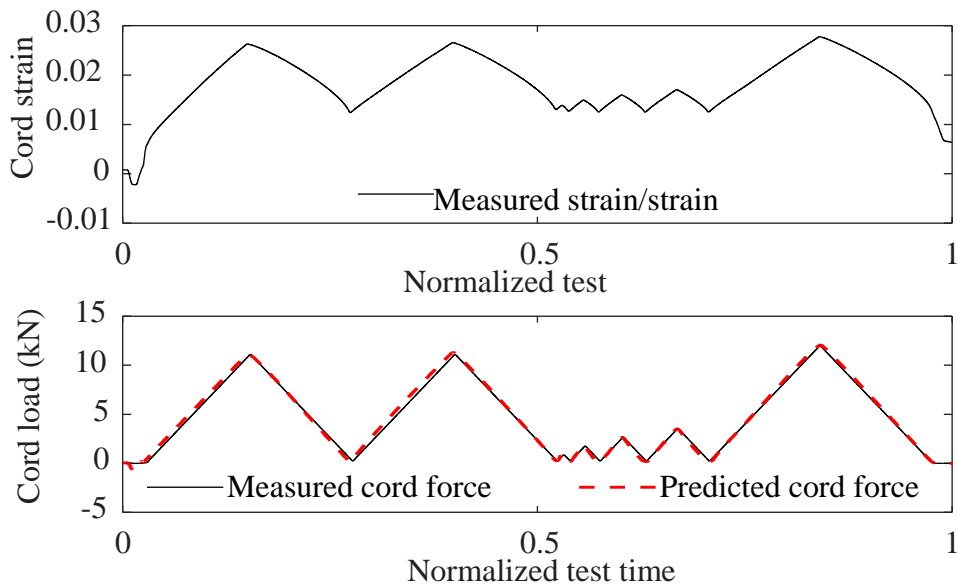
Figure 2.14. Cord hysteresis algorithm test results.

The force-strain response of the tested cord and hysteresis algorithm is shown in Figure 2.15.
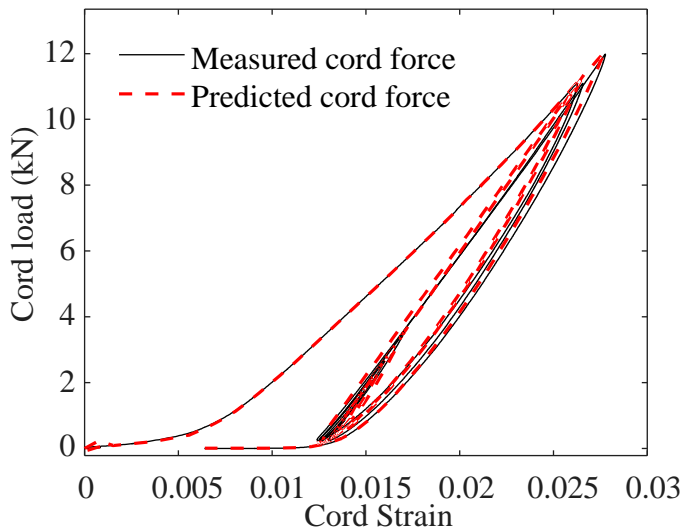
Figure 2.15. Cord test and hysteresis algorithm force-strain response.

The purpose of the cord hysteresis model is to provide a phenomenological means of predicting the cord response when subject to repeated cycles of loading. However, it may also be possible to predict the response of the cords by developing a sub-, or meso-scale, model of the braided members that includes all relevant geometry, fiber-tow stiffness and interaction between fibers. Such a model would likely require significant resources to develop and be computationally demanding. Eventually such an algorithm could be incorporated into the beam-based FE modeling methodology that is developed in later chapters via a sub-routine that would return cord force and stiffness given strain and strain history.

With a better understanding of the response of constituent materials that make up the inflatable members (braided shell and axial reinforcing cords), the response of the members can be analyzed. The shell and cord material models that were described here are used as inputs to both shell and beam-based FE analyses described in the following chapters.

Chapter 3

BEAM-BASED FINITE ELEMENT MODELING METHODOLOGY DEVELOPMENT

This chapter presents the development of a computationally efficient analysis

methodology for use with slender, braided, inflatable members with axial reinforcing

cords located at discrete locations around the member cross-section, and is based on

Young et al. (2017a). The modeling methodology is validated at the component (Chapter

4) and structure (Chapter 5) levels. The development of such an analysis methodology

will allow for the modeling of full-scale HIAD structures and HIAD optimization studies,

as described in Chapter 6.

3.1   Background

Pressurized beams, arches and tori are unique tensile structures and can be used in a

number of civilian, military and aerospace applications (Verge 2006; Brown et al. 2001;

Veldman and Vermeeren 2001). Inflatable, slender members can be packed into a

relatively small volume and deployed rapidly to create load carrying structures. Included

in this class of structures is the HIAD system.

There has been a great deal of study on the structural response of the HIAD system

(Hughes et al. 2011) including flight tests conducted in earth's atmosphere (Wright et al.

2012) and large scale wind tunnel experimentation (Cassell et al. 2013). Finite element

(FE) modeling of the HIAD system and components to date have utilized shell-based

continuum elements to model the inflatable shell and follower forces to model the

internal inflation pressure (Lindell et al. 2006; Lyle 2014, 2015; Li et al. 2015; Clapp et

al. 2015). Although these models can accurately capture the load-deformation response

of the HIAD structure and components, they require significant development time and are

computationally intensive to run, especially when including the contact interaction between inflatable members.

The HIAD system is constructed from stacked, slender members, and is therefore a good candidate for modeling using beam-based FE models. Beam FE models are capable of accurately capturing the large displacement response of structural members with composite cross-sections composed of materials having highly nonlinear constitutive relationships. In particular, flexibility- or force-based fiber-beam elements have been used successfully to model the highly nonlinear behavior of reinforced concrete frames composed of nonlinear materials that exhibit hysteretic behavior (Spacone et al. 1996a, 1996b). When material nonlinearities or plasticity are present in a frame analysis, finding polynomial displacement FE interpolation functions that correctly describe the displaced shape is very difficult without a highly refined discretization of the structure, leading to large computation times. On the other hand, it is straightforward to obtain force interpolation functions that satisfy equilibrium in the element exactly. The trade-off is that when using force-based interpolation functions an iterative procedure must be performed at the element level to ensure that the distribution of section forces at element integration points are compatible with the force interpolation functions. Further, the element stiffness matrix cannot be obtained directly, but must be determined through inversion of the element flexibility matrix and incorporated into the global stiffness matrix for subsequent global, stiffness-based FE iterations (Neuenhofer and Filippou 1997; de Souza 2000).

Inflatable structures present unique modeling challenges due to internal pressure, material response and behavior after the fabric loses prestress, or "wrinkles". Previous work on

inflatable, slender members has primarily focused on isotropic or orthotropic fabric shells without axial reinforcing cords. Cavallaro et al. (2003) investigated the mechanics of woven air beams. Le van and Wielgosz (2005) derived equations for the deformation of a thin walled beam with an internal inflation pressure subjected to stretching and bending and later (Le van and Wielgosz 2007) discretize the solution to develop a two dimensional, shear deformable beam finite element for an isotropic material. The work has been applied by Wang et al. (2009) to study the load deformation response of large scale inflatable space frames. Apedo et al. (2010) investigated the constitutive relationships of pressurized, orthotropic fabrics along with Nguyen et al. (2015). Elsabbagh (2015) developed a beam element for the analysis of isotropic inflatable members that are axisymmetric about the longitudinal axis.

Braided beams have been analyzed by others to a lesser extent. Brown et al. (2001) derived equations for the initial stiffness and wrinkling moment for braided beams while Veldman et al. (2005) developed a bending theory for braided beams with axial fibers located on the beam cross-section, as well as performed bending tests on vertically mounted cantilever beams past the onset of wrinkling. Davids and Zhang (2008) previously developed a beam finite element to analyze the in-plane response of inflatable, woven members. The element was extended to analyze the large displacement response of inflatable, woven beams and arches (Davids 2009), and braided members with discrete reinforcing straps bonded to the cross-section of the element (Brayley et al. 2012). The constitutive relationship of the beam cross-section was considered to be linear elastic, tension only and for members that carried combined axial load and bending moment, the bending response was interpolated from moment curvature relationships that were

developed for varying levels of axial load. In the case of Veldman (2005) and Brayley et al. (2012) the post wrinkling response on the inflatable, braided members with discrete reinforcing straps was modeled using parameters empirically derived from beam bending experimentation. In all cases only two-dimensional deformations were considered, neglecting in-plane and out-of-plane coupling that can occur due to even a small misplacement of the discrete reinforcing cords or small geometric imperfections of the inflatable members. Further, the treatment of coupling between axial and bending forces using pre-defined moment-curvature relationships as done by Davids (2009) and Brayley et al (2012) does not rigorously capture the effect of all deformations and stress combinations.

Significant challenges exist in modeling the structural response of braided, slender members with discrete, integral, axial reinforcing cords. Although the braided shell contributes minimally to the axial and flexural stiffness of the members prior to wrinkling, braid geometry and elastic properties are critical inputs to obtain the correct cord prestress and prestrain and to obtain the correct gross axial stiffness of the shell (Clapp et al. 2016a), including the effects of braid angle changes that occur during axial extension. The response of the discrete, axial reinforcing cords around the shell cross-section largely drives the axial and bending response of the inflatable member. In order to accurately model the response the nonlinear and tension only response of the cords must be taken into account along with the cord loading direction, whether loading or unloading (Clapp et al. 2015, 2016b). The three-dimensional response of inflatable members with discrete axial reinforcing cords around the shell cross-section is also critical; even small misalignments of the cords with the longitudinal axis or geometric

41

imperfections can drive out-of-plane deformations or buckling modes in more complex structures.

There is currently a need to develop a practical, computationally efficient FE modeling methodology employing beam elements that captures the three-dimensional, large displacement and materially nonlinear behavior of inflatable, braided, slender members with integral, axial reinforcing cords. Such a methodology will allow engineers to efficiently explore the HIAD structural design space and perform more formal optimization studies. In this chapter, such a methodology is developed that incorporates the effects of work done by pressure and volume on the inflatable system. The analysis methodology allows for the response of the members to be captured significantly past the point of initial wrinkling without the use of empirically derived parameters. Utilization of a three-dimensional corotational framework along with a flexibility-based fiber-beam element for the inflatable member allows for the full stress state of the member to be analyzed, including the axial, bending and torsional response. Coupling that occurs between the axial and bending response, as well as between in-plane and out-of-plane bending is captured.

3.2   Development of Analysis Methodology

A methodology to perform three-dimensional analyses on inflatable, braided, slender members with integral reinforcing cords using beam finite elements is presented. The element geometry within the corotational framework and the element state determination process are detailed. Details on the material constitutive relationships that are utilized in the modeling methodology were presented in Chapter 2.

3.2.1 Relevant Coordinate System and Geometry

The inflatable structures of interest have the potential to undergo large displacements and rotations, but exhibit only moderate strains of less than 5% under applied loads (Clapp et al. 2016b). As such, a three-dimensional corotational formulation is employed following Crisfield (1990). Figure 3.1 illustrates the global FE coordinate system (X, Y and Z) as well as the local element, or basic coordinate system (x, y and z) which does not include rigid body modes. In the corotational formulation the local element coordinate system translates and rotates with the element's rigid body motions and must be updated every global iteration. The nodal displacements are transformed to the local element coordinate system without rigid body modes, allowing for the element stiffness matrix and element forces to be calculated using the flexibility-based FE element formulation, discussed below. The element and geometric stiffness matrices, along with the element forces can then be transformed from the local to the global coordinate system including all translational and rotational degrees of freedom for assembly into the global stiffness matrix and internal force vector respectively. Further details on the formulation and derivation of the corotational formulation are omitted here but are thoroughly covered by others (Crisfield 1990, de Souza 2000), including the handling of successive rotations in three-dimensional space.
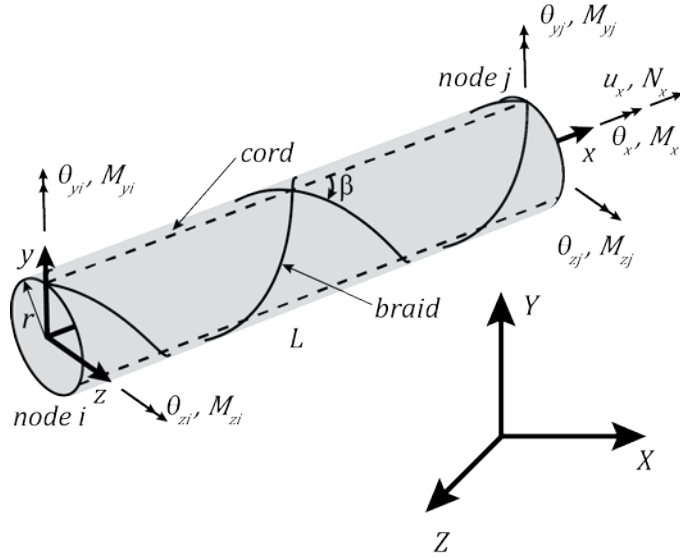
Figure 3.1. Global and local coordinate systems for a three-dimensional, inflatable, corotational beam element.

Figure 3.1 shows the initial shape of the element, including the radius of the member, r, and the element initial length, L. The initial shape is taken as the inflated state rather than the deflated or "natural" state. The inflation process is not considered here whereas the initial, inflated configuration is assumed to be known along with the material constitutive relationships in the pressurized, prestressed state. When analyzing curved members either a curved beam formulation or a sufficient mesh refinement using straight elements is required to accurately capture the response.

The element degrees of freedom of interest (q) are derived from the global displacements as detailed in Crisfield (1990) and are shown in Figure 3.1. The element degrees of freedom include the axial displacement, rotation about the z and y axes at nodes i and j and the rotation about the x axis, or

$$q^T = \left[u_x, \theta_{zi}, \theta_{zj}, \theta_{yi}, \theta_{yj}, \theta_x\right].$$
Equation 3.1

The element degrees of freedom correspond to the element forces, $\boldsymbol{Q}$, also shown in Figure 3.1,

$$\boldsymbol{Q}^T = \left[N_x, M_{zi}, M_{zj}, M_{yi}, M_{yj}, M_x\right].$$
<div align="right">Equation 3.2</div>

Figure 3.1 also illustrates the angle that the shell braid makes with the longitudinal axis (β), the location of generic cords on the element and the location of nodes i and j.

When modeling inflatable, braided members with integrated reinforcing cords an important consideration is the number and location of the reinforcing cords. The reinforcing cords are integrated into the braided textile fabric during the manufacturing process and are prestressed and prestrained during inflation. Figure 2.8 shows a straight, inflatable, braided tube and a detail of one of the integral, axial reinforcing cords located on the member cross-section.

There can be any number of reinforcing cords located anywhere on the member cross-section in the model. An array α of length m (where m is the number of cords), is created for every section integration point. Each entry of α is the measure of the angle from the local positive z-axis counter-clockwise to the cord of interest. Figure 3.2 shows an arbitrary element cross-section at an integration point with the local element coordinate system (z and y are visible, x is into the page), along with the location of an arbitrary cord and the measure of the angle α. The number of section integration points (n), is specified for each element.
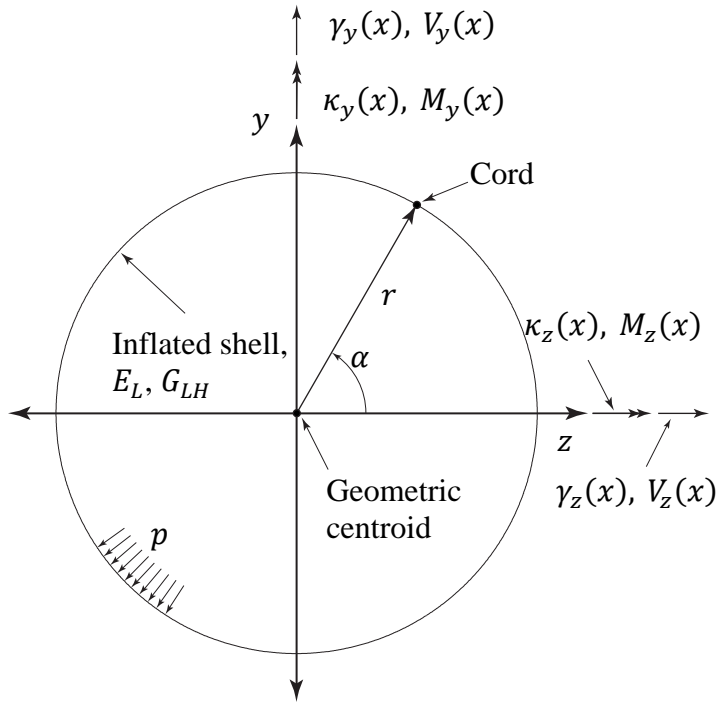
Figure 3.2. Illustration of shell cross-section with quantities of interest.

A cord configuration that is not evenly spaced around the cross-section will produce an internal, unbalanced moment. The internal moment must be brought into a state of equilibrium in an initial pressure equilibrium step, and an initial curvature will be present upon convergence. The cords are integrated into and bonded to the braided shell, as can be seen in Figure 2.8. During inflation and bend testing of the inflatable members no cord de-bonding or slip was observed. Strain compatibility is therefore assumed between the cords and braided shell.

Figure 3.2 contains additional information about the element cross-section that will be referred to throughout this paper. As in Figure 3.1, r is the radius of the inflated tube. Shown in Figure 3.2 are a number of section deformations and section forces. The

symbol d denotes the section deformation vector while the corresponding symbol D denotes the section force vector,

$$d(x) = \left[\varepsilon(x), \kappa_z(x), \kappa_y(x), \gamma_z(x), \gamma_y(x)\right]^T, \text{ and} \qquad \text{Equation 3.3}$$

$$D(x) = \left[N(x), M_z(x), M_y(x), V_z(x), V_y(x)\right]^T. \qquad \text{Equation 3.4}$$

The section curvatures and shear strains, $\kappa(x)$ and $\gamma(x)$, are illustrated in Figure 3.2 along with the section moments and shear forces, $M(x)$ and $V(x)$, about or on the z and y axes respectively. The section axial strain, $\varepsilon(x)$, and axial force, $N(x)$, are positive into the page (not shown).

The geometric centroid of the inflated shell is the origin of the local coordinate system and is shown for reference. Although the neutral axis (NA) can translate and rotate with the deformation of the element, all analyses are conducted from the geometric centroid of the integration point cross-sections and it is not necessary to track the movement of the NA or the elastic centroid. The inflated shell is assigned an extensional and in-plane shear modulus (E_L and G_{LH}), and each cord is assigned a one-dimensional, nonlinear force-strain relationship, as was discussed in Chapter 2. Also shown is the internal inflation pressure, p, that is defined for each element.

3.2.2   Flexibility-Based Element State Determination

A flexibility-based, fiber-beam element is used to handle the response of the inflatable member composed of materials with different, nonlinear constitutive relationships. The use of such elements for the analysis of inflatable members represents a departure from their traditional application to reinforced concrete members. Prior to the onset of material nonlinearities in a frame analysis the displaced shape of a member can be

described exactly using displacement interpolation functions. After the onset of material nonlinearities or plasticity a displacement based interpolation function can no longer exactly describe the member's shape; however, the force and moment distribution through the member can be described exactly. For example, in the case of nodal loading, the axial force is constant through the member while the moment varies linearly. An iterative (Spacone et al. 1996a and 1996b; Taucer et al. 1991) or non-iterative (Neuenhofer and Filippou 1997; de Souza 2000) procedure is used to ensure that the distributions of section forces at element integration points are compatible with the force interpolation functions upon convergence of the load increment. Force-based beam elements are computationally more demanding than displacement based beam elements; however, these elements are able to effectively and stably handle material nonlinearities and generally require fewer degrees of freedom to achieve a desired level of accuracy (Neuenhofer and Filippou 1997). For the current study geometric nonlinearities are handled at the element level using the corotational formulation, a geometrically linear flexibility-based beam element at the section level and sufficient mesh refinement. The element formulation could be further extended in the future to include geometric nonlinearities at the section level for the materially nonlinear, shear deformable inflatable members, as was done by Neuenhofer and Filippou (1998) for materially linear, Euler-Bernoulli beams, or by de Souza (2000) for Euler-Bernoulli beams including material nonlinearities. However, such a refinement is not required.

The non-iterative form of the state determination process was employed following Neuenhofer and Filippou (1997). From a previously converged state, the element displacements (q) are obtained from the corotational formulation (Equation 3.1). The

element resisting force increments ($d\boldsymbol{Q}$) are calculated using the current element

displacements and the element displacements from the previous iteration ($\boldsymbol{q_0}$), along with

the previous element stiffness matrix ($\boldsymbol{K_0^{el}}$),

$$d\boldsymbol{Q} = \boldsymbol{K_0^{el}}(\boldsymbol{q} - \boldsymbol{q_0}).$$ Equation 3.5

Because the torsional portion of the element response is decoupled from the axial, shear

and flexural response, the torsional component of all calculations at the element and

section level is excluded until the end of the analysis, when it is added back into the

element resisting force vector and element stiffness matrix.

The element quantities must next be related to quantities at section integration points.

Quantities are calculated at each section integration point from one ($x = 0$) to n ($x = L$).

Force interpolation functions ($\boldsymbol{b}$) relate the resisting forces at the nodes ($\boldsymbol{Q}$), to the section

forces ($\boldsymbol{D}$, Equation 3.4), without element loading,

$$\boldsymbol{b}(x) = \begin{bmatrix} 1 & 0 & 0 & 0 & 0 \\ 0 & x/L - 1 & x/L & 0 & 0 \\ 0 & 0 & 0 & x/L - 1 & x/L \\ 0 & -1/L & -1/L & 0 & 0 \\ 0 & 0 & 0 & 1/L & 1/L \end{bmatrix}.$$ Equation 3.6

The shear forces are included in the section quantities whereas the current analysis

includes shear deformation. Shear deformations are incorporated into the force-based

element following Marini and Spacone (2006), generalized to three dimensions. The

shear response of the element is modeled using Timoshenko beam theory. The shear

response at the section level is modeled as linear and decoupled from the axial and

bending response. Assuming that a shear strain does not induce an axial strain in the

cords is consistent with a small strain analysis. The shear stiffness of pressurized braided tubes has been shown experimentally to be pressure dependent, but essentially constant at a given pressure (Clapp et al. 2016a). The component of shear deformation is a small percentage of the total deformation for braided inflatable members where off-axis fibers provide some shear resistance. Shear deformation was found to vary from 2.5 to 11% of the total elastic portion of the deformation for the current study, highest for beams with a low inflation pressure and a high braid angle. Shear deformation can be significant (over 30%), for other types of inflatable beams, such as woven members (Kabche et al. 2011), due to the high shear compliance of woven fabrics.

The section force increments are determined by interpolating from the nodal resisting force increment using the force interpolation functions and including the residual, or unbalanced, section forces from the previous iteration, D_0^u, discussed later,

$$dD(x) = b(x)dQ + D_0^u, \qquad \text{Equation 3.7}$$

The section deformation increments can then be calculated using the section force increments and the flexibility matrix (f_0), saved from the previous iteration,

$$dd(x) = f_0(x)dD. \qquad \text{Equation 3.8}$$

The section deformation increments are added into the section deformations from the previous iteration,

$$d(x) = dd(x) + d_0(x). \qquad \text{Equation 3.9}$$

Next, the section constitutive relationship must be used to calculate the section resisting forces. The location of each axial reinforcing cord is stored at each section using an m by five geometric array, l,

$$l(x) = [1, -\sin\alpha, \cos\alpha, 0, 0].$$ Equation 3.10

The last two entries in each row of l are zero because the shear deformations of the

section are assumed to not contribute to the cord deformation. The cord deformation

increments, or cord strain increments, are calculated as,

$$de(x) = l(x)dd(x),$$ Equation 3.11

and are used to update the previously saved total cord deformation array,

$$e(x) = de(x) + e_0(x).$$ Equation 3.12

The initial strain in each cord at each section point is interpolated from the cord force-

strain relationship,

$$e_0(x) = e_0(x, T_0).$$ Equation 3.13

The initial force in the cord at inflation pressure (T_0) is obtained from netting theory

(Equation 2.17). Using the axial force-strain lookup table that has been defined for each

cord at each section point, the tensile force in the cords at each section, $T(x)$, can be

interpolated using the updated cord deformation array, $e(x)$,

$$T(x) = T(x, e(x)),$$ Equation 3.14

along with the tangent stiffness of each axial reinforcing cord,

$$EA_{tan}(x) = EA_{tan}(x, e(x)).$$ Equation 3.15

The geometric array, l, is then used to calculate the cord component of the section

stiffness matrix including all axial-bending and z-y bending coupling terms,

$$k_{cord}(x) = l^T(x)[EA_{tan}(x)]_{diag}l(x).$$ Equation 3.16

The component $[EA_{tan}(x)]_{diag}$ is the cord stiffness arranged as an m by m diagonal

matrix, rather than a vector of length m. The shell portion of the section stiffness matrix

is taken as,

$$k_{shell}(x) =$$

$$\begin{bmatrix} E_{gross}2\pi r & 0 & 0 & 0 & 0 \\ 0 & E_{gross}\pi r^3 & 0 & 0 & 0 \\ 0 & 0 & E_{gross}\pi r^3 & 0 & 0 \\ 0 & 0 & 0 & G_{LH}\pi r + p\pi r^2 & 0 \\ 0 & 0 & 0 & 0 & G_{LH}\pi r + p\pi r^2 \end{bmatrix}.$$

The usual shear correction factor of two for a thin walled circular section is used in the calculation of the section shear stiffness. Including the pressure resultant in the shear stiffness terms accounts for the work done by the internal inflation pressure undergoing a volume change due to shear deformation (Fichter 1966, Davids and Zhang 2008). Although the contribution of this stiffness term is minimal for braided, inflatable members, especially when compared to a woven inflatable member, it is included here for completeness. The five by five section stiffness matrix, $k(x)$, is the sum of $k_{cord}(x)$ and $k_{shell}(x)$. The current section flexibility matrix, $f(x)$, is found by inversion of the section stiffness matrix.

The section resisting forces are calculated as the sum of cord and shell forces. The initial force in the cords due to inflation pressure be accounted for when calculating the axial resisting force,

$$D^r(x) = \left\{ \begin{array}{c} \sum_{i=1}^{m} T_i(x) - p\pi r^2(1 - 2cot^2\beta) \\ -\sum_{i=1}^{m} T_i(x)r\sin\alpha_i \\ \sum_{i=1}^{m} T_i(x)r\cos\alpha_i \\ 0 \\ 0 \end{array} \right\} + k_{shell}(x)d(x).$$

The section resisting forces interpolated from the element resisting forces will not generally be equal to the section resisting forces calculated using the section constitutive relationship. The residual section deformation can be calculated as,

$$\boldsymbol{\rho}(x) = \boldsymbol{f}(x)[\boldsymbol{D}_0^r(x) + d\boldsymbol{D}(x) - \boldsymbol{D}^r(x)].$$

<div align="right">Equation 3.19</div>

Once all section quantities have been calculated the current element flexibility matrix and the element residual displacements can be determined by integrating over the element length,

$$\boldsymbol{F} = \int_0^L \boldsymbol{b}^T(x)\boldsymbol{f}(x)\boldsymbol{b}(x)dx,$$

<div align="right">Equation 3.20</div>

and

$$\boldsymbol{r} = \int_0^L \boldsymbol{b}^T(x)\boldsymbol{\rho}(x)dx.$$

<div align="right">Equation 3.21</div>

A Gauss-Lobatto numerical integration scheme is employed following Spacone et al. (1996). Although the Gauss-Lobatto integration scheme is less accurate than typical Gauss integration, the sections always include the element end points. In a frame analysis with loading concentrated at the member ends, the maximum moment and therefore point of greatest material nonlinearity will be at an element end. Including the ends of elements in the analysis as an integration point therefore improves the accuracy of the solution.

The current element stiffness matrix ($\boldsymbol{K}^{el}$) in the local element coordinate system is found by inverting the element flexibility matrix ($\boldsymbol{F}$). The total element resisting forces can then be updated using the previous element forces, $\boldsymbol{Q}_0$,

$$Q = Q_0 + dQ - K^{el}r.$$ Equation 3.22

The element residual forces ($K^{el}r$) are included in Equation 3.22 so that they can be

assembled into the global internal force vector and accounted for during global

equilibrium iterations. The unbalanced section resisting forces can be calculated for the

next iteration by comparing the interpolation of element forces to the section equilibrium

summations,

$$D^u(x) = b(x)Q - D^r(x).$$ Equation 3.23

The unbalanced section forces are passed to the next global FE iteration where they are

again applied to Equation 3.7 at the element level. Upon global convergence of the

loading increment the residual section deformations will be sufficiently minimized and

the element will be brought into a state of compatibility.

After application of the state determination process the component of torsional stiffness

can be included in the element stiffness matrix, turning the five by five axial and flexural

stiffness matrix into a six by six matrix including all of the local element degrees of

freedom,

$$K_{torsion} = G_{LH}\frac{2\pi r^3}{L}.$$ Equation 3.24

The torsional behavior of the element is uncoupled from the axial, flexural and shear

response. Modeling the torsional response of the shell as uncoupled from the shear

response and the axial response of the fibers is consistent with a small strain analysis for

a straight member. In the case of large torsional deformations or in the case of a curved

beam, decoupling the torsional response from the basic system may not be justified

whereas an axial strain may be caused by warping effects or from torsion-bending

54

coupling respectively. The torsional restraining force is added to the end of the element resisting force vector,

$$M_x = K_{torsion}\theta_x.$$

Equation 3.25

The current element tangent stiffness matrix ($\boldsymbol{K^{el}}$) and element resisting forces ($\boldsymbol{Q}$) can then be sent back to the corotational formulation (Crisfield 1990) for incorporation into the global stiffness matrix along with the geometric stiffness matrix, and the creation of the internal force vector, respectively. Global Newton iterations continue until the externally applied forces are in equilibrium with the internal element forces, within a specified tolerance.

3.2.3   Convergence of Element

In order to check convergence of the element the critical buckling capacity (F_{cr}), of a linearly elastic, shear deformable member with both ends pinned was compared to an analytical solution from Fichter (1966) with no internal inflation pressure,

$$F_{cr} = \frac{EI\frac{\pi^2}{L^2}GA_v}{EI\frac{\pi^2}{L^2} + GA_v}$$

Equation 3.26

The length of the column (L) was taken as unity and the stiffness product, EI, was taken as π^{-2}. As can be seen from Equation 3.26, as the shear stiffness of the section (GA_v) goes to infinity, F_{cr} converges to the critical buckling factor for an Euler-Bernoulli column, which is unity for the parameters used here. The two-dimensional finite element model, shown in Figure 3.3, consists of a member with one end restrained from translating and the other end restrained from translating perpendicular to the axis of the member. An axial compression load was applied to the roller end of the member. A half

55

sine wave perturbation was included in the initial geometry of the member such that the

mid-span eccentricity was equal to 0.1% of the element length. Figure 3.3 shows the

convergence of the model for a varying number of nodes compared to the analytical

solution, represented by the dashed lines (Equation 3.26).
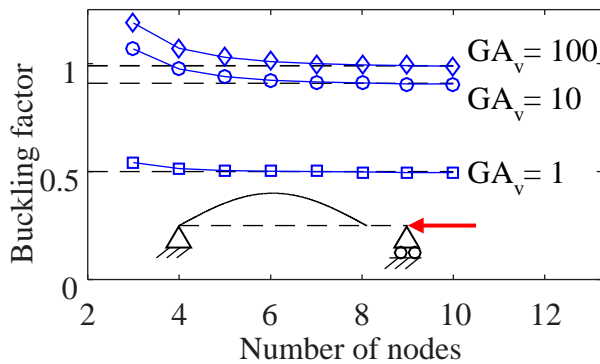
Figure 3.3. Convergence of model to critical buckling load for a shear deformable

member

As can be seen from Figure 3.3, the model converges to the analytical solution. Although

a faster rate of convergence could be obtained by incorporating geometric nonlinearities

into the flexibility formulation at the section level, a satisfactory solution can be obtained

by simply refining the mesh.

3.2.4 Application

With the development of the beam-based FE modeling methodology complete it was implemented in a general-purpose FE modeling code developed in the MATLAB environment and applied to the analysis of inflatable members and structures. Chapter 4 documents the validation studies performed on component level tests of straight tubes and individual torus structures while Chapter 5 presents validation studies performed on the full HIAD structure. The tools are then further extended to the analysis of full-scale HIAD structures in Chapter 6.

Chapter 4

FINITE ELEMENT MODEL VALIDATION: COMPONENT LEVEL

This chapter presents the results of studies conducted in order to validate the beam-based FE modeling methodology that was developed in the previous chapter. The straight tube tests conducted by Clapp et al. (2016b) are modeled using both the beam-based FE modeling methodology, and a high-fidelity shell-based FE modeling methodology. The beam-based modeling tools are then extended to model the torus load tests that were detailed in Whitney (2016). Chapter 5 contains additional validation studies in which the beam-based modeling tools are applied to the analysis of full HIAD pressure tub tests conducted by NASA (Swanson et al. 2015).

4.1 Analysis of Straight Tube Testing

An important step in the development of the beam-based FE modeling methodology for inflatable, braided, slender members with discrete axial reinforcing cords is to compare modeling results to component level tests and shell-based FE modeling techniques. In the following section the beam-based FE modeling techniques are applied to the analysis of straight tube four-point bending tests performed on specimens with varying braid angles, inflation pressures and in multiple orientations.

4.1.1 Description of Tests

An extensive experimental campaign to acquire the four-point bend load deformation behavior of straight, inflatable, braided tubes with discrete axial reinforcing cords was conducted along with the development of shell-based FE models, details of which can be found in Clapp et al. (2016b).

All of the test specimens had three axial reinforcing cords that were evenly spaced around the shell cross-section. The angle of the braid, the internal inflation pressure and the orientation of the specimens were varied. Figure 4.1 presents the straight tube four-point bend test configuration. The ends of the beams were supported by rollers with a center of rotation located 350 mm down from the center of the inflated tube. The distance between roller centers was 3,280 mm. Two loading straps were centered in the clear span and located 1,040 mm apart (center to center). A spreader beam was used to transfer the load from the actuator to the two strap sets. The displacement of the member at the mid-span was recorded using string potentiometers and a photogrammetry system.

Figure 4.1. Straight tube four-point bend test configuration.

4.1.2   Shell-Based Finite Element Model

A three-dimensional shell finite-element model was developed using the commercial FE software package ABAQUS (2014) to predict the response of the four-point bend test specimens. The inflatable tube was modeled with element type S8R, an 8 node reduced integration quadratic shell element. The shell section was defined as a laminate

consisting of three lamina. The shell material was defined as a linearly elastic, orthotropic material, as was previously described in Chapter 2. The Technora cords, which are integral to the inflated tube, were modeled with element type B32, a 3 node quadratic beam element. The cord nodes were superimposed onto the shell nodes. The cord beam section was defined generally by specifying the area, bending moments of inertia and torsional rigidity of the section. The axial behavior of the beam elements were defined as a tension only material by means of a direct force-strain input table from material testing, also described in Chapter 2. All geometric parameters were based on as-built conditions and all properties input to the model were from independent component-level testing (see Table 2.2).

In four-point bend testing of the inflatable tube and in tension testing of the cord material (Figure 2.11), it was observed that the first application of loads produces results that are significantly less stiff than subsequent loading cycles. Results were repeatable after the second load application. Because each inflated test specimen was subjected to multiple loading cycles at different inflation pressures and orientations, the third load cycle is reported here for consistency across all specimens and orientations. The third cord tension loading cycle was also used in developing the cord force-strain relationships used in the FE models. Contact pairs were defined between the loading strap and the inflatable tube, and also between the rigid support cradle and the inflatable tube. Contact conditions between the beam and loading strap and the beam and support cradle were modeled in order to accurately capture actual test boundary conditions.

In order to reduce the computational expense of the model, half symmetry was employed. The nodes in the center of the beam are constrained from moving in the global Z

direction, as defined by the triad in Figure 4.2. The nodes are further constrained from

rotating about the X or Y axes. The end of the beam was supported by a rigid cradle on a

roller. The motion of the cradle was tied to a point located below the cradle that was

coincident with the actual center of rotation of the support wheel in the test assembly.

The roller was constrained from translating in the X or Y direction, and rotating about the

Z axis. The free end of the inflatable tube was modeled as rigid, the behavior of the tube

at the free end was not of interest. There was over one tube diameter between the rigid

support and the rigid free end of the beam to eliminate the influence of any unwanted

edge effects.
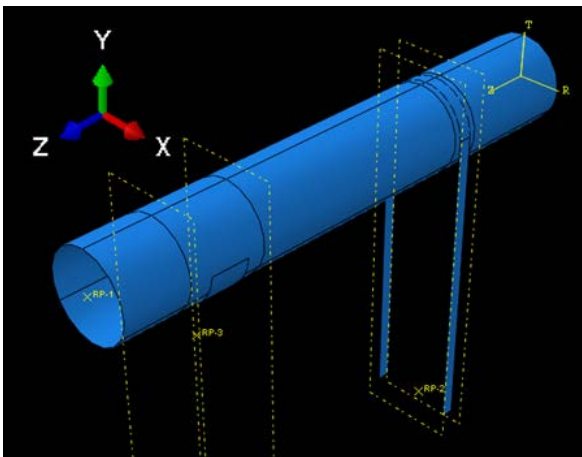
Figure 4.2. Half-symmetric 3D finite-element model of straight tube bending test (saddle

support on left and applied loading through straps on right).

The model utilizes three loading steps in the analysis process: an inflation step, a gravity

step and finally a loading step. In the inflation analysis step loads are applied to the tube

to simulate the inflation process. The internal pressure was modeled as a distributed

follower force. The end resultant was applied to the rigid tube end as a shell edge load

with a total magnitude equaling the pressure end resultant. Modeling the internal

pressure as distributed follower forces, as opposed to an encapsulated ideal gas, was reasonable in this case whereas the pressure was constant over the entire quasi-static test. A large displacement analysis was employed.

The second analysis step simply applies an acceleration to the model equal to the acceleration due to gravity. Although the effect of self-weight was minimal in this test configuration (the inflatable tubes have a mass of about 4.5 kg), it was included to increase the realism of the model. As in the case of the inflation step, a large displacement analysis was employed.

In the final analysis step, force was applied to the strap ends to simulate the loading of the inflated tubes. The strap ends are constrained to only allow translation in the global Y direction, the direction of the applied force. The loading was transferred to the inflatable tube through contact, as in the real structure. A large displacement analysis in conjunction with an arc-length or Riks solver was employed. The arc-length solver allows the analysis to overcome any instability caused by wrinkling of material above the neutral axis of the beam and to obtain the post-wrinkling behavior of the specimen.

The displacement solution was generally the solution of interest. Converged solutions were obtained with relatively large elements having approximately 75 mm sides. A typical model of an inflatable tube consisted of approximately 1,350 nodes and 450 elements. A screenshot of the finite-element model at peak displacement is shown in Figure 4.3. The yellow arrows indicate the magnitude of tensile forces in the cords. Note that the top cord forces are less than the bottom cord forces due to the reduction from applied bending loads, but are still in tension since load loss due to the applied bending

moment was less than the load due to initial inflation. Comparisons with experimental

results, and with the beam-based FE modeling approach are presented in Figure 4.5 and

Figure 4.6, along with the predictions from the beam-based model described next.
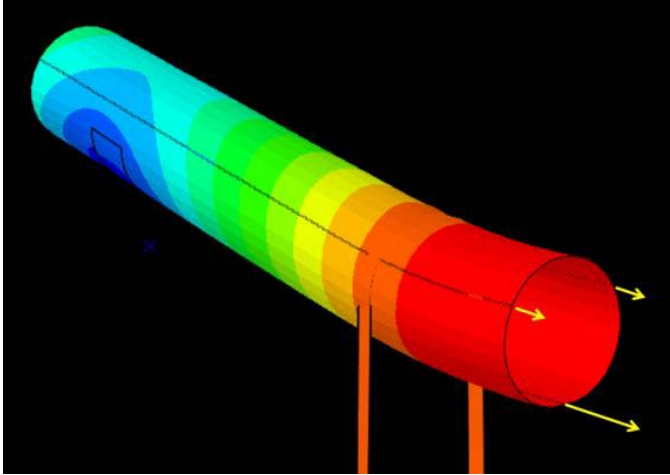
Figure 4.3. Deformation of shell-based finite element model (red to blue colors indicate

high to low deflections, respectively; yellow arrows represent the magnitude of tensile

cord load).

4.1.3   Beam-Based Finite Element Model

The beam-based FE modeling tools that were developed in Chapter 3 were applied to the

analysis of the straight-tube four-point bend test. FE model inputs were measured

directly from test specimens, rather than utilizing nominal values and the third load cycle

was utilized for the development of all material models, as was the case for the

development of shell-based FE models. The measured geometric and material inputs that

were used in the analyses are presented in Table 2.2.

Global load controlled Newton iterations were utilized and adaptive load stepping was

implemented in all analyses (Clarke and Hancock 1990). To further reduce computation

time, half symmetry of the four-point bend test was employed. A rigid vertical link was

used to model the effect of the roller offset from the tube centerline. The bottom of the link, or roller, was constrained from translating vertically or out-of-plane, and from rotating about an axis parallel with the beam (Figure 4.4). The components of rotation perpendicular to the axis of the beam were constrained at the plane of symmetry, along with displacement parallel to the longitudinal axis of the beam. Ten elements utilizing three integration points were utilized in all analyses. The mesh was found to be acceptably refined and a converged load-displacement curve could be obtained with a coarser mesh.
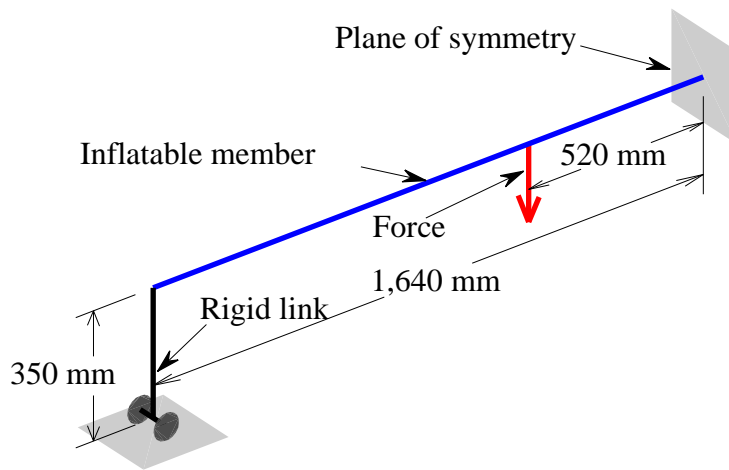
Figure 4.4. Beam model of straight tube test.

4.1.4 Comparison of Experimental, Shell and Beam-Based Finite Element Results

For the current study two inflatable tube test specimens were analyzed, one with a nominal 60° braid angle and one with a nominal 71° braid angle. Both specimens were analyzed in two configurations at four inflation pressures (34, 69, 103 and 138 kPa), for a total of 16 analyses. In the one-cord-up configuration α, the location of the cords measured counter-clockwise from the horizontal axis, was taken as $[90°, 210°, 330°]$. In the two-cords-up configuration α was taken as $[30°, 150°, 270°]$.

Figure 4.5 and Figure 4.6 present the load versus mid-span displacement test results and analyses of the nominal 60° and 71° specimens respectively. Beam FE modeling results were compared with experimental and shell-based FE results. As can be seen from the modeling results, the beam FE modeling methodology captures the initial stiffness of the experimental results, the wrinkling load, the soft transition to the wrinkled state and the post-wrinkling stiffness with reasonable accuracy. The wrinkling load, which corresponds with a dramatic reduction in beam stiffness that occurs when the top-most cord(s) lose pretension due to inflation, is accurately captured by the model and the response is tracked well beyond the point of initial wrinkling. It is especially important to note the significant drop in wrinkling load with braid bias angle and inflation pressure which is correctly predicted by the model.
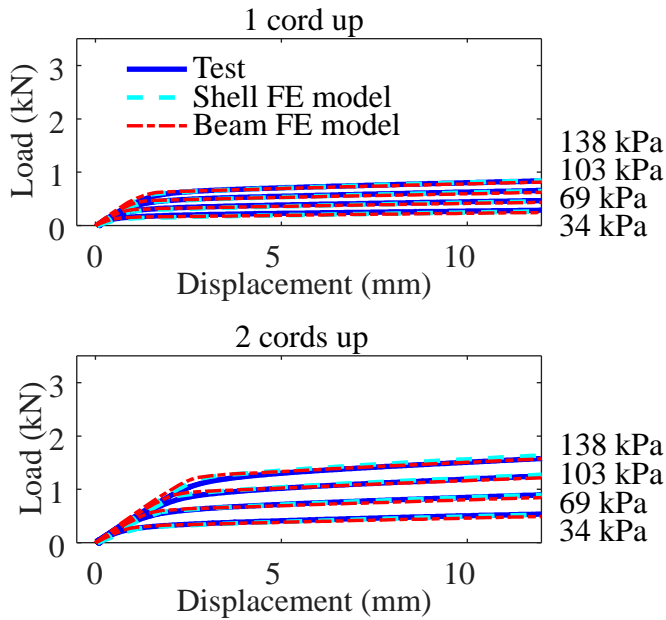
Figure 4.5. Comparison of experimental results with shell and beam FE modeling for nominal 60° straight tube four-point bend tests.
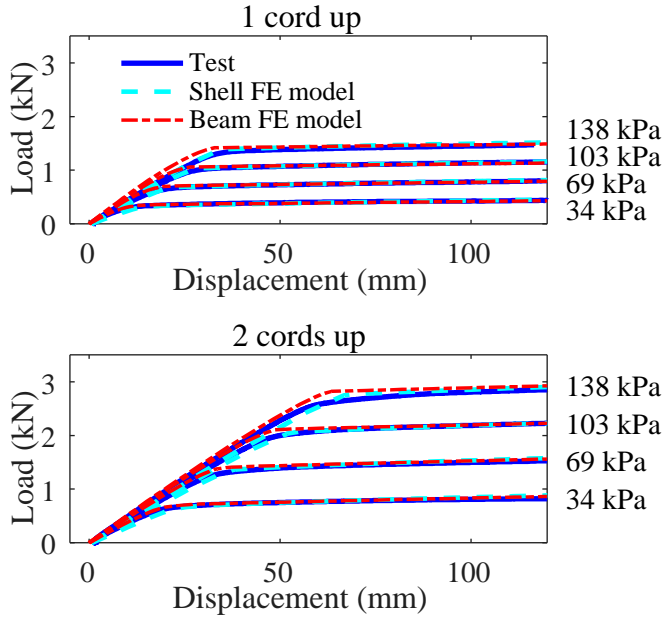
Figure 4.6. Comparison of experimental results with shell and beam FE modeling for nominal 71° straight tube four-point bend tests.

Figure 4.7 illustrates the load deformation response of a representative analysis (60° braid angle, two cords up at 138 kPa of inflation pressure). The deformed configuration is shown for every 0.2 kN of applied load. As can be seen from the plot, most of the deformation occurs at the end of load application process.
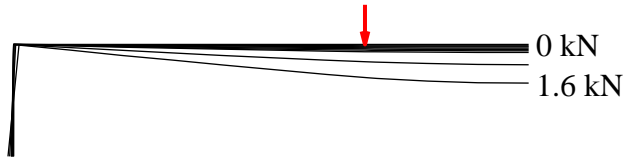
Figure 4.7. Trace of deformed member for every 0.2 kN of applied load, 60° braid angle, 138 kPa inflation pressure, 2 cords up.

Figure 4.8 presents comparisons of initial stiffness of the four-point bend test with shell and beam FE models. The initial stiffness was calculated as a least squares fit to the initially linear portion of load displacement curves (Figure 4.5 and Figure 4.6), taken at

66

load levels below 50% of the load corresponding to the knee in the load-displacement response. As can be seen from Figure 4.8, both the shell and beam FE models reasonably track the increase in initial stiffness with an increase in pressure. The beam FE modeling results tend to predict a somewhat stiffer response than is observed with testing or predicted by the shell FE model. However, the beam FE model would be expected to predict a stiffer load displacement response due to its inherent kinematic assumptions of plane sections and first-order shear deformation theory, and since it cannot capture three-dimensional deformations of the shell.
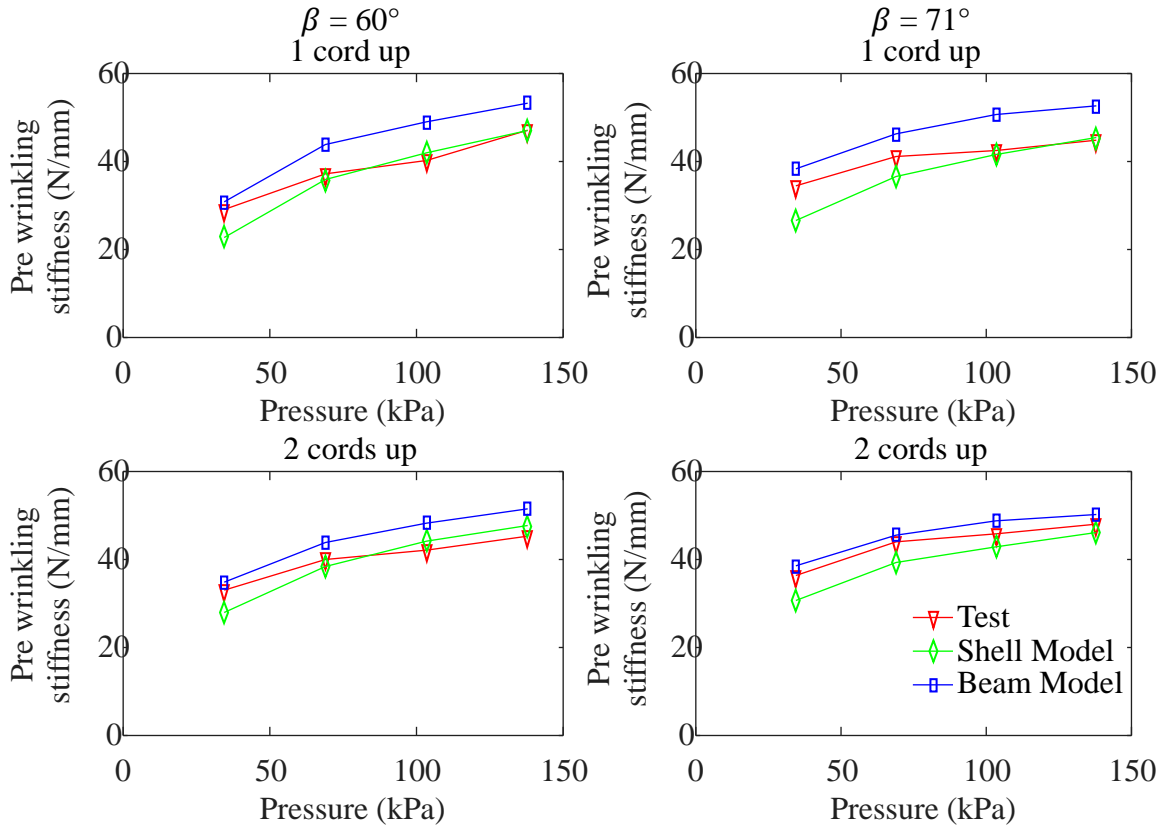
Figure 4.8. Comparison of initial stiffness.

Figure 4.9 presents the change in the post wrinkling stiffness with pressure of the four-point bending test, shell FE model and beam FE model. The post wrinkling stiffness was

calculated as a linear fit to the four-point bend load displacement curve after the onset of wrinkling to 120 mm of displacement. As with the initial stiffness, the change in post wrinkling stiffness is generally tracked by both the shell and beam FE models. In this case the shell FE model predicts a slightly stiffer response than the beam FE model. This may be due to the shell model accounting for the small change in radius that occurs post wrinkling. When the member wrinkles the NA drops from the initial, geometric centroid of the shell, putting more of the cross sectional area into compression. The average radius of the cross section will then increase slightly due to the Poisson effect. Although the pressure-volume change work that occurs as a result of this change in radius is accounted for in the beam-based FE model, the slight increase in section modulus is not.

In the case of the 71° beam the post wrinkling stiffness of the tests seems to be approximated by the both the shell and beam FE models, but not tracked with change in pressure, as is the case for the 60° specimen. The discrepancy between measured and predicted post wrinkling stiffness is due to the measurement of the shell extensional stiffness. The post wrinkling stiffness is dominated by the extensional stiffness of the shell. As can be seen from Table 2.2, the measured value for E_L for the 71° beam does not increase with pressure. Further, the magnitude of the change in longitudinal stiffness that results from a change in braid angle as the shell undergoes an extension decreases as the braid angle increases (Equation 2.30). The post wrinkling stiffness of the 71° beam may improve with the pressurized tension testing of a more representative specimen or by utilizing mean values from a larger tension testing data set.
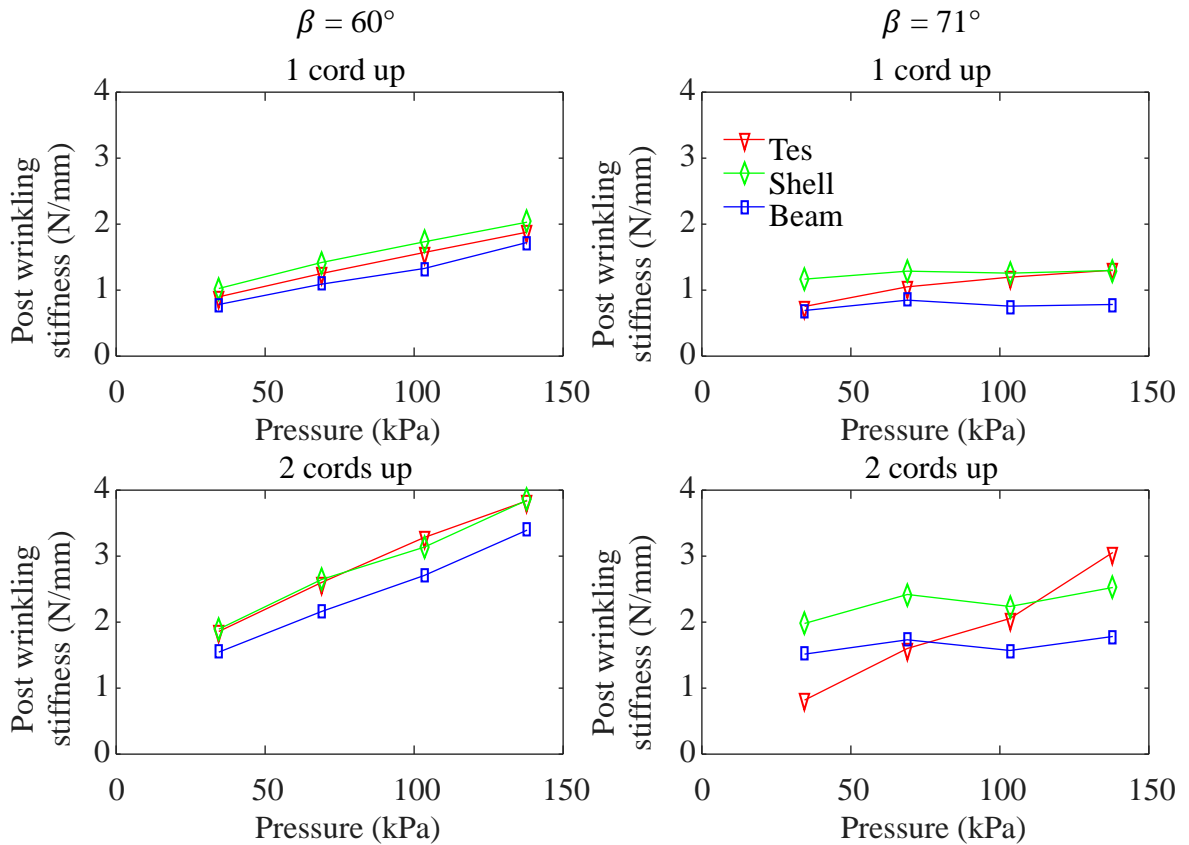
Figure 4.9. Comparison of post wrinkling stiffness.

Although both the shell and beam-based FE models closely follow the experimental results, the shell FE models do so with a significant increase in the number of degrees of freedom. The beam model has approximately 150 degrees of freedom versus 8,000 degrees of freedom for the shell-based FE model. Further, the shell-based model incorporates a number of multiple degree of freedom constraints and contact interactions. The beam FE models are able to accurately capture the response of the inflatable members across internal inflation pressures, braid angles and member orientations with a significant decrease in the number of degrees of freedom and model complexity.

4.1.5 Out-of-Plane Deformations

Although the response of the members was primarily in-plane, out-of-plane deformations were also of interest and could be induced with some member configurations. Significant out-of-plane deformations were observed in some cases during testing. The out-of-plane deformation was driven by small manufacturing imperfections in the members, as is discussed below. Including initial imperfections in the model allows the analysis to capture the full three-dimensional response of the specimens and illustrates the sensitivity of these structures to the presence of imperfections, and the importance of capturing the full three-dimensional response. Also of interest was the response of the member with the symmetric axis of the cross-section oriented horizontally, rather than vertically as was the case for previous straight tube analyses. Orienting the cross-section of the member in this manner could allow for comparisons to future torus configurations, where the symmetric axis of the member cross-section is also oriented horizontally.

During four-point bend testing of the straight, inflatable tubes out-of-plane deflections of approximately 40 mm occurred, although all loading remained in-plane. These out-of-plane deflections were not initially noticed visually during the test, but were captured by digital image correlation data gathered during testing. Out-of-plane deflections were particularly pronounced in the two cords up configuration after the wrinkling load had been reached. As the inflatable tube was loaded the top cords began to lose their pretension while the tensile force in the bottom cord increased. Once the strain in the top cords became negative the member had lost almost all lateral stiffness and small imperfections or a misalignment of the bottom cord axis with the longitudinal axis of the beam caused by a slight twisting of the member could cause relatively large out-of-plane

deflections; this phenomenon is essentially a lateral buckling instability. Figure 4.10

illustrates the cord misalignment that occurred during testing of the straight tube

specimens on one of the support saddles. Shown is the bottom cord offset from the white

tic mark indicating dead center of the support. When a twist was observed down the

length of a beam, efforts were made to ensure that the bottom cord straddled opposite

sides of the dead center mark on opposite sides of the beam with the goal of positioning

the cord as close as possible to the bottom of the cross-section at mid-span.

Figure 4.10. Cord misalignment during straight tube four-point bending test.

In the case of the tube-twist analysis the entire beam was modeled. In the shell model an

additional step was incorporated that enforced a rotation at one end of the beam equal to

1°. All other boundary and loading conditions were the same as in previous analysis,

except that symmetry was not employed. In the beam model a total of 20 elements were

used, each with three integration points, since symmetry boundary conditions would

unrealistically restrain the beam. The boundary conditions of the roller end of the beam

(Figure 4.4) were applied to both ends of the beam. An additional translational constraint

parallel with the longitudinal axis of the beam was added at one end of the member to

fully constrain the model. Figure 4.11 shows both the experimental, and shell and beam based FE modeling results of the analysis.
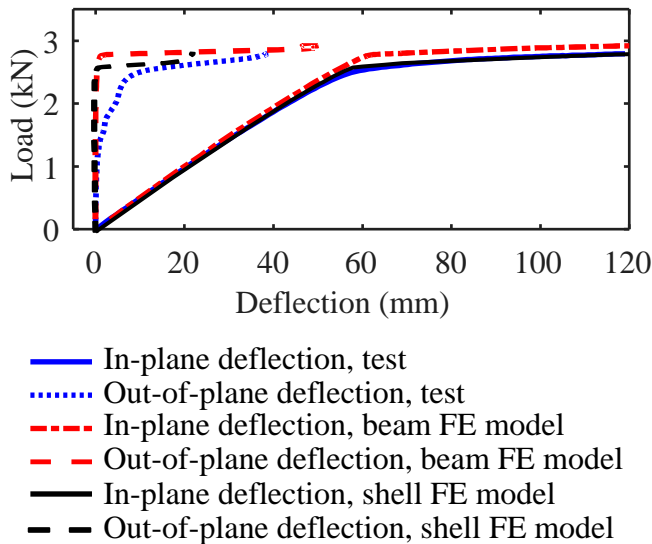
Figure 4.11. In-plane and out-of-plane load deformation behavior for a 71° beam at 138 kPa of inflation pressure with two cords up and a 1° twist.

As can be seen from Figure 4.11, the beam FE model response follows the three-dimensional response of the straight tube experimental results closely. There is minimal out-of-plane deflection until the onset of wrinkling, when the top cords lose stiffness. Following the wrinkling of the beam, the off-axis bottom cord drives out of plane deflection to magnitudes similar to those observed in testing. In the beam FE model and the experimental setup, the torsional stiffness of the tube restrains the out-of-plane deflection. In the experimental setup and shell-based FE model the tube is further restrained to some extent by the loading strap that was used to apply the vertical load.

Also analyzed was the inflatable member in a third orientation, with the three cords located at $\alpha = [60°, 180°, 300°]$. The symmetric axis of the cross-section was oriented vertically, rather than horizontally, as was the case for the previous analyses. The

horizontal orientation of the member is of interest because two of the three cords will be aligned vertically, as in the case of a torus member. With the exception of the orientation of the member, the beam-based FE model that was developed was identical to the twisted member analysis. The braid angle of the member was maintained at 71° and the internal inflation pressure was 138 kPa. A load test of the member in the horizontal orientation was not conducted. The predicted response of the member is shown in Figure 4.12.
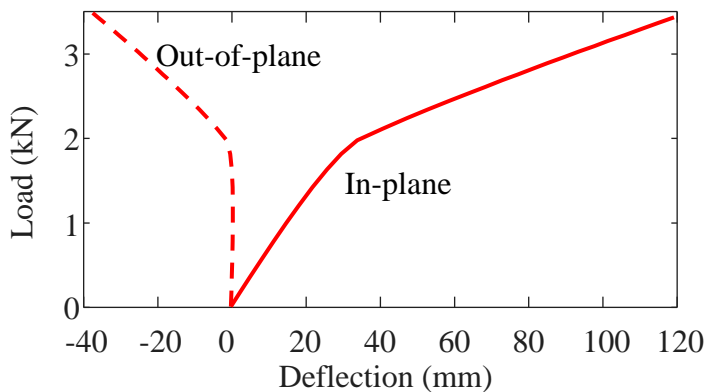
Figure 4.12. In-plane and out-of-plane load deformation behavior for a 71° beam at 138 kPa of inflation pressure with the symmetric axis of the member oriented horizontally.

The out-of-plane displacement of the member is again essentially zero pre-wrinkling; with the symmetric axis of the three cords oriented horizontally the centroid of member is still located at the geometric center. The wrinkling load was lower than the wrinkling load of the member in the two-cord-up configuration, but was higher than the one cord up configuration. The post wrinkling stiffness both in and out-of-plane was higher than the post wrinkling stiffness for both the one and two cords up configurations. As the top cord lost stiffness the two remaining cords were offset both horizontally and vertically and provided additional geometric stiffness when compared to the one and two cords up configurations.

4.2   Analysis of Torus Testing

In order to understand and to be able to predict the structural response of the HIAD system, the behavior of individual tori must be understood. The beam-based FE modeling methodology that was developed in Chapter 3 for slender, inflatable, braided members with axial reinforcing cords is applied to the analysis of toroidal components. The torus load testing and experimentation are fully described in Whitney (2016) and additional comparisons are made in Young et al. (2017b).

4.2.1   Background

Previous research on the structural response of inflatable tori is generally limited to analytical studies. Weeks (1967) performed an analytical investigation on the buckling of inflatable, shear deformable tori subject to both conservative and non-conservative uniform external loading. Le van and Wielgosz (2007) used the numerical test cases of a pinched toroidal beam and a toroidal beam subject to a radial compressive force to partially validate the development of a beam-based finite element (FE) modeling approach for isotropic inflatable members. Wang et al. (2009) applied the method for analyzing slender, inflatable members developed by Le van and Wielgosz (2005) to the load deformation analysis of an inflatable frame that included toroidal members. Roychowdhury and DasGupta (2015a) investigated the response of hyperelastic toroidal membranes subject to a radial line load applied to the inner equator of the torus. Various hyperelastic material models, deflated inner and outer radius ratios, and internal inflation pressures or constant amounts of gas were analyzed. Berger et al. (2004) performed a limited experimental investigation into the out-of-plane static response of an inflatable torus composed of twelve straight segments.

74

Others have also studied the dynamic response of inflatable tori analytically and computationally. Investigations include those performed by Smalley et al. (2001), Raouf and Palazotto (1996), Jha (2002) and Pazhooh et al (2011a and 2011b), all using a variety of modeling methodologies and material models. The inflation process of toroidal members has been investigated by Tamadapu and DasGupta (2013 and 2014) and by Roychowdhury and DasGupta (2015a and 2015b).

Like tori, inflatable arch systems are subjected to combined bending, axial compression and potentially torsion under simple loading regimes. The study of inflatable arches tends to be more grounded in experimental methods than tori, likely due to the simpler fixed or pinned boundary conditions at both ends. Guo et al. (2015) experimentally and numerically investigated the response of a full-scale inflatable terrestrial structure composed of inflatable arches and beams. The inflation of individual arches was also investigated experimentally and numerically by Li et al. (2016). The inflatable members were modeled using membrane elements and pressure follower forces to simulate inflation pressure in both cases. Molloy et al. (1999) numerically investigated various loading regimes on a pair of leaning arches that were in contact at their apex. Likewise, Plaut et al. (2000) derived the equations for a pressurized membrane arch and applied various loading regimes to investigate the in-plane response. Roekens et al. (2016) experimentally and numerically investigated the response of the 'tensairity' arch that combines both rigid and inflatable components by attaching aluminum flanges to the top and bottom outer sections of the inflatable member with a circular cross section.

Davids (2009) investigated the response of woven fabric pressurized arches experimentally and numerically. A two-dimensional beam element was used to model

the response of the inflatable members, work due to inflation pressure was incorporated, and nonlinear moment-curvature relationships for varying levels of axial load were used to treat the tension only nature of the pressurized fabric. Brayley et al. (2012) investigated the response of braided fabric arches with externally bonded reinforcing straps. Moment-curvature relationships were again used to model the response of the members, an approach that does not capture biaxial bending coupling and axial-bending coupling that can occur. In all cases only the in-plane response of the arches was analyzed, although out-of-plane deformations were either observed or prevented from occurring with bracing.

Obtaining the structural response of real, inflatable, braided torus structures with axial reinforcing presents a significant increase in experimental and analysis complexity when compared to straight or arch members. The minimally restraining boundary conditions of a torus structure present unique challenges when compared to an arch with pinned or captured ends. The combined biaxial bending, axial and torsional response must be taken into account along with geometric and material nonlinearities and real, measured geometry.

The response of an inflatable, toroidal member subjected to both out-of-plane and in-plane loading was investigated using the modeling tools developed in Chapter 3 and partially validated using straight-tube test data in Section 4.1. The combined loading case was selected because it represents the most complex loading state for the inflatable member and best serves to demonstrate the model response. Demonstration of the beam-based FE modeling approach for the application of torus loading represents a significant jump in complexity from the modeling of straight tube inflatable members as the torus

structure will experience a state of combined bending and axial loading. Given a straight beam element formulation is utilized to model a curved structure, a sufficient mesh refinement is employed to ensure the initial curvature is adequately captured.

In the following section a torus loading methodology that applies both out-of-plane and in-plane loading is described. The torus load test configuration is also described, along with the test specimen that was used for model validation efforts. The beam-based FE model is described in detail and model comparisons with the experimental results are made.

4.2.2 Torus Experimental Setup

In this section the torus experimentation is described. Additional details on the development of torus load testing can be found in Clapp (2017). Whitney (2016) gives additional details of the experimental setup and a description and results of a much more extensive test matrix including other torus configurations. Both the load frame used in the experimentation described here and many of the experimental methods were adapted from previous work with inflatable tori conducted by NASA researchers (Levine 2017).

The torus test load frame was designed to apply in-plane, radial loading to the inflatable torus at discrete loading points. The steel load frame consisted of horizontal top and bottom circular plates, plate support posts and a floor reaction plate, as shown in Figure 4.13.
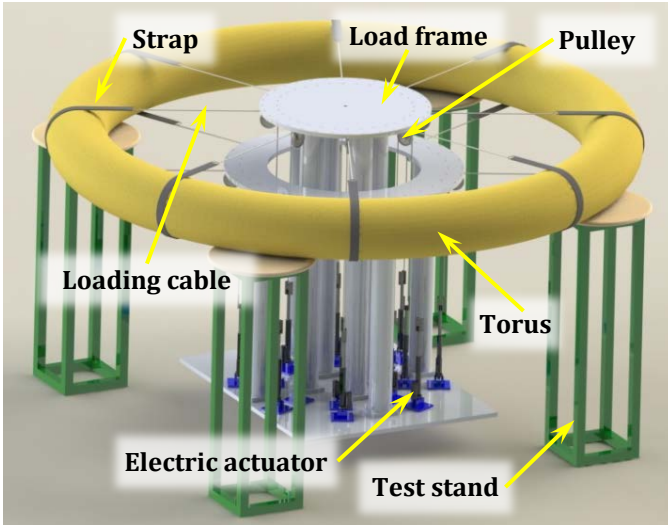
Figure 4.13. Torus test configuration.

Sixteen electric actuators were mounted vertically around the outer perimeter of the floor reaction plate. Pairs of actuators applied load to the top and bottom of the torus cross-section at eight different circumferential locations. The first loading point was located at 11.25° measured counter-clock-wise from the reference axis shown in Figure 4.14. Cables attached to the actuators passed over a pulley attached to the bottom circular reaction plate and radially out towards the inflatable torus member. Each cable was connected to a 50 mm wide fabric strap that was wrapped and bonded around the inflatable torus and returned back towards the load frame. A second cable was attached to the other end of the strap, returned radially to the load frame and sent through a pulley on the top circular reaction plate where it then connected to the second actuator in a pair. Each loading cable included an inline load cell and a string potentiometer that was attached to the cables on the radial side of the pulley to measure radial displacement.
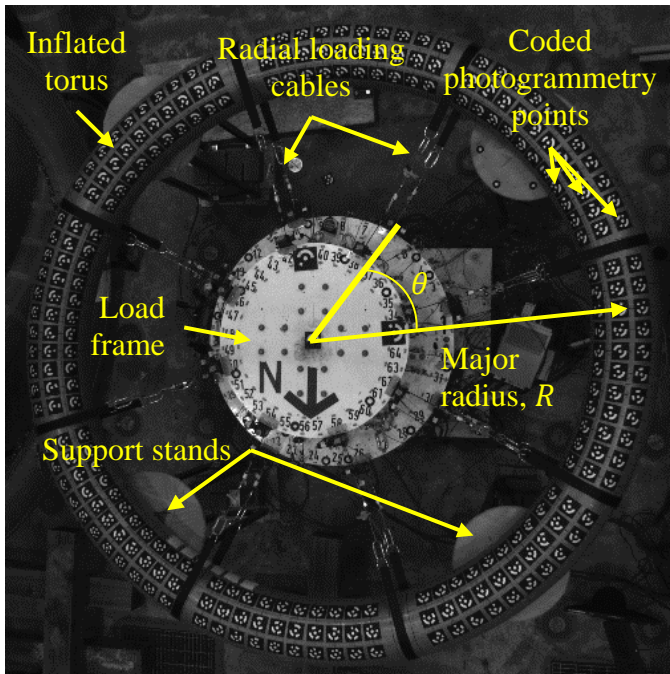
Figure 4.14. Photogrammetry view of test configuration.

The inflated torus was supported vertically by four test stands evenly spaced around the test setup. The diameter of the torus supports was 570 mm and the support centers were located at 34°, 124°, 214° and 304°. Two layers of peel ply release fabric were placed between the supports and the torus to minimize friction.

The location and movement of the individual photogrammetry points (seen in Figure 4.14) in three-dimensional space were tracked throughout the duration of an individual test. The photogrammetry system took pictures of the experimental setup at a rate of 2 Hz. An algorithm was developed to determine the location of the center of the torus cross-section at locations around the circumference of the torus based on the location of the somewhat arbitrarily placed photogrammetry points located on the surface of the torus (Clapp 2017). In this manner the precise location of the torus centerline was tracked throughout the duration of the test for comparison to numerical models.

4.2.3   Description of Specimen and Test

The test article used for model validation purposes was designated as T3AP-3 in Whitney (2016). The geometry is representative of the third torus in the six-meter major diameter HIAD structure that was experimentally investigated by NASA researchers (Cassell et al. 2013). The material system consists of a braided Technora fiber shell with an impermeable urethane gas bladder and is identical to the material system investigated in Clapp et al. (2016a and 2016b) and in previous validation studies. The minor radius of the inflated torus is nominally 170 mm and the braid angle is nominally 71°. The average braid angle, however, was determined to be 69.5° and varied from an average braid angle of 71.8° measured on the inside equator of the torus to 67.4° measured on the outside equator of the torus at 137 kPa of inflation pressure. The average braid angle was within 0.1% of these values at the lowest inflation pressure of 34 kPa. Two Technora axial reinforcing cords, identical to those detailed in Clapp et al. (2016b), were nominally located at ±60° from the inside equator of the torus, as illustrated in Figure 4.15.
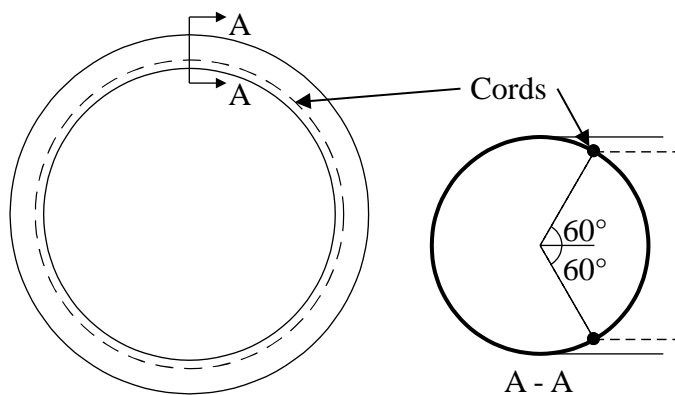
Figure 4.15. Torus and cross-section geometry.

In order to induce significant out-of-plane deformation a torus load test was performed at 103 kPa of inflation pressure. Two sets of hanging weights (2.1 kN each), were initially

applied at opposing points on the torus (at 78.75° and 258.75° measured from the reference axis shown in Figure 4.14). After application of the out-of-plane hanging weights the in-plane loading commenced. Load control was used initially to apply a 44.5 N preload to all of the cables. Once the cables were all properly loaded to the target 44.5 N preload, the displacements of the cables ends were controlled with a linear ramp up to the target cable end displacement at a rate of 12.7 mm per minute.

4.2.4   Analysis

In this section the modeling strategy is described along with the details and parameters of the study performed to partially validate the modeling approach. Developing confidence numerical simulations can produce reasonable predictions of the structural response of an inflated torus to loading is an important step in gaining confidence in the predicted response of a full HIAD system.

4.2.4.1 Description of Torus Modeling

The pressure dependent axial and shear moduli of the braided shell material were obtained through pressurized tension-torsion testing of inflatable specimens with identical material and geometry as in the present study (Clapp et al. 2016a). The extensional and shear properties utilized were 20 and 420 N/mm respectively and include the effect of the impermeable bladder and the geometric stiffening effects that occur when the inflated shell undergoes axial deformation due to a braid angle change (e.g. see Chapter 2).

The cross-section of the member was modeled with two cords at ±60° from the inner equator of the torus, as shown in Figure 4.15. The cord load-strain response was obtained

through tension testing of comparable Technora braided cords. As with previous modeling efforts, the load versus strain response of the cords was taken as the unloading response at loads below the force in the cords due to inflation pressure, while the loading response was assumed at load levels above the force in the cords at inflation pressure and is based on Figure 2.11.

The initial geometric shape of the inflated structure (defined in the R, θ and Z directions per Figure 4.14) was imported directly from photogrammetry measurements of the inflated torus before the application of any load. No initial shape data were collected on the orientation of the cross-section. As such, the cross-section was assumed to be oriented vertically before the application of external loads (with the cords remaining in the nominal locations at ±60° from the inner equatorial axis of the torus).

The four support stands that the torus rested on were modeled as bilinear vertical springs supporting the torus elements from below. The springs had a relatively high compression stiffness (0.5 to 1.2 kN/mm) to limit inter-penetration between the support and torus and a small tension stiffness to allow lift-off (0.18 N/mm). In the out-of-plane loading test a small amount of local compression was observed where the torus contacted the support edge. As such, the compression stiffness of the vertical springs was chosen to obtain the same amount of torus/support inter-penetration observed in testing. Each support was modeled with one spring at each edge of the support (located 570 mm apart). In this manner the torus can contact one or both edges of the support, as in the case of the experimental setup. At the location of the torus supports, the torus elements were further constrained by adding soft tangential and radial springs. Although these elements could be used to approximate the contact friction between the torus and support, the spring

stiffness was kept low enough (0.18 N/mm) to not influence the response of the torus while still providing sufficient numerical constraint to avoid a singular stiffness matrix.

The radial loading cables were attached to the torus by means of rigid link elements. These link elements connected the torus elements, located at the centerline of the inflated torus, to the cable ends and were the length of the minor radius of the torus. In this manner the loading cables were capable of imparting torsional loading to the torus. Radial cable elements returned the link element ends to location of the torus load frame pulleys. The response of the cable elements is described in more detail below. The free cable element ends were constrained vertically and tangentially with stiff axial springs (1.75 kN/mm). The cable ends could then either be unconstrained radially, loaded radially or displaced radially.

Figure 4.16 illustrates a wedge portion of the FE model including torus elements, link elements, loading cables and support and cable end boundary springs. The mesh was refined in order to obtain a convergent load deformation response. For all analyses approximately 100 elements, each with three integration points, were utilized to model the inflatable torus, although convergent results were obtained with significantly fewer elements.

Loading cables

Link

Torus support
boundary
springs

Cable end
boundary
springs

Torus elements
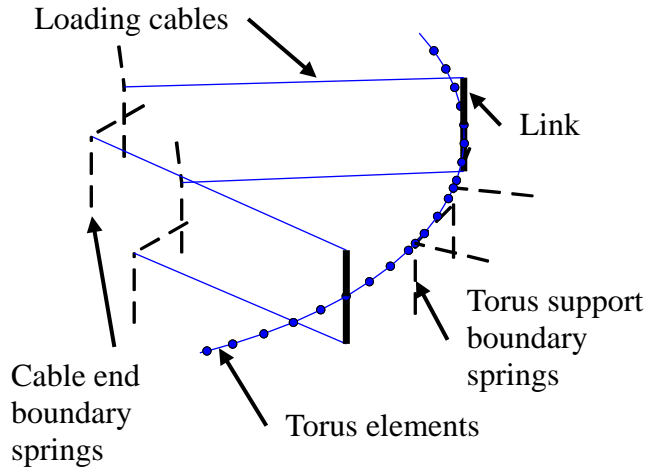
Figure 4.16. Beam-based FE model of torus load test wedge detail.

Three analysis steps were utilized in modeling the out-of-plane torus load test. In the first

step the 2.1 kN out-of-plane loads were applied to the torus model at 78.75° and 258.75°

acting downward. In this step the cable ends were un-constrained and allowed to

translate radially. In the second step the 44.5 kN preload was then applied to each cable

end acting radially inward. In the third and final step the cable ends were displaced

radially inward 43 mm by enforcing the locations of the cable end nodes. In all load

steps Newton iterations were utilized to ensure the model was in a converged state and

adaptive load stepping was implemented in order to reduce computation time (Clarke and

Hancock 1990).

4.2.4.2 Cable Response

One of the greatest challenges with the modeling of the inflatable torus load tests was

providing the correct amount of constraint to the torus during loading. When modeling a

load controlled torus test the response of the torus was under-constrained; the

fundamental ovalization mode of the torus was obtained for all load cases. When

84

modeling a torus test where the displacements of the cable ends were controlled, the radial cable system becomes part of the loaded structure and the relative stiffness of the cable and strap assembly must be accounted for. The radial cable loading assembly consists of steel cable, an inline load cell, connection fittings and the straps that are bonded to the outside of the inflated torus, all in series. In addition to the relative compliance of the loading assembly, the cross-sectional compliance of the inflated torus shell must also be included as the torus member can be indented, compressed or undergo ovalization as the loading strap applies force to the torus.

The nonlinear load-strain response of each cable assembly (including cables, connection hardware, load cells and the torus cross-sectional response) was obtained for the test. The portion of the test of interest was the uniform cable end displacement step. During the 44.5 N preload portion of the test the relative compliance of the cable system is not relevant. From photogrammetry data of the particular test of interest the displacement response of the torus centerline was extracted. The strain of an individual cable assembly ($\varepsilon_{cable-i}$) was then estimated per Equation 4.1.

$$\varepsilon_{cable-i} = \frac{\left(U^{torus}_{radial-i} - U^{cable}_{radial-i}\right)}{L_{cable-i}}. \qquad \text{Equation 4.1}$$

The variable $U^{torus}_{radial-i}$ represents the radial displacement of the torus at the location of the ith cable attachment throughout the loading test. The variable $U^{cable}_{radial-i}$ is the corresponding enforced radial displacement of the cable end throughout the loading test and $L_{cable-i}$ is the initial length of the cable from the torus centerline to the load frame pulley. Cross-sectional rotation or Z displacement of the torus at the point of cable connection was not included in the estimation of cable assembly strain.

Using the force data taken directly from the inline load cell of the cable assembly the load-strain response of each individual cable for each test was constructed from 44.5 N to the final load level recorded in the cable. The response of the cable assembly for the cable end displacement portion of the out-of-plane test is shown in Figure 4.17. At load levels above the maximum value recorded during testing (which may be encountered during modeling of the torus), or when the load level in the cable decreased during the test, a tangent stiffness was utilized. At load levels below 44.5 N a linear stiffness was used that was tangent with the load-strain response at 44.5 N of load. As can be seen from Figure 4.17, the response of the individual cables varies considerably and exhibits a nonlinear force-strain relationship.
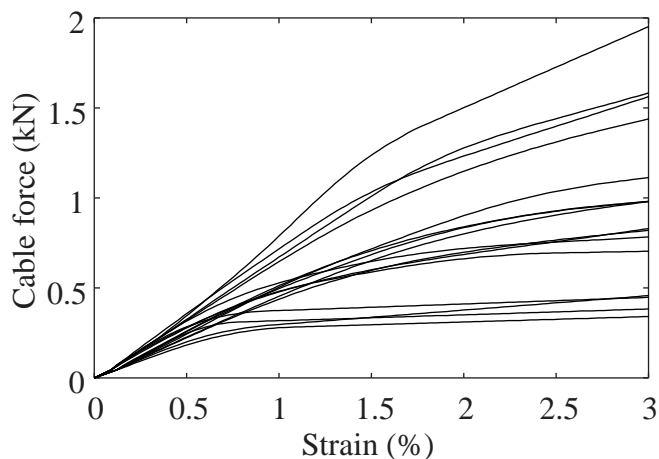
Figure 4.17. Cable assembly response.

The nonlinear load-strain behavior derived from the torus load test was used to simulate the response of the corresponding cables in the torus models. This method provided a means of approximating the torus loading while providing the correct amount of restraint to the torus structure. As will be discussed subsequently, the torus model prediction of

load-deformation response was found to be particularly sensitive to the relative stiffness of the loading cables.

4.2.4.3 Description of Test and Model Output

Before presenting the results of testing and analysis, a description of the test output used for presentation of the results is worthwhile. The load deformation response of the torus is shown as total cable load (calculated as the sum of all cable in-line load cell readings) versus the enforced cable end radial displacement (e.g. see Figure 4.19). The load versus deformation response is presented starting from 712 N of total load (44.5 N of preload per cable) since the cable end displacement prior to the application of the 44.5 N preload is not informative. As the controller works to eliminate slack from the cable and apply the correct amount of preload to the cable end the displacement tended to be large and to fluctuate.

The total cable load versus enforced cable end displacement was chosen to illustrate the gross load-deformation response of the member, although other methodologies were considered. Presenting the total cable load versus average torus radius is another way to present the load-deformation response; however, utilizing the average radius can obscure the higher frequency deformations that occur around the circumference of the torus. Likewise, utilizing a total cable load versus the radial displacement at a particular location on the torus can be informative for a particular test, but it is difficult to make comparisons as different tests may deform in different configurations and the location where the displacement is tracked is arbitrary. Presenting the total cable load versus enforced cable end displacement provided a means of comparing the gross load deformation response of the loaded torus for varying inflation pressures and displacement

levels; however, this approach does neglect to capture the local variations that occur as the torus is loaded.

In order to make comparisons with the response of the torus at a more local level, the R and Z centerline position of the torus versus θ location is also presented at various load levels (e.g. see Figure 4.20). These plots present a more detailed view of the local response of the torus at various load levels; however, the load deformation response of the member is difficult to extract. Both plot types can be used in conjunction to obtain a better understanding of the torus response at various load and displacement levels.

4.2.4.4 Results and Model Comparisons

In the test a rapid drop in load was observed after 43 mm of cable end displacement. The drop in load was caused by a rapid de-bonding of the top internal reinforcing cord to the braided shell as the strap holding the out-of-plane load (at 79°) caused wrinkling and penetrated the braided shell (shown in Figure 4.18). The response of the torus is not shown beyond 43 mm of cable end displacement as reliable displacement measurements were not recorded after the onset of out-of-plane loading strap penetration.

Figure 4.18. Out-of-plane strap/torus penetration, before and after initial wrinkling (Whitney 2016).

The results of analysis and comparisons to the out-of-plane torus load test are shown below. Figure 4.19 presents the total cable load versus enforced cable end displacement results for the test and model with all nominal inputs, as described previously. Also shown are results of additional analyses that will be discussed subsequently.
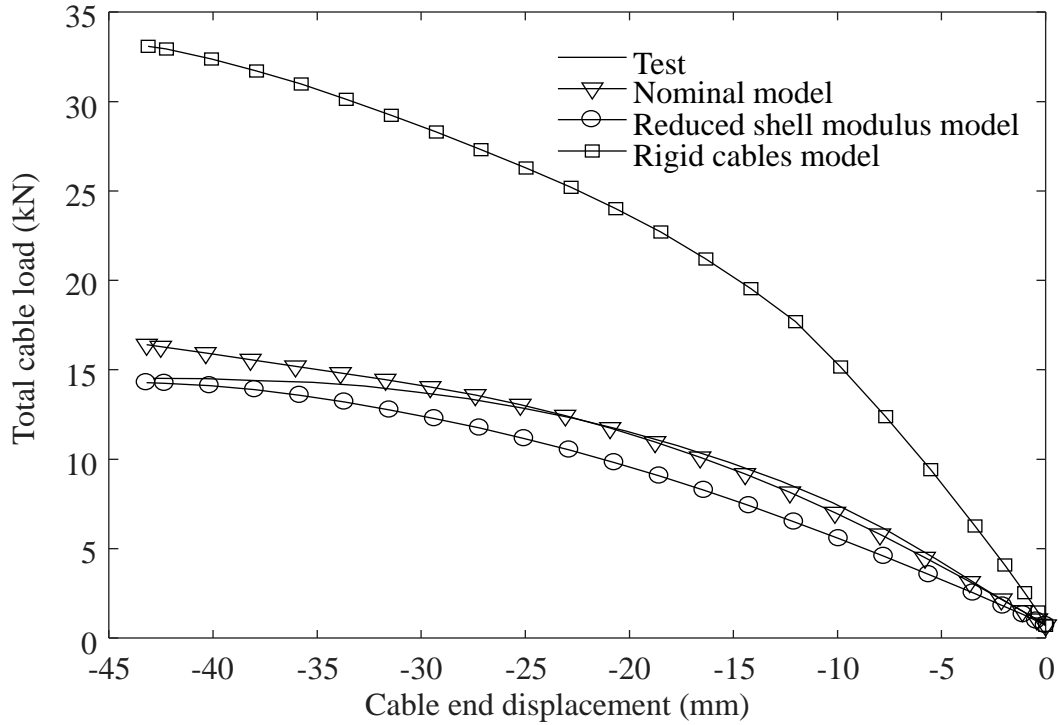
Figure 4.19. Torus out-of-plane load testing with model comparisons.

The nominal model appears to track the test results well, although it somewhat over-predicts the final load. The R and Z position versus θ location of the modeling results is shown in Figure 4.20. The R and Z shape of the torus specimen and model is shown with no external load, after the application of the out-of-plane load and after the application of both the out-of-plane and in-plane loading.
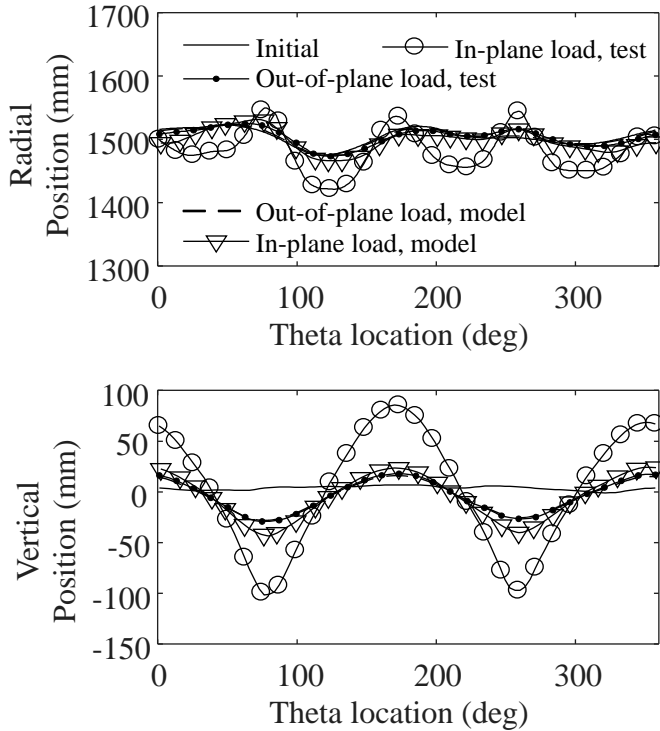
Figure 4.20. Torus test and nominal model R and Z position versus θ location at no external load, after the application of the out-of-plane load and after the application of the in-plane load.

The out-of-plane shape is captured by the model after the application of out-of-plane loading. However, the shape of the torus after the application of in-plane cable end displacements is under-predicted (both in-plane and out-of-plane). Although the initial shape of the torus prior to loading is utilized as the initial shape of the model, it is postulated that because at the time of testing the torus specimen had experienced significant load cycling that there was likely damage to the textile braid and bladder, or interface between the two, that was not accounted for by simply using the measured initial shape. Progressive amounts of damage were visible in the stiffness and final load response as gradually increasing levels of cable end displacement were applied to the specimen (Whitney 2016), although no damage was visible on the torus structure. The

analysis was rerun utilizing only the contribution of the braid gross extensional stiffness that is due to geometric changes that the braid experiences as it undergoes a longitudinal strain (7 N/mm). The fiber tows that made up the braided shell were assumed to be capable of rotating freely. The *R* and *Z* position versus *θ* location results, Figure 4.21, agree with the tested response significantly more favorably.
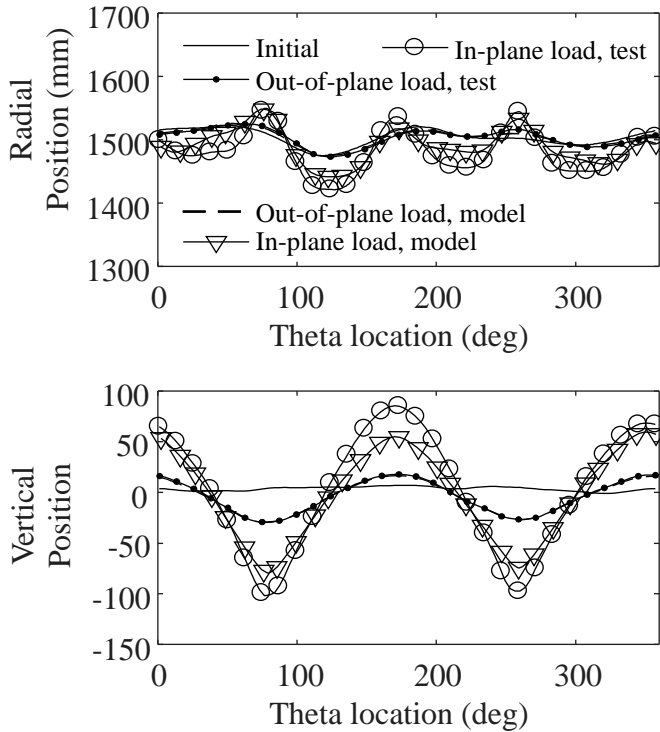
Figure 4.21. Torus test and model *R* and *Z* position versus *θ* location for torus with geometric contribution to braid stiffness only.

The final shape is still somewhat under-predicted, but the model captures the gross in-plane and out-of-plane response of the torus when loading is applied. The magnitude of out-of-plane displacement increases in a similar manner for both the test specimen and modeling results from the out-of-plane load state to the in-plane load state; the model's ability to predict the large load magnification is important. As can be seen from Figure

4.19 the load deformation response of the torus is captured by the modified model reasonably well, with a final cable load discrepancy of less than 2%.

An analysis was also conducted using the nominal torus model and rigid cables, rather than the cable response derived from torus testing (Equation 4.1 and Figure 4.17) to demonstrate the sensitivity of the results to the stiffness of the restraining cables. Although the final shape of the torus (not shown) is more in-line with the response of the model with a modified shell modulus, the final load is severely over-predicted (a 128% increase in final total cable load), as is evident in Figure 4.19. The rigid cable model shown in Figure 4.19 illustrates the importance of utilizing a reasonable cable response. In the case of displacement controlled tests and analyses, the loading cables become part of the structural response. The cables serve to apply boundaries to the torus and constrain the structure in a way that cannot be approximated by assuming the cables are rigid.

Finally, the response of the nominal torus model was analyzed using load-controlled (rather than displacement controlled), solution schemes. In the first case uniform cable loads were applied. In the second case the measured cable loads from testing were applied to the corresponding cables in the model. The final load level applied to the model agrees with the final load level measured in testing in both cases; however, the R position versus θ location results, Figure 4.22, show a significant difference between in-plane torus test and model shapes. The final shapes of both load controlled models have taken a fundamental, ovalized shape.
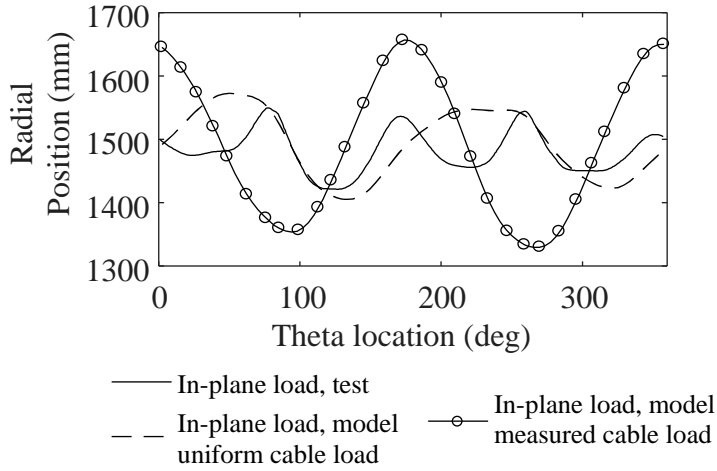
Figure 4.22. Torus test and model R position versus θ location for nominal torus and load controlled modeling schemes after the application of in-plane loads.

The ovalization of the torus models is also apparent in the true-scale illustration of the torus centerline final shapes, shown in Figure 4.23.
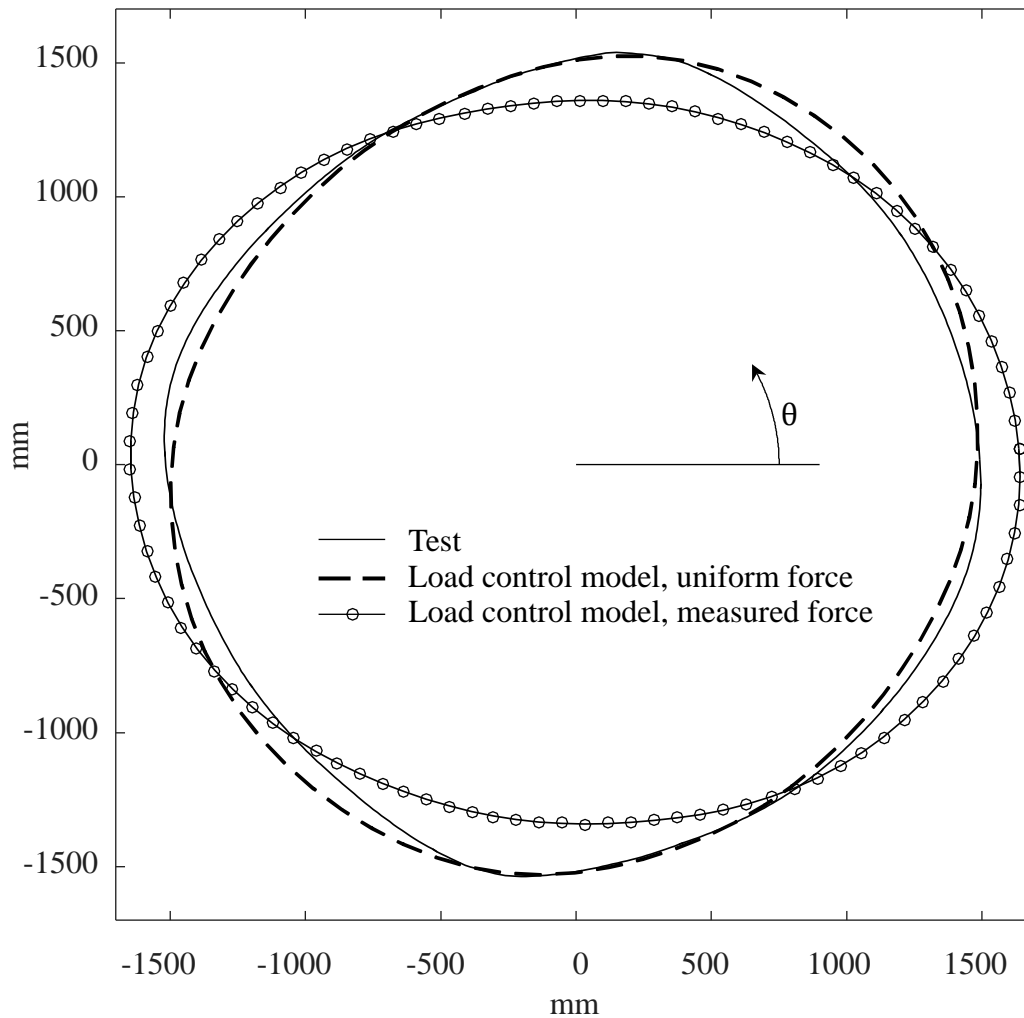
Figure 4.23. Final in-plane torus shape from test and load controlled modeling.

Although a load controlled test may be of interest, displacement control was found to be the most repeatable and predictable, given experimental constraints. When modeling the torus structure in load control the correct level of constraint is not applied to the torus and the lowest energy mode shape is obtained.

4.3   Summary and Recommendations

The modeling tools that have been developed for the analysis of slender, inflatable members with axial reinforcing cords have been shown to be able to adequately capture

the experimental load-deformation response of both beams and tori. Torus load testing included both in-plane and out-of-plane loading and put the inflated member into a complex combined load state, including axial, bending, shear and torsional loading. In the real HIAD system, the adjacent tori support and brace each other and the load state consists primarily of a distributed load around the circumference of the torus. Although the load state produced in the out-of-plane torus test is not representative of real HIAD loading, it serves as a validation test case for the modeling tools and analysis methodologies.

A number of challenges were encountered in the analysis of the out-of-plane torus test. The model was found to be sensitive to boundary conditions, the loading cable stiffness and distribution, loading methodology and initial torus shape. Although the beam-based FE modeling tools were used to analyze the torus load test, it should be noted that the challenges that were encountered are not exclusive to the beam-based FE analysis methodology and are encountered with shell-based FE models of the torus system as well. The challenges are driven by the unrestrained nature of the torus test and the sensitivity of the system to imperfections and variability. Improvements to the torus load testing methodology may include incorporating a reliable load control scheme. The decision to execute the tests using a displacement control of the cable ends loading scheme was driven primarily by the limitations of the electric actuators' actuation speed and the need for a reliable and repeatable control variable for input and comparison with numerical models. Although the displacement control scheme provided the reliability that was desired, the system became much more sensitive to the relative stiffness and variability of the loading cables, as discussed previously, and tended to drive specific

deformation modes. Future refinements to the torus load testing and analysis program may include refining the load control scheme, perhaps by significantly decreasing the rate of loading. With a load controlled methodology applied to the torus tests the in-plane displaced shapes will likely become more varied and sensitive to the initial shape. It should be ensured that the initial shape of the torus member is well quantified. In addition to measuring the centerline location of the member, the initial cross-sectional rotation and precise location of the axial reinforcing cords should also be measured. Finally, the inflatable members are susceptible to damage and a degradation of properties, as was observed in the current study. Modeling results should compare to the first extreme loading cycle whenever possible.

Having successfully modeled component level testing of straight tubes and toroidal members, the modeling tools are extended to analyze the full HIAD structure in the following chapter.

Chapter 5

FINITE ELEMENT MODEL VALIDATION: HIAD LEVEL

HIAD structure modeling efforts have utilized a shell-based FE modeling approach with pressure follower forces and both implicit (Li et al. 2015; Lindell et al. 2006) and explicit (Lyle 2014 and 2015) solution schemes. Although these approaches can predict the response of the HIAD structure subjected to pressure loading, they are time consuming to develop, computationally expensive and can often take days to run. Applying the beam-based FE modeling methodology to the analysis of a full HIAD structure is a significant departure from previous HIAD modeling efforts. Further, modeling a full HIAD structure represents a large increase in complexity from the modeling of single, inflatable components. In modeling multiple tori, the interaction between the inflatable members must be accounted for. The straps that connect the tori to each other and to the relatively rigid center-body must also be included. The beam-based FE modeling methodology under development has been partially validated using straight-tube and torus experimentation of braided, inflatable, slender members with axial reinforcing cords located at discrete locations around the cross-section of the member as detailed in Chapter 4. The modeling methodology is further validated by comparing the results of load testing on a full HIAD structure.

5.1   Description of Tests

NASA researchers (Swanson et al. 2015) developed a testing methodology to apply a uniform pressure load to a HIAD structure. Although a uniform pressure load case is not representative of aero loading on the structure during atmospheric reentry, this load case can be used to assess a particular HIAD configuration and can serve as validation for the

development of various modeling schemes. A picture of the HIAD pressure tub test configuration is shown in Figure 5.1 along with the 3.7 meter major diameter HIAD specimen that will be the focus of validation efforts for the beam-based modeling approach. The fore side of the HIAD structure is visible in Figure 5.1. Also shown are the various strap types and components of the structure and test configuration that will be described subsequently.
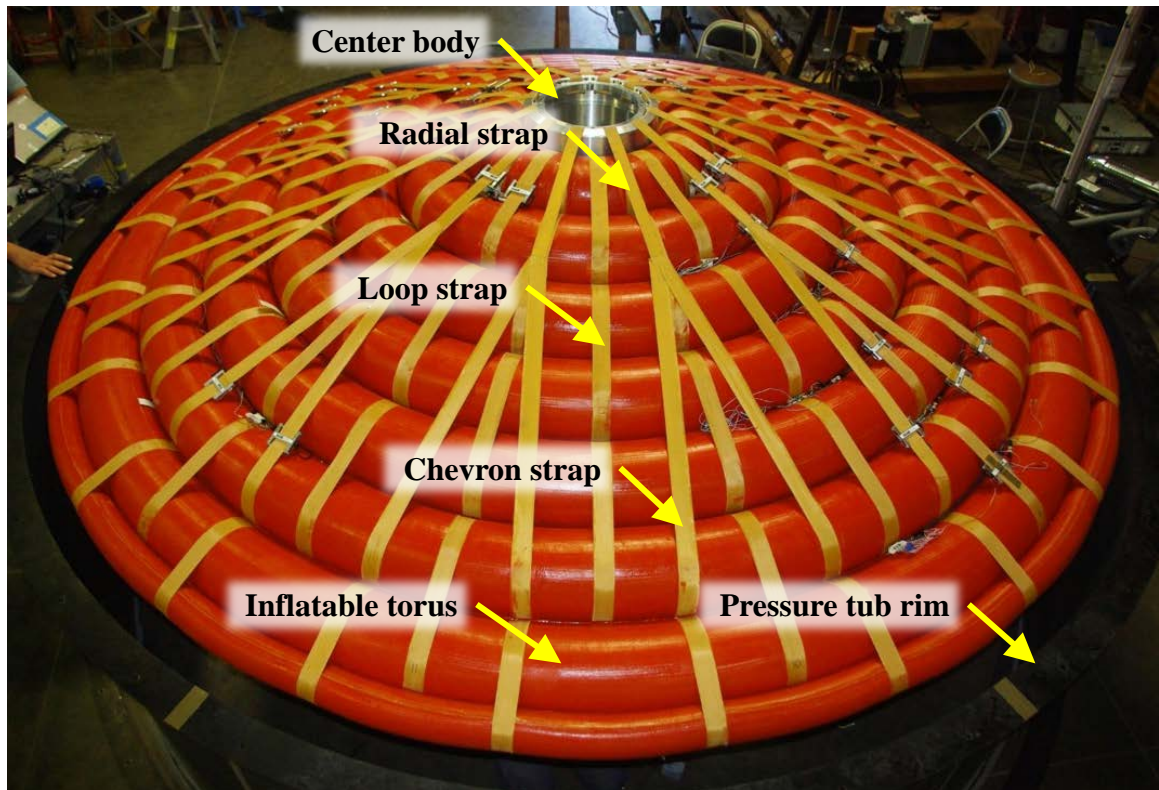
Figure 5.1. 3.7 meter HIAD specimen and pressure tub (Swanson et al. 2015).

The HIAD structure was strapped to the center-body structure, as in a typical deployment. The center-body was firmly mounted to the floor with an inline load cell to measure vertical reaction. A steel skirt that was sealed to the floor encompassed the outer torus of the HIAD structure (visible in Figure 5.1). An impermeable membrane was then draped over the outside of the HIAD structure and sealed to the upper rim of the skirt.

To apply a uniform pressure load to the outer, or fore, side of the HIAD structure the air

encapsulated by the skirt and outer membrane was evacuated, creating a pressure

differential between the fore and aft faces of the HIAD. The atmospheric pressure then

applied a uniform, positive pressure load on the fore side of the HIAD. The internal

inflation pressure (gauge pressure) of the tori on the depressurized side of the membrane

was regulated at the nominal inflation pressure throughout the duration of the test. The

vertical reaction of the loaded structure on the center-body was recorded throughout the

duration of the test, along with the loads in individual straps. The experimental results

that are shown in subsequent sections are not based on the first experimental run of a

pristine specimen, although the loads applied in previous runs were not to the level that

permanent damage would be expected. The deformed shape of the aeroshell was tracked

using string potentiometers at discrete locations and a laser scanner over the fore surface

of the HIAD.

5.2   Description of Test Article

The 3.7 meter major diameter HIAD test article is shown in Figure 5.1. The structure

consisted of eight inflatable tori. Tori T1 (the torus closest to the center-body) through

T7 (the seventh torus from the center-body) all had minor diameters of 251 mm. Torus

T8 had a minor diameter of 89 mm. A plan view of the 3.7 meter HIAD configuration is

shown in Figure 5.2. A cylindrical coordinate system will generally be used to describe

the HIAD structure. The R axis is aligned perpendicular to the longitudinal axis of the

tori. The Z axis is perpendicular to the R axis and is out of the page in Figure 5.2. The θ

axis sweeps about the positive Z axis with counter-clockwise taken as positive.
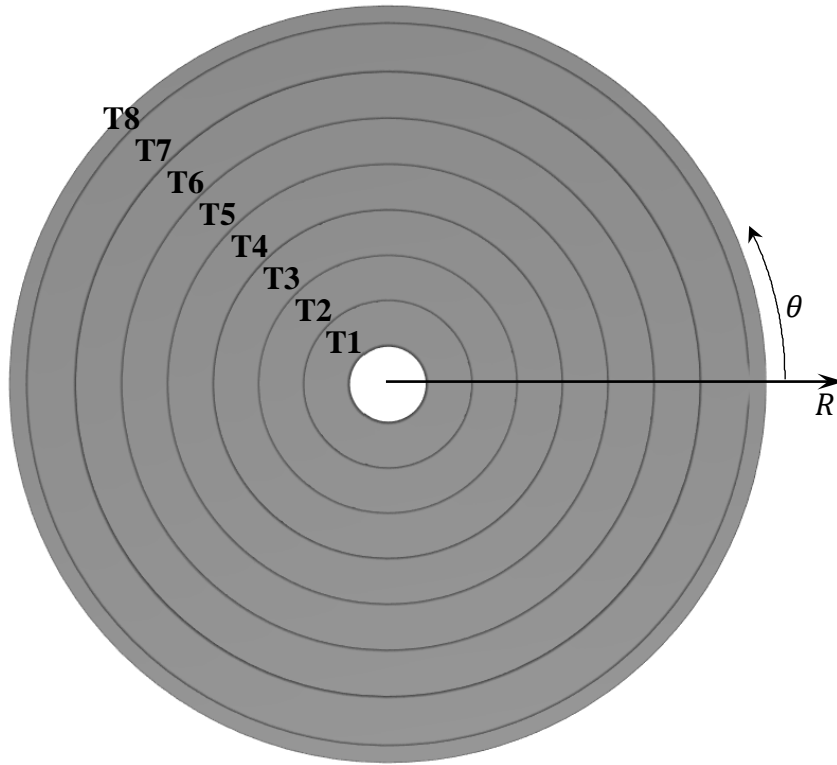
Figure 5.2. 3.7 meter HIAD plan view.

A cross-section of the 3.7 meter HIAD structure is shown in Figure 5.3. The tori were

configured at a 20° angle from the horizontal (R) axis. In Figure 5.3 the tori are shown

overlapping each other and overlapping the center-body. In the actualHIAD specimen

this interference caused the tori to compress against each other and against the center-

body, creating some amount of prestress in the tori and straps before any loading was

applied. The inflation pressure for all tori in the test of interest was 83 kPa.
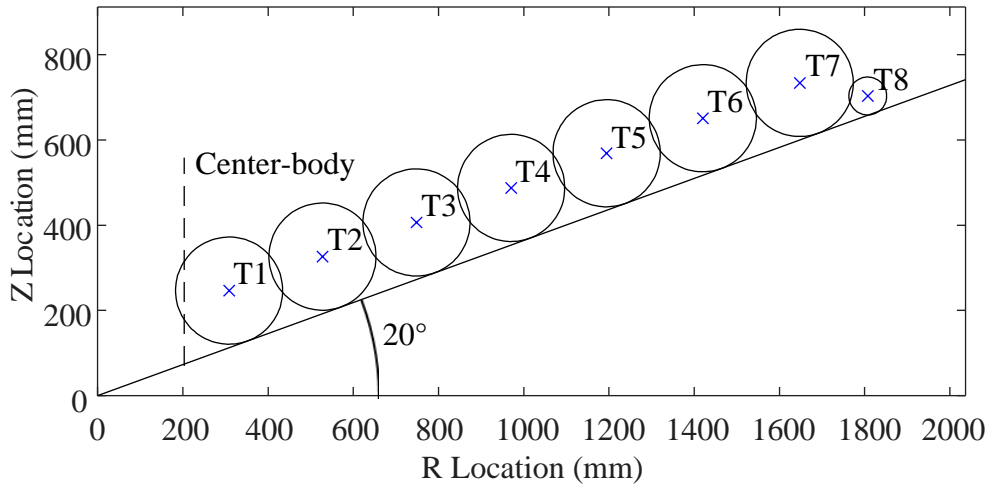
Figure 5.3. 3.7 meter HIAD cross-section.

The cross-section shown in Figure 5.3 is arbitrarily taken at $\theta = 0°$. It should be noted

that the configuration of the HIAD structure in Figure 5.3, and in all subsequent analyses,

places the point of the cone shape at the origin. The positive Z axis is aligned with the

axis of radial symmetry. This convention, although arguably backwards for the pressure

tub tests, was adopted based on previous HIAD reentry analyses conducted by others

where the orientation of the structure is nose down.

The individual tori are a similar construction to the straight tubes and individual torus

discussed previously. As with the torus article discussed in Section 4.2, each torus has

two cords located at $\pm 60°$ from the inner equatorial axis and the nominal braid angle of

the shell is 71°. Unlike the components discussed previously, the braid and cord material

is now Zylon, rather than Technora. Additional tension/torsion testing of an inflatable

Zylon tube with identical material and geometry as in the 3.7 meter HIAD structure was

conducted (Clapp 2017). The longitudinal modulus of the shell was found to be 15.7

N/mm and the shear modulus of the shell was found to be 700 N/mm. Additional Zylon

cord testing was also conducted by NASA researchers.

102

The tori are connected to each other and to the center-body with straps, as can be seen in Figure 5.1. The straps are made of a woven Zylon material. The strap configuration on the 3.7 meter HIAD specimen was composed of three different strap sets: loop straps, radial straps and chevron straps (as shown in Figure 5.1). Loop straps connected an individual torus to adjacent tori or back to the center-body in the case of T1. Radial straps connected the center-body to a set of chevron straps, and the chevron straps connected radial straps on the fore side of the structure to radial straps on the aft side of the structure. All straps were made of Zylon material which was also tension tested by NASA researchers.

The configuration of the loop straps is detailed in Table 2.1. The strap set number, number of straps within the set, θ location of the first strap and strap connectivities are shown. The individual straps within a strap set were evenly spaced around the circumference of the HIAD structure. The target loop strap prestress was 0.22 kN. In cases where the initial strap load level was recorded, the recorded value is shown.

Table 5.1. Loop strap configurations.

Strap set	Number of straps	Location of first strap (deg.)	Connection	Strap preload (kN)
1	12	15	Center-body to T1	0.22
2	12	15	T2 to T3	0.22
3	12	15	T4 to T5	0.31
4	12	15	T6 to T7	0.27
5	12	0	T1 to T2	0.16
6	12	0	T3 to T4	0.27
7	12	0	T5 to T6	0.27
8	24	7.5	T7 to T8	0.22

There were a total of 12 radial straps on the fore side of the HIAD and 12 radial straps on the aft side of the HIAD. The first fore radial strap was located at $\theta = 15°$ and the first aft radial strap was located at $0°$ (fore and aft radials were staggered around the circumference of the HIAD). The radial straps were connected to the HIAD center-body and extended to the midpoint between the T2 and T3 torus. The radial strap target pretensioned was 0.44 kN, however an initial pretension of 0.18 kN was recorded.

The chevron straps were the only straps that were not aligned with the R axis. A given chevron strap started at the terminal end of an aft radial strap, extended over torus T6 and returned to the terminal end of the next fore radial strap, sweeping a total of $\theta = 15°$ in the process. A corresponding chevron then started at the same fore radial strap, extended over T6 and returned to the terminal end of the next aft radial strap. In this manner each fore radial strap was connected to the adjacent aft radial straps, and each aft radial strap

was connected to the adjacent fore radial straps. The chevron straps were in series with the radial straps and developed approximately half of the radial strap pretension (0.09 kN).

5.3   Description of Beam-Based Finite Element Model

Modeling the full HIAD system using a beam-based FE modeling approach represents a significant and novel departure from previous, shell-based FE modeling strategies. Further, the development of beam-based FE analyses is a significant increase in model complexity from component level analyses.

Modeling the full HIAD system using a beam-based FE modeling approach requires the use of inflatable torus elements, interaction elements to capture the response between tori, strap elements to represent the loop, radial and chevron straps, and link elements to connect straps and tori. In addition to describing the various element types that are used in modeling the full HIAD system, a description of the boundary conditions, loading and solution schemes that were employed are also included.

5.3.1   Torus Elements

The elements representing the inflatable torus members were the three-dimensional, corotational, flexibility-based beam elements that were previously detailed in Chapter 3 and applied to the analysis of straight and toroidal members in previous validation efforts. Tori T1 through T7 were specified with a minor diameter of 251 mm and torus T8 was specified with a minor diameter of 89 mm. The R and Z locations of the torus cross sections were specified as detailed in Table 5.2 and also as shown in Figure 5.3. The internal inflation pressure was specified as 83 kPa for each torus.

Table 5.2. Configuration of tori, 3.7 meter HIAD article.

Torus	*R* location (mm)	*Z* location (mm)	Minor diameter (mm)	Inflation pressure (kPa)
T1	308.6	246.6	251	83
T2	527.5	36.2	251	83
T3	748.1	406.5	251	83
T4	970.4	487.5	251	83
T5	1194.5	569.0	251	83
T6	1420.2	651.2	251	83
T7	1647.6	733.9	251	83
T8	1807.2	703.2	89	83

A shell braid angle of 69° degrees was utilized based on previous experience with nominally 71° braided members in the curved configuration (see Section 4.2.3). The measured extensional and shear stiffness of the braided shell were utilized as model inputs (15.7 and 700 N/mm, respectively). The additional longitudinal stiffness due to the geometric changes that the braided shell undergoes when subjected to an axial strain was also included in the typical manner (Equation 2.30, the gross extensional modulus was 20.4 N/mm for tori T1 through T7 and 17.4 N/mm for the shoulder torus, T8).

Two axial reinforcing cords were located at ±60° from the inner equatorial axis of each torus. The cord response was derived from tension testing of Zylon cords conducted by NASA researchers. The cord specimens were identical to the cords used in the 3.7 meter HIAD test specimen. The cord force at 83 kPa of inflation pressure was calculated to be

1.44 kN for tori T1 through T7, and 0.18 kN for T8 based on Equation 2.17. The idealized load-strain response is shown in Figure 5.4, below.
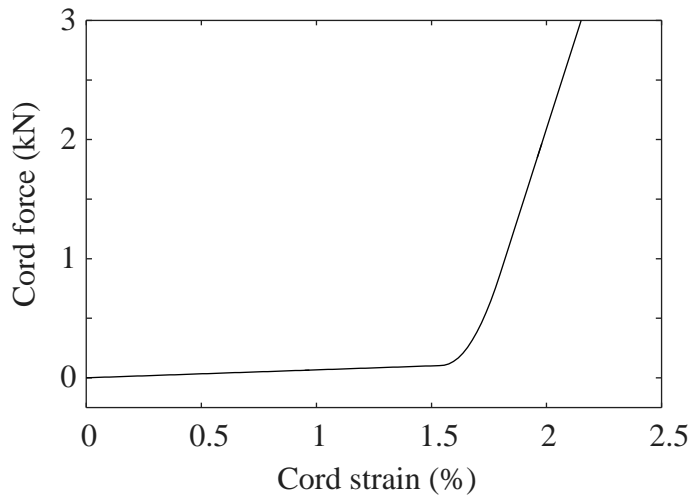
Figure 5.4. Idealized load versus strain response of Zylon cords.

Each torus was modeled as geometrically perfect. It is not expected that the HIAD system will have the same sensitivity to geometric imperfections as an individual torus structure, since in a full HIAD stack adjacent tori brace each other and mitigate the influence of an initially imperfect geometry. A total of 144 straight beam elements were utilized per torus, although a converged solution could be obtained with significantly fewer elements.

5.3.2   Interaction Elements

Although the beam elements that make up the inflatable torus members can simulate the axial, bending, shear and torsional response of the members, they cannot simulate the stiffness of the members perpendicular to the longitudinal axis. This component of stiffness is important to simulate the response of the HIAD because each torus is compressed against adjacent tori, both in the unloaded state and as the structure is loaded.

Interaction elements are used in the beam-base FE model of the HIAD system in order to simulate this cross-direction stiffness of the inflatable members, and to tie adjacent tori together. Each interaction element goes from the centroid of the cross-section of a given torus to the centroid of the cross-section of the adjacent torus, and is aligned with the R axis. Each torus is modeled with the same number of nodes, located at the same θ locations in order to accommodate the alignment of interaction elements. Interaction elements also tie torus T1 back to the center-body, for the 3.7 meter HIAD located at $R = 203.2$ mm and $Z = 246.6$ mm. The interaction elements employ three dimensional, corotational elements with a linear elastic material model.

The axial stiffness and bending rigidity of the interaction elements must be chosen to approximate the cross-section compression and shear stiffness of the inflatable members. The properties are linearized about the inflated state although future refinements may incorporate a nonlinear response, including separation between tori. Both the axial and flexural rigidity of the interaction elements are determined based on a unit length of the inflatable member undergoing deformations due to either a cross-direction compression or shear, respectively.

The axial rigidity of an interaction element can be estimated by considering a cylindrical member with inflation pressure p, subjected to two opposing compressive pressures (f), a cross-section of which is shown in Figure 5.5.
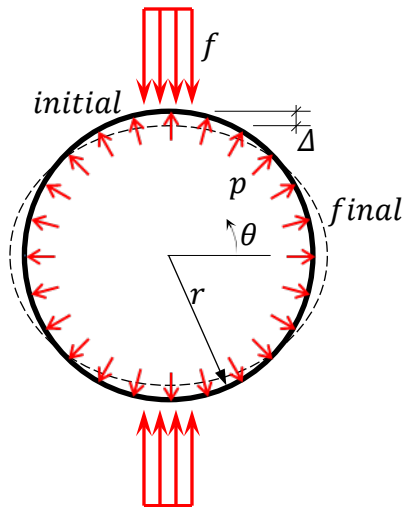
Figure 5.5. Cross-section of inflated member subjected to opposing compressive pressures.

The compressive stiffness of the member cross-section is determined using a FE sub-model. A unit width of the torus cross section is modeled using beam elements. The axial stiffness of the elements is specified as a high value (7 GPa), while the bending rigidity is very low (0.7 kPa). The values were chosen to model the textile shell as inextensible and the response of the sub-model was not sensitive to changes in these values. Quarter symmetric boundary conditions were employed at the planes of symmetry (at $\theta = 0$ and $\theta = \frac{\pi}{2}$). All out-of-plane degrees of freedom were also constrained. A minimum of 30 nodes were used to model the quarter cross-section, although convergent results could be obtained with significantly fewer elements. Large deformations were assumed, and all loads including the internal pressure were modeled as follower forces.

In the first loading step, pressure follower forces were applied to the nodes in order to simulate the internal inflation pressure. After equilibrium was achieved at the desired

inflation pressure, a small horizontal pressure (f with units of force/length^2) was applied to the apex nodes of the model within a width of $0.1r$. After convergence of the second step the vertical displacement of the apex (Δ) was obtained and a stiffness of the entire cross-section was determined from the quarter symmetric model,

$$k_{ax} = \frac{0.2rf}{2\Delta}.$$
<div align="right">Equation 5.1</div>

The convergent cross-section compressive stiffness was found to be independent of the minor radius of the cross-section and is equivalent to,

$$k_{ax} = 0.35\pi p.$$
<div align="right">Equation 5.2</div>

The units of the stiffness value are force/length/length as a unit width of the member was considered.

A similar calculation can be performed using the principle of virtual work and assuming the displaced shape of the deformed cross-section. The following re-derivation of the axial stiffness is provided for illustrative purposes. The final axial stiffness of the inflatable member cross-section derived below was not used in subsequent FE analyses as the assumed compressed shape of the cross-section over-constrains the member's response and produces an overly-stiff result.

The initial volume of a unit slice of the member cross-section is simply πr^2. A line load is assumed to be applied to the apex of member (f, with units of force/length). It is assumed that the cross-section of the member ovalizes a small amount (Δ) when loaded and that the circumferential shell is non-extensible. The final volume of the unit slice is then,

$$V_f = \pi(r + \Delta)(r - \Delta) = \pi r^2 - \pi \Delta^2, \qquad \text{Equation 5.3}$$

and the change in volume is $-\pi\Delta^2$. The total work on the unit slice due to the externally

applied line load undergoing a deformation (Δ), and the internal inflation pressure

undergoing a volume change is,

$$W = 2f\Delta - p\pi\Delta^2. \qquad \text{Equation 5.4}$$

Applying the principal of virtual work by taking the variation of the location of the force

with a virtual change in deformation and the variation of the internal inflation pressure

undergoing a virtual volume change, and setting the subsequent expression to zero yields,

$$\delta U = 2f\delta\Delta - 2p\pi\Delta\delta\Delta = 0. \qquad \text{Equation 5.5}$$

The axial stiffness of the inflatable member cross-section ($k_{ax} = f/2\Delta$) is then,

$$k_{ax} = 0.5\pi p. \qquad \text{Equation 5.6}$$

The units of the stiffness value are again force/length/length because a unit width of the

member is considered. When Equation 5.6 is compared to Equation 5.2 it is clear that the

axial response derived from the principle of virtual work is stiffer compared to the result

obtained from the FE analysis (due to over-constraining the deformed shape). Although

the axial stiffness value derived above is not used in subsequent analyses, it serves to

illustrate the response driver and the cross-sectional stiffness's independence of the minor

radius when the linearized stiffness of the cross-section is used.

A similar, shear stiffness for the cross-section of the member was determined. Figure 5.6

illustrates the configuration of the shear virtual test.
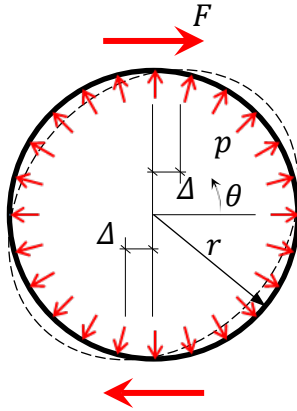
Figure 5.6. Cross-section of inflated member subjected to shear loading.

A unit width of the torus cross section was again modeled using beam elements with the same convergent properties. Anti-symmetry was employed with pin boundary conditions at the plane of symmetry (at $\theta = 0$ and $\theta = \pi$). All out-of-plane degrees of freedom were again constrained. A minimum of 30 nodes were used to model the half cross-section, although convergent results could be obtained with significantly fewer elements.

In the first loading step, pressure follower forces were again applied to the nodes in order to simulate the internal inflation pressure. After equilibrium was achieved at the desired inflation pressure, a small horizontal load (F with units of force/length) was applied to the apex node of the model. After convergence of the second step the horizontal displacement of the apex node (Δ) is obtained and a stiffness of the entire cross-section was determined,

$$k_v = \frac{F}{2\Delta}.$$

<div align="right">Equation 5.7</div>

Like the compression stiffness of the cross-section, the shear stiffness was found to be

only a function of internal inflation pressure and not the minor radius,

$$k_v = 0.72\pi p.$$ Equation 5.8

The axial and shear stiffness of the tori were then used to calculate the axial and bending

rigidity of the interaction elements. The stiffness between two tori was determined by

considering two halves of the adjacent tori and calculating an equivalent, effective

stiffness of the members in series. The configuration that was used to calculate the

effective axial and bending rigidity is shown in Figure 5.7. In the case of T1 there was no

adjacent torus and the adjacent center-body was assumed to be infinitely rigid. A factor

of two was used in the case of the axial stiffness of each torus half because the length of

each component is half the length of the member that was used to calculate k_{ax} (Equation

5.2) and axial stiffness is inversely proportional to length. A factor of eight was used in

the case of k_v for each torus half because bending stiffness is inversely proportional to
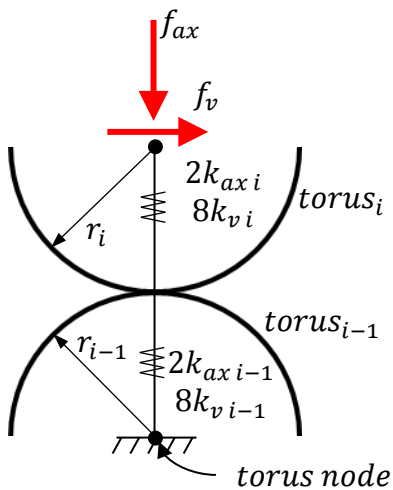
length cubed.

Figure 5.7. Cross-section of inflated member subjected to axial and shear loads.

Calculating the axial rigidity between the two tori is accomplished by finding the equivalent stiffness of the two half-sections in series,

$$k_{ax\,eq-i} = [(2k_{ax\,i-1})^{-1} + (2k_{ax\,i})^{-1}]^{-1}.$$

Equation 5.9

The equivalent axial rigidity is then,

$$EA_{eq-i} = k_{ax\,eq-i}(r_{i-1} + r_i)l.$$

Equation 5.10

The value l is the tributary width of the interaction element along the circumference of the torus and is a function of the number of nodes per torus that are used in the analysis (N) and the major radius of the torus (R_i, Table 5.2),

$$l = 2\pi \frac{R_i}{N}.$$

Equation 5.11

The shear stiffness of one cross-section is modeled as a cantilever beam with a length equal to the minor diameter of the torus. To calculate the effective or equivalent stiffness between adjacent tori, two half-sections in series are again considered (Figure 5.7). Each half-cantilever stiffness is derived from the stiffness of adjacent tori. The cantilever stiffness of the half-torus section is eight times larger than the stiffness of the full-torus section found in Equation 5.8 because the bending stiffness is inversely proportional to length cubed. When the effective member is subjected to a unit load the total tip deflection (Δ_{total}) is a result of the cantilever deflection of both torus cross-section halves,

$$\Delta_1 = \frac{1}{8k_{i-1}} \;\; and$$

Equation 5.12

$$\Delta_2 = \frac{1}{8k_i},$$

Equation 5.13

114

the rigid body rotation and translation of section i caused by translating the unit load f_v

from the tip of the cantilever to the end of r_{i-1},

$$\Delta_3 = \frac{3r_i}{16k_{i-1}r_i}, and$$

Equation 5.14

the rigid body rotation and translation of section i caused by the moment that is produced

when translating the unit load f_v from the tip of the cantilever to the end of r_{i-1},

$$\Delta_4 = \frac{3r_i{}^2}{8k_{i-1}r_{i-1}{}^2}.$$

Equation 5.15

The total tip deflection is then,

$$\Delta_{total} = \Delta_1 + \Delta_2 + \Delta_3 + \Delta_4.$$

Equation 5.16

The equivalent bending rigidity of the cantilevered interaction element can then be

calculated,

$$EI_{eq-i} = \frac{(r_i + r_{i-1})^3}{3\Delta_{total}}l.$$

Equation 5.17

The equivalent axial and bending stiffness of the interaction elements will be equivalent

to the axial and bending stiffness of one of the tori when the two adjacent tori are

identical. The equivalent bending rigidity of the interaction element is used for the out-

of-plane stiffness of the element (perpendicular to HIAD cone). The in-plane (aligned

with the θ direction of the HIAD) and torsional stiffness of the interaction elements are

specified as relatively rigid. Torsional displacement of a torus relative to adjacent tori is

not expected to drive the response of the HIAD as the friction between tori provides a

significant amount of stiffness and HIAD aero-loading does not tend to rotate the tori

relative to each other.

The purpose of the interaction elements is to tie adjacent tori together and provide a reasonable approximation of the stiffness between tori. Although there is opportunity for improving the interaction element material models that are utilized, the model has been found to not be highly sensitive to variation in the interaction element stiffness, as will be shown subsequently.

5.3.3   Link Elements

In the real HIAD structure, straps wrap around the tori and are either connected back to themselves, to other straps or to the center-body. In a shell-based FE modeling approach the straps can be modeled as wrapping around the tori. Straps are either boded to the torus shell using constraints or friction is defined between the strap and the torus shell surfaces. In a beam-based modeling approach the straps cannot be modeled as wrapping around the torus because the nodes are aligned along a one-dimensional axis and there is no diameter for the straps to wrap around. Instead, link elements are utilized in a similar manner to the link elements utilized in modeling the response of torus load testing (Section 4.2). Figure 5.8 illustrates the cross-section of a torus member at the location of a strap set.
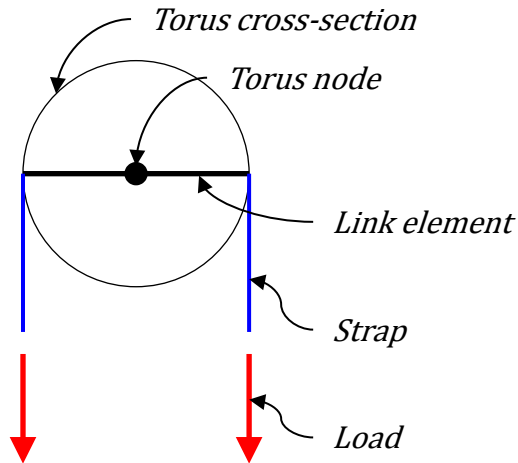
Figure 5.8. Cross-section of an inflated member with link elements.

For a set of loop straps, two link elements extended from the torus node to the shell of the torus cross-section (the length of each element is equal to the minor radius of the torus cross-section). In this manner differential strap loading could apply a torsional load to the inflatable torus, as in the real structure. The geometry of all strap sets was specified such that they are tangent to the cross-sections of the tori.

In the current modeling efforts, the link elements are specified as rigid, or having stiffness much greater than the connecting torus or strap elements. This approach allows the strap response to drive the response of the HIAD. In the real HIAD structure, when the straps experience high load levels they will indent the torus. Depending on the load level of the strap, the indentation can be significant. The effect of indentation could be captured using the link elements and specifying a nonlinear moment curvature relationship. The moment curvature relationship of the link elements would be derived phenomenologically based on the expected indentation response (a function of internal inflation pressure, minor radius, strap width, material response, etc.). This approach is not pursued in the current research as the strap indentation response is not well

117

understood and the 3.7 meter HIAD pressure tub specimen was not loaded to the point where significant strap indentation was observed.

5.3.4 Strap Elements

Strap elements connected the link element ends to each other, to other strap elements, or to the rigid center-body. The response of the straps, like the response of the cords, was tension only, nonlinear at low strain levels, and linear at high strain levels. The strap response, derived from test data produced by NASA researchers (personal communication, July 7, 2016), is shown in Figure 5.9. A small compression stiffness was utilized for numerical stability (18 N).

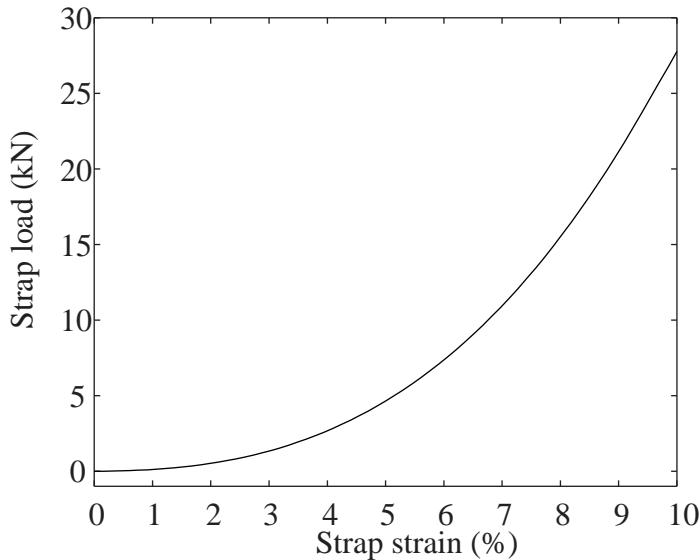Figure 5.9. Axial strap response.

In the real HIAD structure the straps were all pretensioned to some specified load level before the structure was loaded (to target levels of 0.22 to 0.44 kN in the 3.7 meter HIAD structure). As can be seen from Figure 5.9, at the target pretension levels the response of the straps is still quite nonlinear. Two approaches were considered in order to put the

118

beam-based HIAD FE model in the correct prestressed state prior to loading the structure. One method utilizes a pressure equilibrium step with strap prestrains as the model input. The magnitude of the strap prestrains are determined by solving an inverse problem with the objective of obtaining the specified strap prestress, further discussed in Chapter 6.

A simplified method (utilized in the analysis of the 3.7 meter pressure tub tests) assumes the level of strap prestress is known, along with the inflated shape of the structure. The axial strap response (Figure 5.9) is then shifted so that the strap is capable of accommodating a compression load up to the desired level of prestress. In post processing of the results the pretension is added back into the strap load. In the model of the 3.7 meter pressure tub test, the pretension values discussed in Section 5.2 were utilized.

5.3.5 Model Boundaries, Loading and Solution Scheme

A rendering of the beam-based HIAD FE model is shown in Figure 5.10. The cross-sections of the torus members have been rendered so that the model more accurately represents the real HIAD structure visually, although the interaction and link elements are obscured.
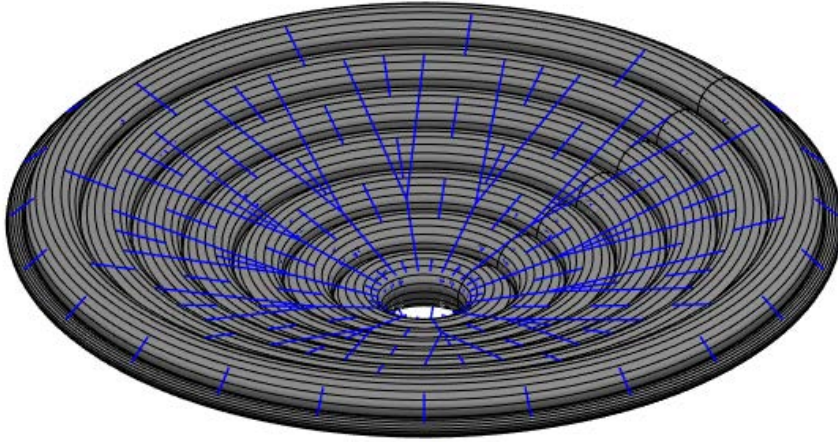
Figure 5.10. Beam-based HIAD FE model.

The HIAD inflatable shell was fixed to the center-body. All T1 interaction elements that return to the center-body were fixed. The loop straps in set 1 (Table 2.1) that wrap around torus T1 were fixed at the center-body, along with the center-body end of the radial straps.

Loading was applied to the torus nodes of the HIAD structure. A uniform pressure (P) was assumed and the tributary width (w_i) of each torus was determined. The tributary width of each torus is essentially the minor diameter of the torus, minus the overlap or compression from adjacent tori (Figure 5.3). The tributary width of each torus was not updated during the analysis. Although the tributary width may change as the structure deforms, it is not expected to have a significant influence on the response of the structure. The uniform pressure that was applied to the tributary width of the torus was integrated to the torus element. The load that is applied to each node is a function of the magnitude of the line load, the major radius of the torus and the number of nodes per torus,

$$F = Pw_i 2\pi \frac{R_i}{N}.$$

Equation 5.18

The vertical reaction of the HIAD structure was recorded during testing. In order to make comparisons to test data, the total uniform pressure load was scaled to match the maximum recorded vertical load (approximately 40 kN). The initial orientation of the nodal forces is aligned perpendicular to the aero-shell surface (at an angle of 20° from vertical). As a pressure load will always remain perpendicular to the surface that the pressure is applied to, non-conservative follower forces were employed so that the forces rotate and translate with the torus nodes (Argyris and Symeonidis 1981). Global load controlled Newton iterations were utilized and adaptive load stepping was implemented in the solution in order to reduce analysis time (Clarke and Hancock 1990).

5.4   Results of Analysis

The beam-based FE model of the 3.7 meter HIAD pressure tub testing was analyzed and compared to test results. The result of greatest interest was the gross load-deformation response of the HIAD. The vertical deflection of torus T7 (the outermost, full-size torus) was tracked throughout the duration of the test using string potentiometers. Figure 5.11 shows the average experimental load-deformation response of the T7 torus with the model comparison.
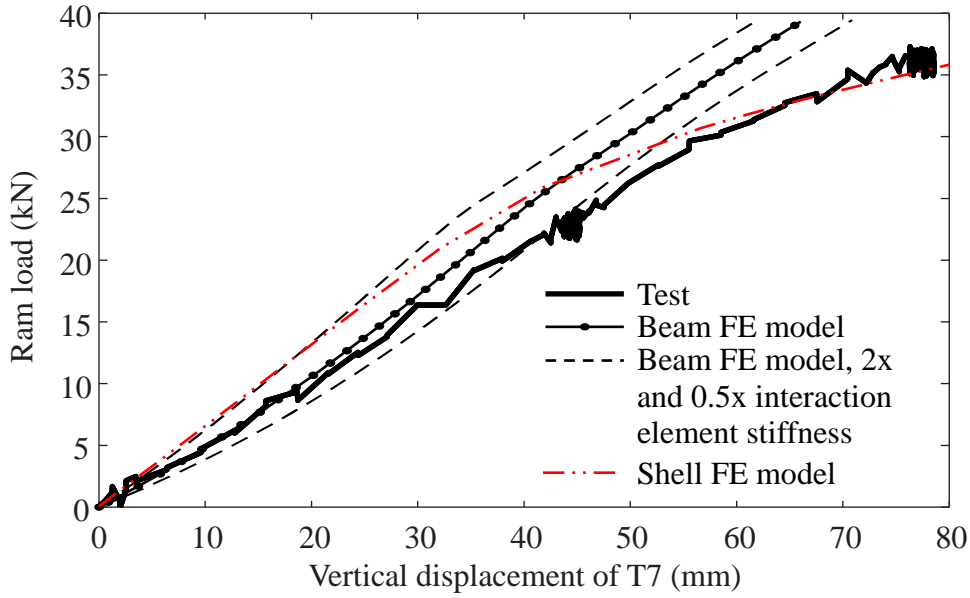
Figure 5.11. Load-deformation response of 3.7 meter HIAD pressure tub test with interaction element stiffness sensitivity.

Two holds in the total load (at approximately 23 and 36 kN) were applied in order to assess the visco-elastic response of the HIAD structure and are visible in the experimental data. As can be seen from Figure 5.11, the beam-based FE modeling response generally follows the gross load-deformation response of the experimental results. The initial stiffness of the model response captures experimental results well and there appears to be an inflection point in both curves at approximately the same load level (at approximately 15 kN). The modeling response is stiffer at higher load levels. A stiffer response is expected to some extent with the lower level modeling methodology employed here.

Shell-based FE modeling results are also provided for the same HIAD configuration and load case for comparison purposes. The shell-based FE modeling results were produced by Michael Lindell, lead structural analyst for the NASA HIAD project (personal

communication, June 6, 2017). The shell-based FE model employed 1/24th wedge symmetry (a 15° slice of the HIAD was modeled), whereas the full HIAD structure was modeled using the beam-based modeling approach. Analysis times on comparable computer systems are approximately one hour versus one minute for the shell versus beam-based modeling approaches respectively. If the full HIAD was modeled using shell elements, this discrepancy would be significantly greater.

Also shown in Figure 5.11 is the response of system when twice and half of the beam-based interaction element stiffness is utilized (Equation 5.2 and Equation 5.8). As can be seen from Figure 5.11, the response is influenced by the interaction stiffness, but even when doubling or halving the stiffness the response is within the same range of the measured response.

The response of the straps was also investigated, a representative subset of which is shown below. Figure 5.12 shows the response of a subset of fore radial straps obtained from test results and the results of modeling efforts.
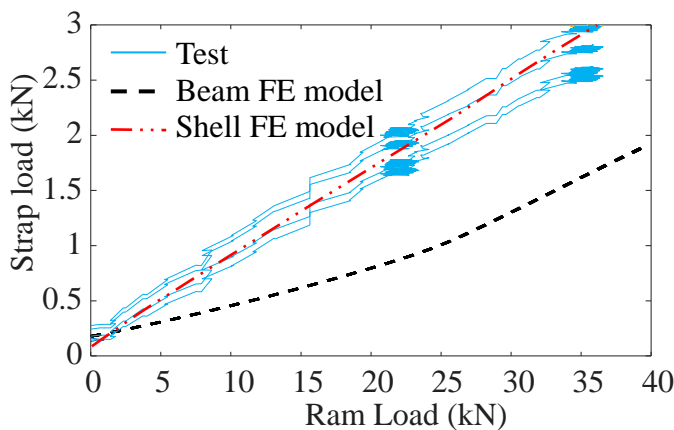

Figure 5.12. Fore radial strap response.

Some variability in the testing results is visible due to specimen and measurement variability. Although the modeling response is on the same order of magnitude as the test results, the beam-based FE modeling response does under-predict the load accommodated by the radial straps. Figure 5.13 and Figure 5.14 presents model comparisons with test data for loop strap sets two and four respectively (see Table 2.1).
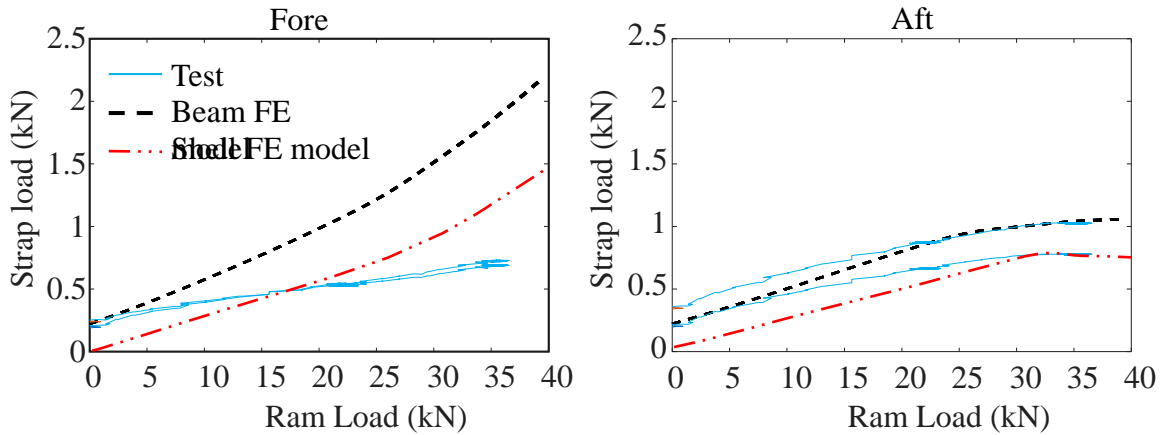

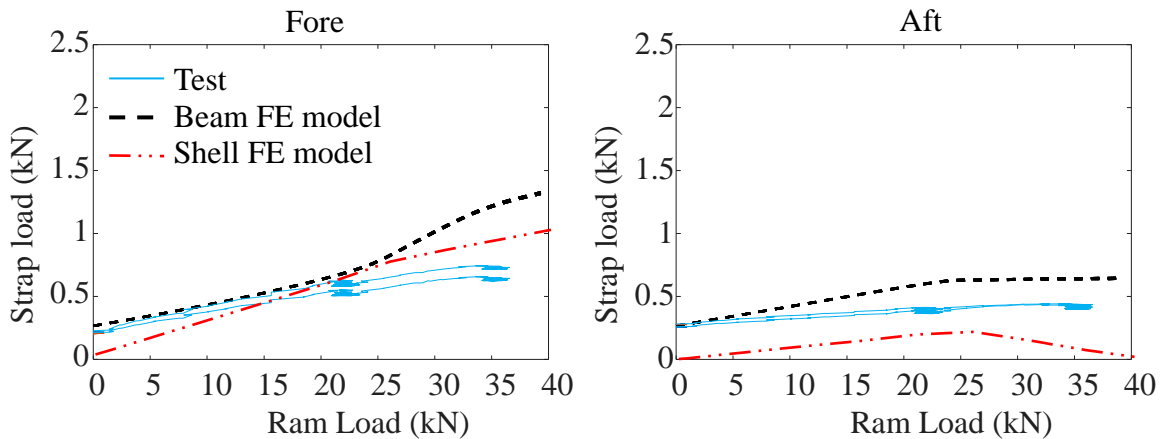Figure 5.13. Loop strap set two fore and aft response.

Figure 5.14. Loop strap set four fore and aft response.

Again, the beam-based FE modeling response is on the same order of magnitude, and shows similar trends to the measured response. The predicted loop strap response tends

to exceed the measured loop strap forces. In general, the load levels predicted by the

modeling response tend to be under-predicted by radial and chevron straps and over-

predicted by loop straps. The shell and beam-based FE modeling results generally follow

similar trends. It is noted that the initial force in the straps is typically under-predicted by

the shell-based modeling efforts. This is illustrative of the fact that the desired initial,

pressurized state is difficult to obtain with the shell-based FE model.

It is hypothesized that the discrepancy between measured strap loads and those predicted

with the beam-based FE model are largely due to real variability in the response of the

straps. The HIAD structure is composed of a multiple tori and strap sets. Many of the

structural components are redundant and the HIAD structure is indeterminate to a high

degree. Modeling efforts can be sensitive to the distribution of stiffness of the members

in highly redundant structures. As can be seen from Figure 5.9, at the levels of strap

pretension that were targeted and measured for 3.7 meter HIAD pressure tub testing, the

strap response is still in the highly nonlinear range. Even at the maximum loads

experienced for the pressure-tub load case (approximately 3 kN) the strap response is still

within the nonlinear range. Even small amounts of variability in the strap response could

make the stiffness significantly off in this range. While the results of the analysis show

that the beam-based FE modeling tools are capable of approximating the response of a

full HIAD system without the use of any tuning or empirically derived parameters, the

strap response should be carefully quantified to ensure the best correlation with test

results. To illustrate the sensitivity of the system to the strap stiffness, two additional

analyses were conducted. In the first analysis all straps had twice the nominal stiffness,

and in the second analysis all straps had half of the nominal stiffness. The results of the
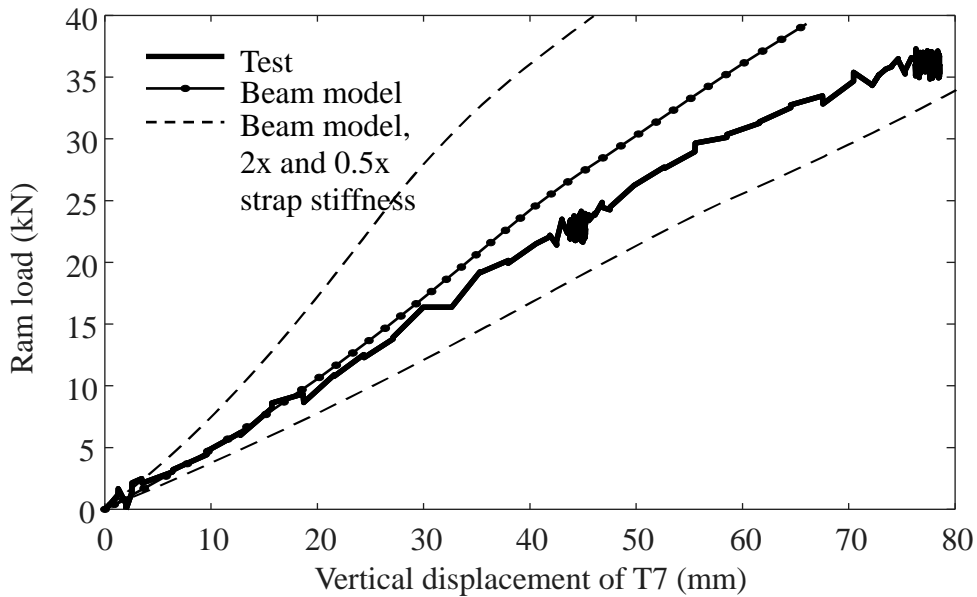analyses can be seen in Figure 5.15.

Figure 5.15. Load-deformation response of 3.7 meter HIAD pressure tub test with strap
stiffness sensitivity.

Successfully applying the beam-based FE modeling methodology that was developed for
use with slender, inflatable members with discrete axial reinforcing cords represents a
significant increase in complexity from previous modeling efforts. Previous model
validation efforts considered single straight or curved members, while modeling the full
HIAD system required accounting for the interaction and connections between tori. With
confidence that the beam-based FE modeling approach can reasonably capture the
response of a full HIAD system, the analysis methodology is extended to model full-scale
HIAD articles in Chapter 6.

Chapter 6

FULL-SCALE HIAD ANALYSES

Following validation of the beam based FE modeling approach to experimental results of

straight tube, torus and full HIAD structures in Chapter 4 and Chapter 5, the modeling

tools were extended to the analysis of larger scale and more complex HIAD structures.

In this chapter models of two HIAD structures are developed and analyzed. First, a 16.7

meter major diameter HIAD model for reentry on Mars was created. Strap pretension

and load-deformation analyses with loading derived from computational fluid dynamics

(CFD) analyses were conducted. The response of the structure with an aerodynamic tab

for the purpose of controlling the orientation of the HIAD during atmospheric reentry

was also investigated. In addition to the 16.7 meter HIAD structure, a 6 meter major

diameter HIAD model for Earth reentry was created. The 6 meter model was utilized to

couple the structural analysis tools that have been developed as part of this research with

structural optimization tools. The coupling of analysis and optimization routines allows

for the response drivers of the system to be explored and the response of the system to be

better understood. A description of the HIAD 6 meter model and analyses are provided.

6.1   Strap Prestress Analysis

In this section strategies for including the effect of strap prestress were investigated.

While in Chapter 5 a simplified approach was utilized to incorporate strap prestress, a

more rigorous approach was taken here.

6.1.1   Problem Description and Motivation

The HIAD structure is composed of a series of concentric tori that are stacked together to

form a cone shape (see Figure 1.1). The individual tori are strapped together and

strapped to the relatively rigid center-body. During the initial construction process the individual straps are pretensioned to a desired load level (generally on the order of 0.2 to 0.9 kN) to obtain a target shape. As the structure is loaded during atmospheric reentry some of the straps will experience an increase in tension while other straps will experience a decrease in tension. Once the straps that experience a decrease in tension are completely unloaded they will become slack and lose all stiffness. The level of strap pretension therefore has the potential to significantly influence the structural response of the HIAD system.

In addition to strap pretension levels, the strap pretension process has the potential to influence the initial shape of the HIAD structure. As individual straps are pretensioned the HIAD may deform, potentially loading or unloading other straps in the system in unexpected ways. An initial shape of the HIAD system that has been modified by the pretensioning process could further influence the load-deformation response.

In the previous analysis of the 3.7 meter HIAD test article a simplified approach was taken in order to incorporate strap prestress. The initial, pretensioned shape of the HIAD structure was assumed to be known, along with the level of strap pretension in each strap set. The load-strain response of the individual straps (Figure 5.9) was then shifted so they could accommodate a level of compression equal to the level of expected pretension. In the post-processing stage the initial strap pretension was simply added back into the element axial force.

The benefit of utilizing the simplified prestress approach is an initial, prestress equilibrium step was not needed. However, it was unknown as to whether or not the simplified approach significantly influenced the response of the HIAD modeling results.

In order to more accurately incorporate the initial, prestressed HIAD configuration, an initial equilibrium step must be utilized. The level of strap prestrain must be defined such that the desired level of strap prestress is obtained. The challenge with this approach is the HIAD structure is indeterminate to a high degree and small changes is the initial level of prestrain in one strap set can have an influence on the final strap prestress in all other strap sets, and an influence on the HIAD initial shape. In order to find the levels of strap prestrain that produce the correct amount of pretension, and maintain the desired HIAD shape, an inverse problem must be solved.

6.1.2 Description of Model, Boundaries and Loading

Before continuing with the development of the strap prestress analysis, a description of the HIAD model that was utilized in the development of the strap prestress equilibrium methodology is warranted. The 16.7 meter HIAD model was developed and analyzed prior to the development of the 3.7 meter HIAD model detailed in Chapter 5, and the development of the 6 meter article described later in this chapter. As such the cord and strap material inputs are not as refined as in other analyses, but they do approximate the material response adequately. The HIAD structure was composed of six tori, as shown in Figure 6.1. The outer, shoulder torus creates a 16.7 meter major diameter structure and the center-body major diameter was 4.3 meters. All naming, sign and coordinate system conventions remain consistent with previous analyses (Chapter 5).
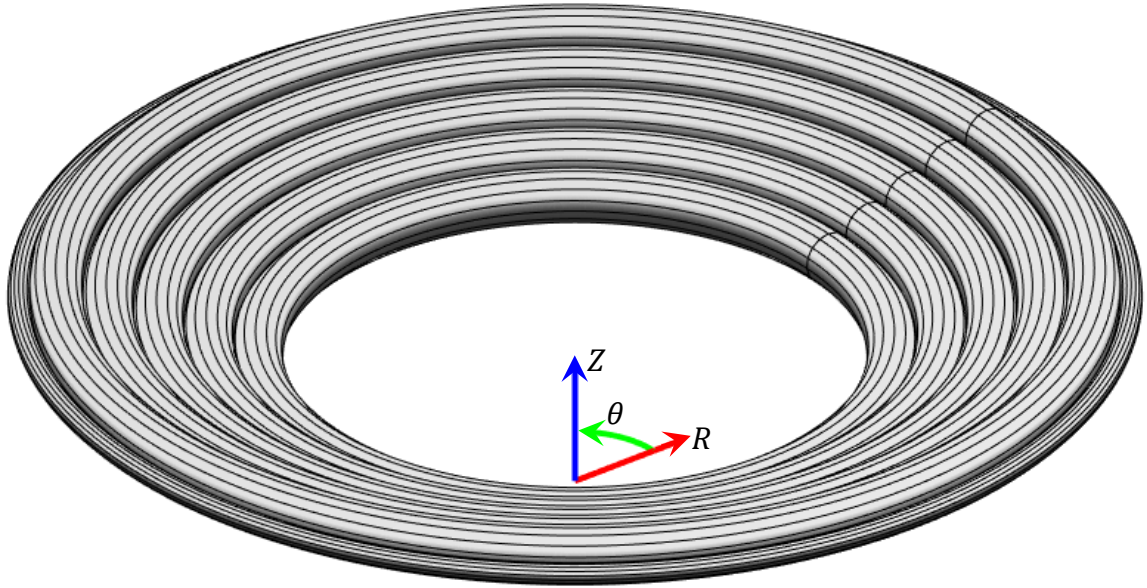
Figure 6.1. 16.7 meter major diameter HIAD, configuration of tori.

The tori created a 20° angle from the horizontal, R axis. The configurations of the HIAD

tori are specified in Table 6.1.

Table 6.1. Configuration of tori, 16.7 meter HIAD configuration.

Torus	R location (mm)	Z location (mm)	Minor diameter (mm)	Inflation pressure (kPa)
T1	4704	2142	809	138
T2	5429	2406	809	138
T3	6161	2673	809	138
T4	6900	2942	809	138
T5	7645	3213	809	138
T6	8189	3153	323	138

All tori had two axial reinforcing cords located at ±60° from the inner equatorial axis of

the torus. The cord force-strain relationship (shown in Figure 6.2) was based on the

response of a Zylon cord. The stiffness of the cord was doubled because it was assumed two cords would be needed to accommodate the significantly increased cord force due to the larger section diameter of the tori. The cord load at inflation pressure was calculated to be 27 kN for tori T1 through T5 and 4.3 kN for torus T6 (Equation 2.17).
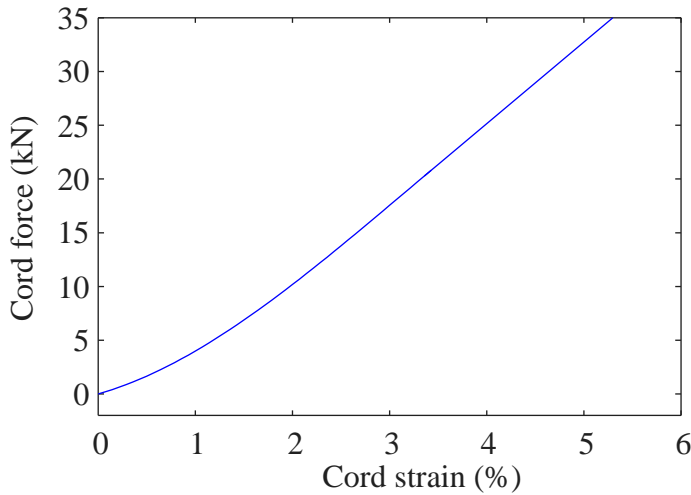

Figure 6.2. Idealized load versus strain response of cords.

The extensional and shear stiffness of the Zylon braided shell were utilized as model inputs (15.7 and 700 N/mm, respectively). The additional longitudinal stiffness due to the geometric changes that the braided shell undergoes when subjected to an axial strain was also included as described in Chapter 2, Section 2.2.1.2 (Equation 2.30, the gross extensional modulus was 35.6 N/mm for tori T1 through T5 and 23.7 N/mm for the shoulder torus, T6).

As with the 3.7 meter major diameter HIAD discussed in Chapter 5, strap sets included loop straps, radial straps and chevron straps. Table 6.2 details the configurations of each strap set. Radial straps connected from the HIAD center-body (CB) to the base of the chevron (chev.) straps between the T2 and T3 tori.

Table 6.2. Strap set configurations.

Strap set	Strap type	Number of straps	Location of first strap (deg.)	Connection	Swept θ (deg.)	Target preload (kN)
1	Loop-aft	148	0	CB to T1	0	0.2224
2	Loop-aft	148	0	T2 to T3	0	0.2224
3	Loop-aft	148	0	T4 to T5	0	0.2224
4	Loop-fore	148	0	CB to T1	0	0.2224
5	Loop-fore	148	0	T2 to T3	0	0.2224
6	Loop-fore	148	0	T4 to T5	0	0.2224
7	Loop-aft	148	1.22	T1 to T2	0	0.2224
8	Loop-aft	148	1.22	T3 to T4	0	0.2224
9	Loop-aft	148	1.22	T5 to T6	0	0.2224
10	Loop-fore	148	1.22	T1 to T2	0	0.2224
11	Loop-fore	148	1.22	T3 to T4	0	0.2224
12	Loop-fore	148	1.22	T5 to T6	0	0.2224
13	Radial-aft	148	1.22	CB to Chev.	0	0.4448
14	Chev.-aft	296	1.22	Radial to T5	±0.61	0.2224
15	Radial-fore	148	0	CB to Chev.	0	0.4448
16	Chev.-fore	296	0	Radial to T5	±0.61	0.2224

The 16.7 meter HIAD model and straps are illustrated in Figure 6.3. A plan view of the

aft side of the HIAD is visible ($+Z$ is out of the page). Only 24 strap sets are shown in

Figure 6.3 (rather than the 148 strap sets that were used in the analyses), so that

individual straps are discernable.
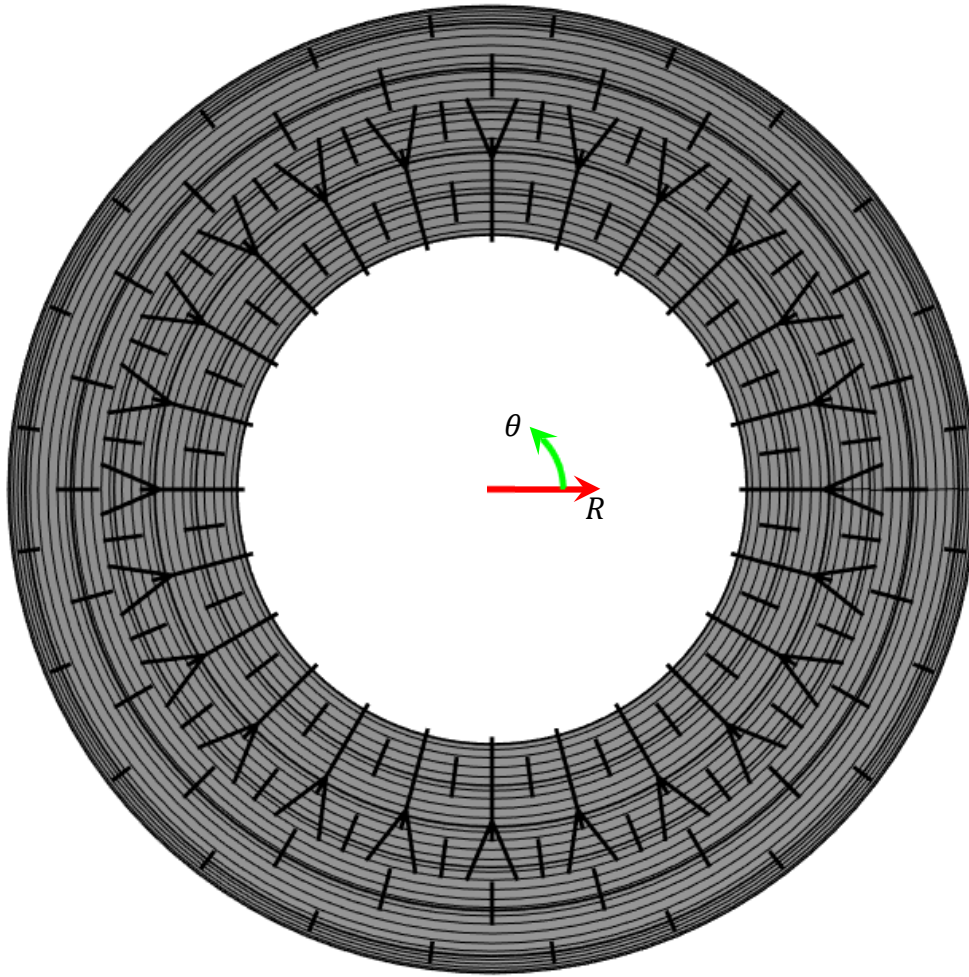
Figure 6.3. 16.7 meter HIAD model with straps (only 24 strap sets shown).

The force-strain response of the loop and radial strap sets are shown in Figure 6.4. A

small compression stiffness was utilized for numerical stability (18 N). To avoid

numerical issues that were encountered in the development of the 16.7 meter HIAD

model, the chevron strap's response was taken as linear (507 kN) with an axial rigidity

equal to the axial rigidity of the loop straps in the linear range (above 1 kN of load in

Figure 6.4). Because the radial and chevron straps are in series, the chevron straps were

not capable of accommodating load after the radial straps loose pretension, even though

the constitutive relationship of the chevron straps allowed compression.
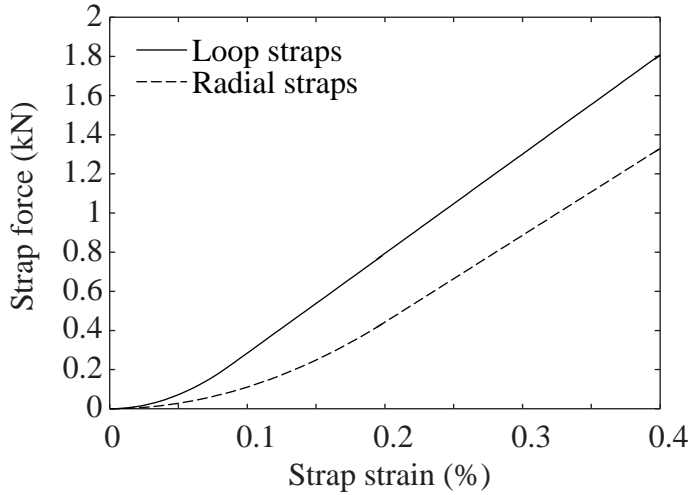
Figure 6.4. Loop and radial strap force-strain response.

A force offset was not included in the strap response, as had been done for previous

analyses using the simplified prestress approach. A strap prestrain input was

incorporated for each strap set. A positive prestrain induced a contraction of the member.

If both ends of a strap element were fixed a tension force would develop following the

response shown in Figure 6.4.

Even with no initial strap prestrain, the HIAD is not in a state of static equilibrium

because there is some amount of torus overlap, causing the tori to react or compress

against each other. To account for this initial pre-compression the interaction elements

were prestrained by an amount equal to the overlap between two adjacent tori. The

distance L_i between two tori centers was,

$$L_i = [(R_{i+1} - R_i)^2 + (Z_{i+1} - Z_i)^2]^{1/2}.$$

Equation 6.1

The radial (R) and vertical (Z) location of the torus centers can be found in Table 6.1.

The change in length between the two tori was,

$$\Delta L_i = L_i - 0.5(d_{i+1} + d_i). \hspace{4cm} \text{Equation 6.2}$$

The minor diameters of the tori (d) are also found in Table 6.1. Equation 6.1 and

Equation 6.2 can then be combined to determine the amount of interaction prestrain,

$$\varepsilon_i = \frac{\Delta L_i}{L_i}. \hspace{5cm} \text{Equation 6.3}$$

Because the prestrain was negative for all adjacent tori, the interaction elements always

elongated and began the analysis in a pre-compressed state. For the case of the first

interaction element set (between the center-body and T1), d_i was simply taken as zero.

When an arbitrary set of strap and interaction element prestrains are defined and used as

model inputs, the HIAD configuration was not in a state of static equilibrium, even

though no external loading was applied. All of the internal forces must be allowed to

come to an equilibrium configuration. The amount of force that was developed in each

strap set cannot be predicted *a priori* because the structure was nonlinear and highly

redundant. Newton iterations were used to ensure that the final configuration of the

prestrained HIAD structure was in an equilibrium configuration. Although there may be

more efficient form finding solution techniques available, such as the force density or

dynamic relaxation methods (Adriaenssens et al. 2014), utilizing Newton iterations was

found to be sufficient for the current application.

6.1.3   Analysis, Results and Significance

As was discussed previously, the goal of the analysis was to determine the correct level

of prestrain in each strap set, such that the desired level of strap prestress was achieved

(Table 6.2) and the desired shape of the structure was maintained. An objective function was developed that incorporated the strap force objectives, along with the HIAD shape requirements as a soft constraint.

The strap force portion of the objective function simply found the difference between the desired strap pretension (Table 6.2) and the strap tension after the convergence of the prestrain equilibrium step (f_0 and f, respectively). The vector of 14 force discrepancies (the chevron straps, sets 14 and 16 in Table 6.2, are not included in the objective function because they are in series with the radial straps and a function of the radial strap force) are then individually squared and summed together to obtain a scalar objective value. The shape portion of the objective function sums the squared difference of the individual torus centers after the convergence of the equilibrium step from a line that passes through the torus centers in the desired configuration (a vector of torus location errors, e), as illustrated in Figure 6.5. The shape objective was then added to the strap force objective to obtain a single, scalar objective value.
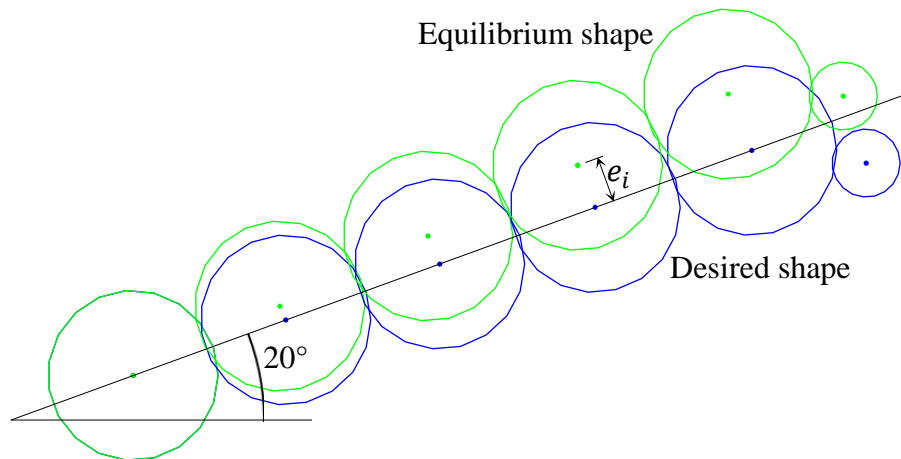
Figure 6.5. Desired and equilibrium HIAD cross-section.

The input variables included the 16 strap prestrains and an initial cone angle adjustment. It was found that as the system approached the correct, prestressed state, the entire HIAD tended to pitch forward, making an angle less than 20° with the horizontal axis. The cone angle adjustment modified the initial location of the torus centers to allow the HIAD to pitch to the correct final angle. The torus centers were rotated as a rigid body about the T1 torus center by the magnitude of the cone adjustment angle. For example a cone adjustment angle of -10° would produce an initial HIAD configuration with tori oriented at an angle of 30° from the horizontal axis (instead of the 20° shown in Figure 6.5). The formulation of the unconstrained optimization problem was,

$$find\ \boldsymbol{X} \hspace{4cm} \text{Equation 6.4}$$

$$such\ that\ \sum_{i=1}^{14} (\boldsymbol{f}_{0i} - \boldsymbol{f}_i)^2 + \sum_{j=1}^{6} \boldsymbol{e}_j{}^2\ is\ minimized.$$

The vector $\boldsymbol{X}$ includes the 16 strap set prestrains and cone adjustment angle.

The optimization problem was solved using the built in MATLAB (2015) function *fmincon* with the interior-point algorithm. The converged solution produced results that were well within an acceptable tolerance and are detailed in Table 6.3. The converged cone adjustment angle was -5.32°.

Table 6.3. Strap prestrain and prestress results.

Strap set	Prestrain	Target prestress (kN)	Equilibrium prestress (kN)
1	-0.0414	0.2224	0.2235
2	0.0439	0.2224	0.2209
3	0.00756	0.2224	0.2234
4	0.0508	0.2224	0.2211
5	0.0504	0.2224	0.2231
6	-0.0196	0.2224	0.2238
7	0.0212	0.2224	0.2213
8	0.0948	0.2224	0.2214
9	0.0650	0.2224	0.2225
10	0.0592	0.2224	0.2213
11	0.0807	0.2224	0.2243
12	0.0580	0.2224	0.2224
13	0.000410	0.4448	0.4423
14	0.0891	--	0.2217
15	0.0129	0.4448	0.4450
16	0.124	--	0.2231

The final strap pretension was less than 1% of the target pretension in all cases. Figure 6.6 illustrates the desired, initial (with cone adjustment angle), and final (equilibrium) configurations of the HIAD cross-section. As can be seen from Figure 6.6, the HIAD

pitches forward and compresses during the strap equilibrium step to achieve the desired cone angle.
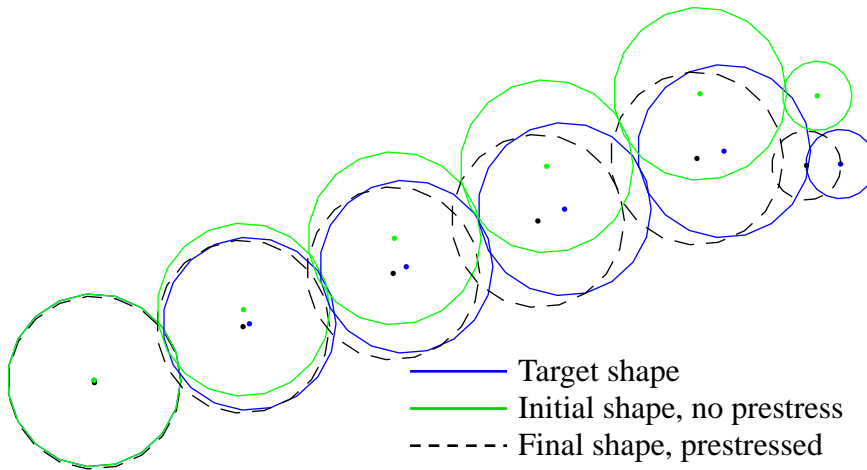
Figure 6.6. Desired, initial and equilibrium HIAD cross-section configurations.

The strap prestress finding methodology that was developed here could be applied to the analysis of higher fidelity, shell-based FE models with wedge symmetry applied, although more efficient solution techniques would be worth investigating. Alternately, the beam-based FE model could potentially be used to determine strap prestrain inputs to the shell-based model, although care would be required to ensure that all of the material and geometric inputs were closely matched between model types.

Although the strap prestress finding methodology showed that the beam-based FE model is capable of achieving the correct prestressed state with an equilibrium step, whether or not the simplified strap prestress approach can produce adequate results was still an outstanding question. The advantage to using the simplified approach is that neither the prestress finding process, nor is an initial equilibrium is step needed. To assess the efficacy of the two approaches to handling strap prestress, three analyses were conducted

using a uniform pressure load on the fore side of the HIAD structure. The configurations that were analyzed included:

1. The prestressed model that utilized the prestrains obtained in the optimization process and an equilibrium step,

2. A model that utilized the shape obtained in the optimization process with the simplified prestress methodology, and

3. A nominal model that utilized the target HIAD shape and the simplified prestress methodology.

The load deformation results (total vertical reaction versus vertical deflection of the T5 torus) are shown in Figure 6.7, below.

—— Prestressed analysis
--- Simplified prestressed analysis, prestressed geometry
—•— Simplified prestressed analysis, original geometry
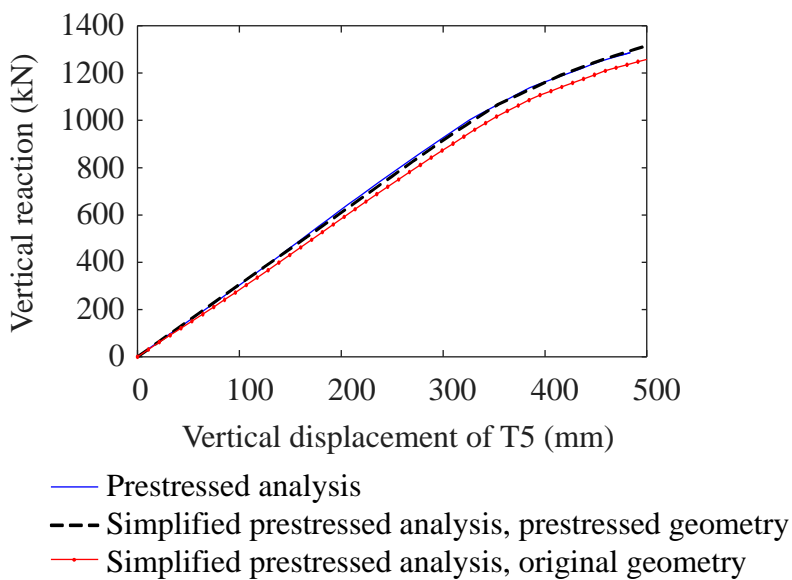
Figure 6.7. Uniform pressure analysis on prestressed and simplified prestressed HIAD configurations.

As can be seen from Figure 6.7, the prestressed analysis and non-prestressed analysis with prestressed geometry match well. Even the nominal model that utilizes the

simplified approach and original geometry tracks the refined solutions reasonably well, with a final predicted load within 4% of the refined solution.

The methodology that was developed for finding the initial, prestressed HIAD configuration is of use when conducting more refined analyses, or investigating a particular HIAD configuration. However, for the purposes of obtaining the gross response of a HIAD structure, analyzing multiple configurations, or when in the design process where variables that influence the prestressed configuration may be parameterized, the simplified methodology is adequate and offers a significant amount of time savings.

In addition to strap pretension levels, the variability in strap pretension (which was significant for the 3.7 meter HIAD structure investigated in Chapter 5), also has the potential to influence response. The impact of strap variability could be investigated using optimized strap prestrains as the reference configuration and varying the prestrains within a strap set based on some expected distribution. This study is outside of the scope of the current work and was not investigated here.

6.2   Full-Scale HIAD Tab Study

In this section analyses on the 16.7 meter HIAD configuration are continued. The model is extended to investigate alternative pressure loading distributions and the influence of an aerodynamic tab on the structural response.

6.2.1   Problem Description and Motivation

In addition to utilizing the 16.7 meter major diameter HIAD model for the purpose of developing a strap pretension methodology, the configuration was also used for the study

of a non-axisymmetric HIAD. As the HIAD travels through the atmosphere it is desirable to be able to control the orientation of the body's lift and drag vectors in order to more accurately control the flight of the system. There are multiple concepts for creating the non-axisymmetric shapes that would allow more desirable lift to drag ratios than those produced by the typical stacked cones that have been described previously. Concepts include controlling the payload center of mass, a canted stacked torus configuration that produces a more ovalized cone, morphing HIAD concepts where the shape of the relatively compliant structure is actively changed during reentry using cables and actuators, and the use of aerodynamic tabs, to name a few (Johnson 2016).

An important question with all of the non-axisymmetric configurations is how the change in external pressure loading that is induced by the asymmetry influences the structural response. In the current study, a tab configuration was investigated. The tabbed HIAD consisted of the 16.7 meter structure with an additional tab cantilevered from the T5 torus. The tab was pitched to match the cone angle of the HIAD structure (20° from the horizontal axis), as shown in Figure 6.8.
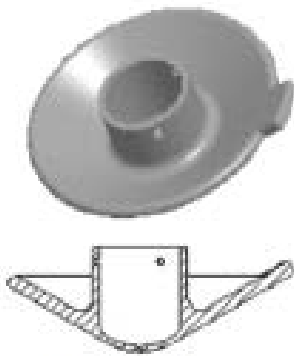
Figure 6.8. Rendering and cross-section of HIAD structure with tab (Johnson et al. 2016).

6.2.2 Analysis and Results

The tab size was chosen to be 3% of the total frontal, projected area of the HIAD. The length of the tab is approximately 1.9 meters and has a swept area of 25°. To obtain the expected pressure distribution on the fore side of the HIAD surface, CFD analyses were conducted by NASA researchers (personal communication, February 24, 2016). The pressure distribution is shown in Figure 6.9. Also shown in Figure 6.9 are the global coordinate system, and the location of the leeward and windward sides of the HIAD.
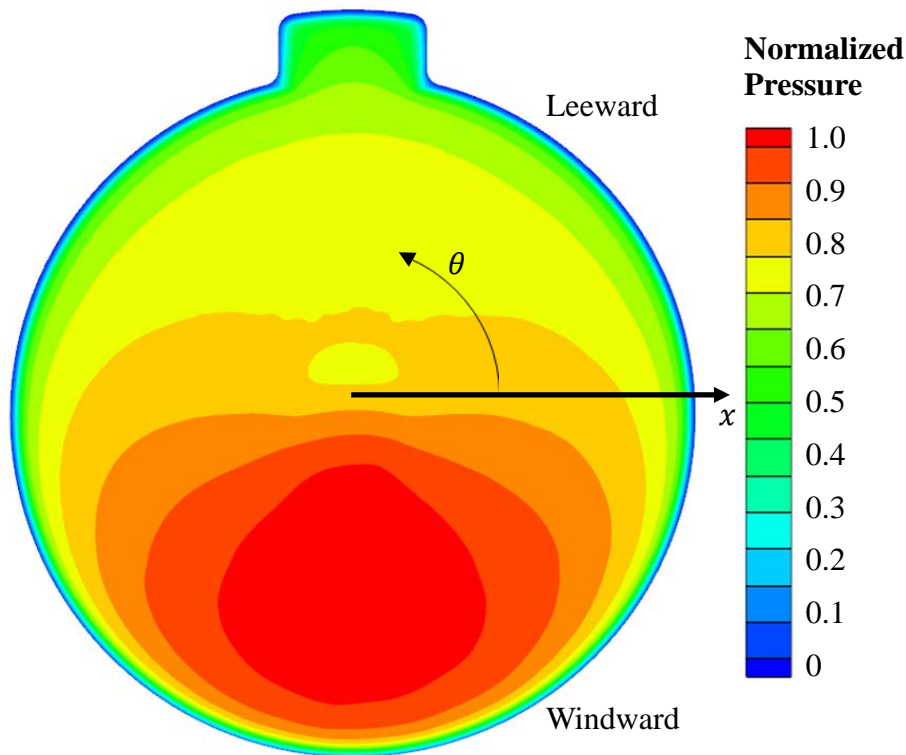
Figure 6.9. Tabbed 16.7 meter HIAD expected pressure distribution.

Two analyses were developed to assess the influence of the tab on the structural response of the HIAD system. In the first analysis the pressure distribution shown in Figure 6.9 was interpolated to the tori but the tab structure and tab loading were not included. In the second analysis the tab structure was approximated using beam finite elements and the

143

pressure loading from Figure 6.9 was interpolated to both the tori and the tab structure. To model the tab structure, rigid beam elements were cantilevered from the T5 torus. The pressure distribution of the tab was then integrated to point loads located at the cantilever tips. A total of 35 tab elements were utilized (one per torus node in the tab region). The tab structure is shown on a 60° wedge of the HIAD in Figure 6.10. The torus cross-sections have been rendered and the strap elements are not shown for clarity. By modeling the tab in this manner, no assumptions were made as to how an actual tab would be designed or connected to the HIAD structure, except that it would be cantilevered from the last full-sized torus (a worst-case scenario). The tab elements imparted the correct thrust and torque to the torus elements while not over-constraining the torsional rigidity of the inflatable member. The simplified strap pretensioning methodology was utilized in both analyses.
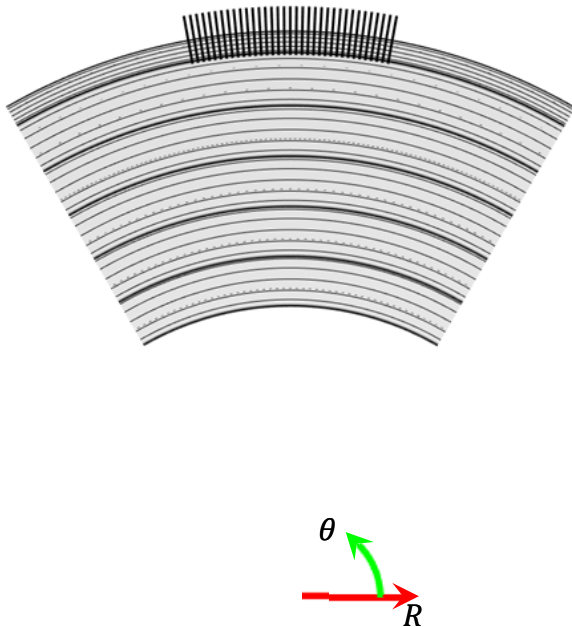
Figure 6.10. Tab structure.

The normalized pressure distribution shown in Figure 6.9 was scaled so that the total

integrated vertical force on the aeroshell portion of the HIAD was almost 1,200 kN, a

load level that is expected to be above the operational load level during reentry. The load

deformation response of the two HIAD structures (vertical reaction versus vertical

displacement of the T5 torus), is shown in Figure 6.11.
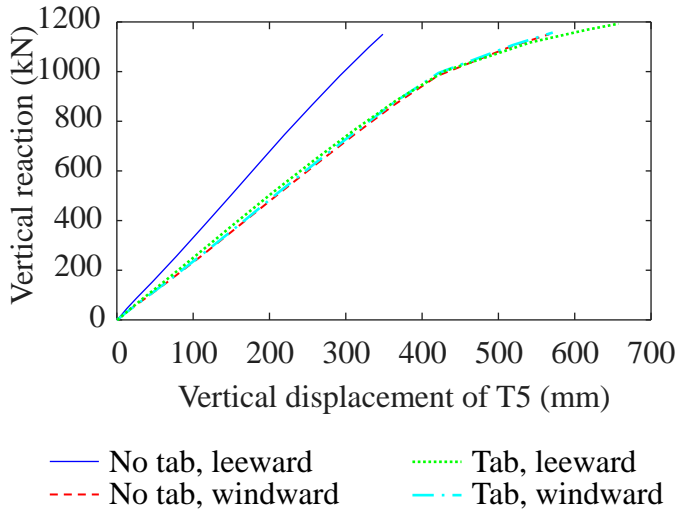
Figure 6.11. Load deformation response of HIAD with and without a tab.

As can be seen from Figure 6.11 the response of the HIAD remains essentially constant

on the windward side of the HIAD with and without the presence of the tab. The

response of the structure on the leeward, tabbed, side of the HIAD is significantly

influenced by the presence of the tab. Although the response of the leeward side of the

tabbed HIAD softens at higher load levels (above 1,000 kN of vertical reaction), the

structure is still capable of accommodating load. The deformed shape of the un-tabbed

and tabbed HIAD at the maximum load is shown in Figure 6.12, viewed from the leeward

side. The tab structure is shown in the bottom HIAD configuration and the color mapped

total deformation is also provided. The straps are not shown in Figure 6.12 so that the

deformations of the tori are more clearly visible.
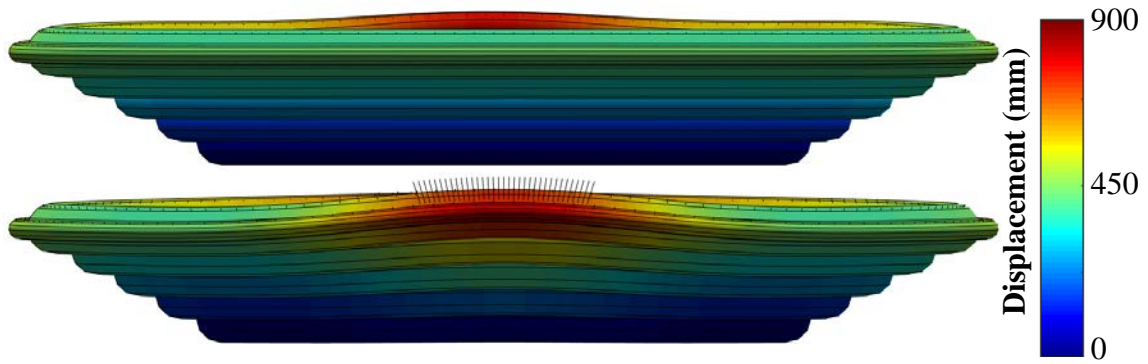
Figure 6.12. Deformed shape of un-tabbed (top) and tabbed (bottom) HIAD.

As can be seen from Figure 6.12, the deformation due to the tab is fairly localized to the area surrounding the tab structure. As the tab structure was loaded the additional force and torque was accommodated by the strap system and the torsional rigidity of the T5 torus. The final magnitude of the maximum shear strain in torus T5 was estimated to be 0.24% without the tab structure and 0.50% with the tab structure. The maximum shear strain reported in Clapp et al. (2016a) was approximately 0.3%. Although the estimated shear strain for the tabbed structure is 67% greater than the values reported in Clapp et al. (2016a), the member is expected to be capable of accommodating the greater shear strain without wrinkling because it is continuously braced by adjacent tori.

Figure 6.13 illustrates the response of the radial straps on the fore side of the HIAD structure with and without the presence of a tab. With a uniform pressure loading all radial straps would be expected to load equally. As can be seen from Figure 6.13, there is some spread in the radial strap loads around the HIAD structure as the system without a tab is loaded by the non-axisymmetric pressure distribution; however, the magnitude of

discrepancy between straps increases significantly for the tabbed structure. The more

highly loaded straps are in the immediate vicinity of the tab structure.
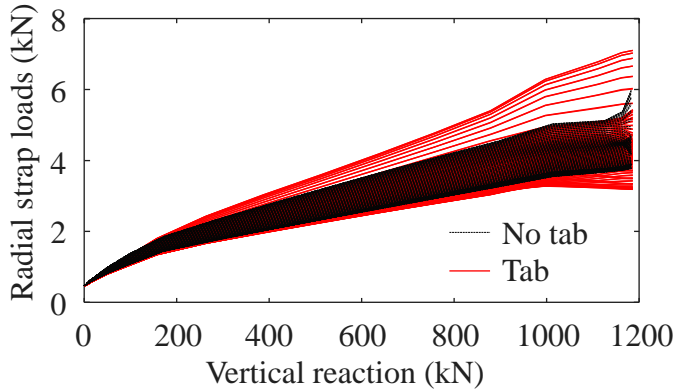
Figure 6.13. Radial strap loads.

The beam-based modeling methodology is a powerful tool for exploring various HIAD

configurations, including non-axisymmetric designs. The previous analysis demonstrates

the feasibility of analyzing large-scale and non-standard HIAD configurations, and how a

non-uniform pressure distribution can be applied to the model.

6.3   HIAD Structural Optimization

An efficient HIAD structural modeling tool has been developed and validated at the

component and structural levels. Although it has been demonstrated that the modeling

tools can be used for the analysis of the HIAD system, there are still outstanding

questions as to what parameters drive the structural response. The influences of internal

pressure distribution, torus braid angles, strap placement, cord placement, component

stiffness, etc. are still being understood. In the following sections the HIAD modeling

and analysis tools are coupled to optimization routines in order to demonstrate how some

of these questions may be answered, and how the HIAD design process may be

automated. A genetic algorithm (GA) is employed to demonstrate the methodology

because of its ease of implementation and robust nature. Although at the current stage of

the development process the structural configuration is not being optimized, coupling the

analysis to optimization routines can still be a powerful tool for understanding the

response of the system and developing analysis methodologies.

6.3.1   HIAD Model Description

Before continuing with a description of the optimization studies that were conducted, a

description of the HIAD article that was utilized is warranted. The HIAD configuration

that was utilized in the development of optimization studies was based on a 6 meter

configuration designed for reentry in Earth's atmosphere. The system consisted of seven

tori (six full sized tori and one shoulder torus). The nominal inflation pressure was 69

kPa for each torus. Figure 6.14 illustrates the configuration of the tori.
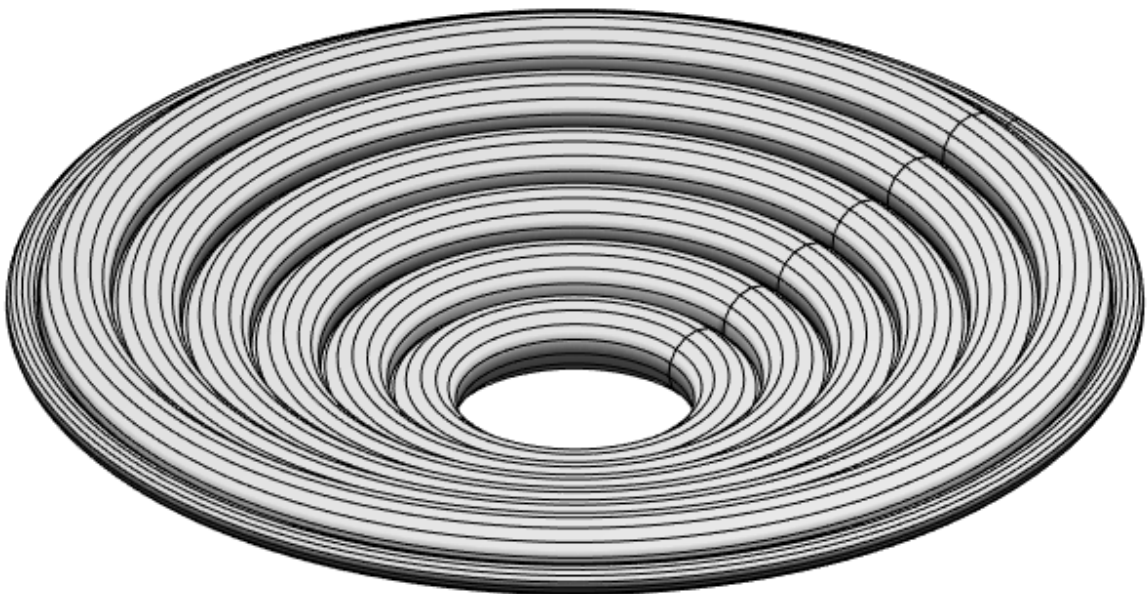
Figure 6.14. 6 meter major diameter HIAD, configuration of tori.

The diameter of the center-body was 1.24 meters and the tori created a 20° angle from the horizontal, R axis (coordinate systems are consistent with previous HIAD analyses). The configurations of the HIAD tori are specified in Table 6.1.

Table 6.4. Configuration of tori, 6 meter HIAD configuration.

Torus	R location (mm)	Z location (mm)	Minor diameter (mm)	Nominal inflation pressure (kPa)
T1	808	450	386	69
T2	1167	630	387	69
T3	1528	762	389	69
T4	1891	894	390	69
T5	2256	1027	391	69
T6	2622	1160	392	69
T7	2899	1145	168	69

All tori had two axial reinforcing cords located at ±60° from the inner equatorial axis of the torus. The cord force-strain relationship is based on a Zylon cord and is shown in Figure 5.4. The cord load at the nominal inflation pressure ranged from 3.08 to 3.18 kN for tori T1 through T6 and was 0.56 kN for torus T7 (Equation 2.17).

The extensional and shear stiffness of the Zylon braided shell used in this study were based on test data at 83 kPa of inflation pressure (the extensional and shear moduli were 15.7 and 700 N/mm respectively). The Zylon braid used in this study was only tested at a 71° braid angle and 83 kPa of inflation pressure using the tension/torsion methodology described in Clapp et al. (2016a). The extensional stiffness is assumed to be constant

across all braid angles and inflation pressures and the additional longitudinal stiffness due to the geometric changes that the braided shell undergoes when subjected to an axial strain was included in the typical manner. However, the shear stiffness is expected to vary with inflation pressure and braid angle. To estimate the shear stiffness for configurations other than a 71° braid angle and 83 kPa of inflation pressure, the results of testing with a Technora braid (reported in Clapp et al. 2016a) were scaled to the single Zylon data point that was available. The scaled data that was used to interpolate the shear stiffness of the braided material as a function of inflation pressure and braid angle is shown in Table 6.5, below.

Table 6.5. Zylon shear stiffness interpolation table (N/mm).

		Braid angle (deg.)			
		55	**60**	**65**	**71**
	3.4	351	202	186	128
Inflation pressure (kPa)	**34**	2550	1069	707	436
	69	3552	1501	1156	622
	103	3891	1814	1477	818
	138	4096	2119	1684	911

As with the 3.7 meter major diameter HIAD discussed in Chapter 5 and the 16.7 meter HIAD discussed earlier in this chapter, strap sets included loop straps, radial straps and chevron straps. Table 6.6 details the configurations of each strap set. Radial straps connected from the HIAD center-body (CB) to the base of the chevron (chev.) straps between the T2 and T3 tori.

Table 6.6. Strap set configurations for 6 meter HIAD.

Strap set	Strap type	Number of straps	Location of first strap (deg.)	Connection	Swept θ (deg.)	Preload (kN)
1	Loop-aft	32	0	CB to T1	0	0.4448
2	Loop-aft	32	0	T2 to T3	0	0.4448
3	Loop-aft	32	0	T4 to T5	0	0.4448
4	Loop-aft	32	0	T6 to T7	0	0.4448
5	Loop-fore	32	0	CB to T1	0	0.4448
6	Loop-fore	32	0	T2 to T3	0	0.4448
7	Loop-fore	32	0	T4 to T5	0	0.4448
8	Loop-fore	32	0	T6 to T7	0	0.4448
9	Loop-aft	32	5.625	T1 to T2	0	0.4448
10	Loop-aft	32	5.625	T3 to T4	0	0.4448
11	Loop-aft	32	5.625	T5 to T6	0	0.4448
12	Loop-fore	32	5.625	T1 to T2	0	0.4448
13	Loop-fore	32	5.625	T3 to T4	0	0.4448
14	Loop-fore	32	5.625	T5 to T6	0	0.4448
15	Radial-aft	32	5.625	CB to Chev.	0	0.890
16	Chev.-aft	64	5.625	Radial to T5	±2.8	0.4448
17	Radial-fore	32	0	CB to Chev.	0	0.890
18	Chev.-fore	64	0	Radial to T5	±2.8	0.4448

The strap force-strain response was derived from test data produced by NASA researchers and is shown in Figure 6.15 (personal communication, September 7, 2016). A small compression stiffness was utilized for numerical stability (18 N). The simplified strap pretensioning method was used in all 6 meter HIAD analyses.
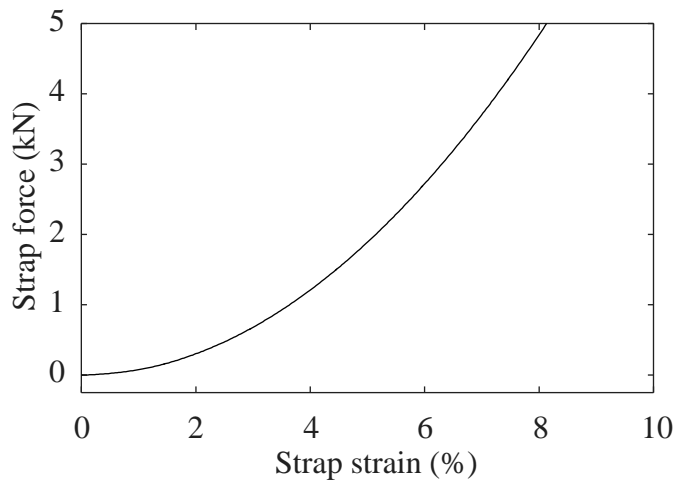
Figure 6.15. Strap force-strain response.

A uniform pressure load was applied to the tori. The load-deformation response of the nominal HIAD configuration is shown in Figure 6.16. The total vertical reaction is shown versus the vertical displacement of the T6 torus. The operational load level is expected to be at approximately 130 kN of total vertical reaction. The initial, tangent stiffness of the structure was 555 N/mm.
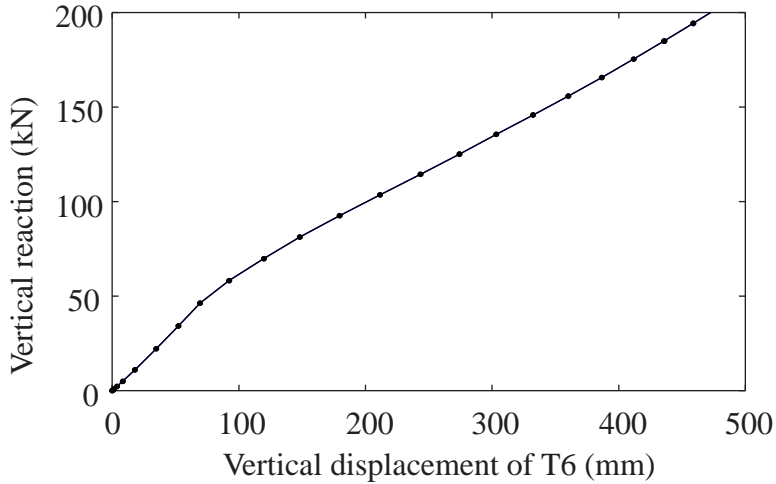
Figure 6.16. Load-deformation response of 6 meter HIAD configuration with uniform pressure load.

6.3.2 HIAD Optimization

Any HIAD optimization study will necessarily include a subset of HIAD design parameters, objective functions and constraint functions. Before conducting an optimization study to demonstrate the feasibility of coupling the HIAD analysis tools with optimization techniques, the formulation of the complete optimization of the HIAD structure is worth considering. From the formulation of the complete optimization problem, optimization studies using a subset of variables, objectives and constraints can be formulated that are informative and tractable. The general formulation of the optimization problem for the full HIAD system is as follows,

Find   **X**,   Equation 6.5

Minimize $f(\mathbf{X})$

Subject to $h(\mathbf{X}) = 0$

$g(\mathbf{X}) \leq 0.$

$\mathbf{X}_{min} \leq X \leq \mathbf{X}_{max}.$

The vector **X** contains the design parameters that fully describe the HIAD system. A subset of parameters may include the braid angle, inflation pressure, cord locations and number of cords for each torus. It may also include the number of straps within a strap set, layout of straps, strap pretension and information about the strap cross-section. Further, the number of tori, minor diameters of tori and location of the cross-section of each torus may be included, to list a few parameters.

The objective functions, $f(\mathbf{X})$, may include goals to minimize the total structure mass or maximize the structural stiffness for any number of given load cases. The equality and inequality constraint functions, $h(\mathbf{X})$ and $g(\mathbf{X})$ respectively, may include limits on the required initial stiffness, maximum allowable displacement, minimum load at which the structure loses stiffness, or maximum allowable strap loads based on strength or indentation criteria, all for any number of given load cases. Constraint functions may also include constructability constraints, based on a maximum or minimum strap density or strap clearances. Frequency and dynamic constraints may also be included. It is also required that the design variable stay within reasonable and physical bounds, as indicated by the limits on the design parameters, **X**.

For a system as complex as the HIAD structure, the number of design variables, objective functions, constraint functions and load cases can quickly grow into a problem that is not currently tractable with available computational resources, analysis tools and solution techniques. For the current research an optimization problem was formulated that utilized a subset of design variables, along with a single objective function and nonlinear constraint. Any optimization problem will include a subset of design variables, since the complete optimization problem involves a very large (if not infinite) number of variables. An analysis that includes a subset of the full optimization problem is worthwhile because the optimization tools can be utilized to better understand the response drivers of the HIAD system.

There were a total of 14 design variables consisting of inflation pressure and the braid angle for each torus. The lower and upper bounds on the internal inflation pressure were 34 and 138 kPa respectively. The upper and lower bounds on the braid angle were 57° and 71° respectively. The goal of the optimization problem was to maximize the initial stiffness of the structure for the uniform, externally applied pressure load case. The initial stiffness was calculated as a tangent slope of the total Z direction reaction ($\sum F_z$) versus vertical displacement of the T6 torus (U_{z-T6}). As mentioned previously, the initial stiffness of the nominal configuration was 555 N/mm. Although the inflation pressure was allowed to vary for each torus, it was desired that the total mass of the gas not exceed the total gas mass for the nominal model (with each torus at 83 kPa of inflation pressure).

The total mass of the HIAD gas was estimated using the ideal gas law for each element,

$$pV = \frac{m}{M}RT. \hspace{4cm} \text{Equation 6.6}$$

Where p is the inflation pressure, V is the volume of the gas in the element, m is the mass of the gas in the element, M is molar mass of the gas, R is the universal gas constant and T is the temperature of the gas (in Kelvin scale). Equation 6.6 was rearranged for the gas mass of the element, m. The mass of each element was then summed to find the total gas mass ($mass$). Nitrogen (N_2) was utilized as the inflation gas ($M = 28.14 \ g/mol$). The temperature was assumed to be 295 K and the gas constant was taken as $8.31 \ \frac{m^3 Pa}{K \cdot mol}$.

The formulation of the optimization problem was,

$$Find \qquad \boldsymbol{X} = \left[\boldsymbol{p}_{T1 \ to \ T7}, \boldsymbol{\beta}_{T1 \ to \ T7} \right] \qquad \qquad \qquad \text{Equation 6.7}$$

$$Minimize \qquad k(\boldsymbol{X}) = -\frac{\partial \sum F_z}{\partial U_{z-T6}}$$

$$Subject \ to \qquad g(\boldsymbol{X}) = 1 - \frac{mass}{mass_0} \geq 0$$

$$34 \ kPa \leq \boldsymbol{p}_{T1 \ to \ T7} \leq 138 \ kPa$$

$$57° \leq \boldsymbol{\beta}_{T1 \ to \ T7} \leq 71°.$$

The total gas mass of the nominal structure ($mass_0$) was determined to be 6.4 kg. The stiffness objective used in Equation 6.7 was negative so that in minimizing the objective function, the stiffness was maximized.

A genetic algorithm (GA) was employed to find the design variables that satisfy the optimization problem as formulated in Equation 6.7. The real-coded GA algorithm documented in Goupee and Vel (2006) was utilized. This implementation is based on select algorithms proposed by Deb (2001). Although more efficient optimization tools may exist (Sigmund and Maute 2013), the GA was chosen for its robust nature and ease of implementation for the HIAD system. GAs have been successfully applied to the

156

optimization of engineering structures by many others (Poirier et al. 2013; Lohn 2008; Young 2013).

A total of 280 individuals were specified per generation (20 individuals per design variable). The analysis was terminated after 400 generations. The analysis was repeated three times and each iteration yielded comparable converged design variables (accounting for the stochastic nature of the GA). Figure 6.17 shows the convergence of the normalized solution for run 1. The normalized fitness is the percent change in stiffness from the nominal solution. The first run of the analysis is representative of all three runs and will be used for the purposes of analysis.
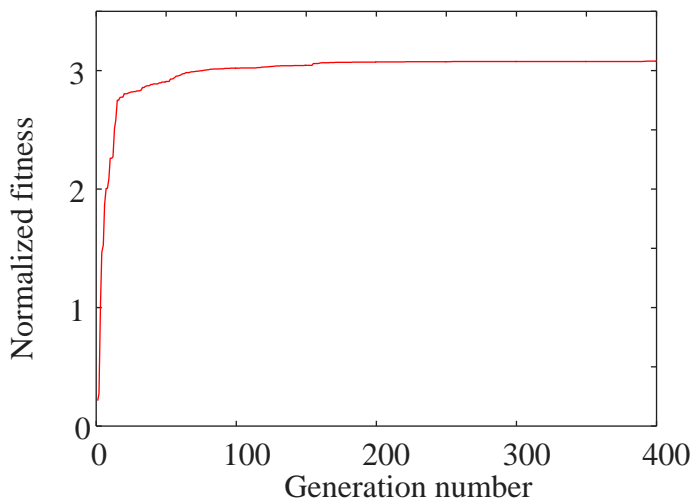
Figure 6.17. Convergence of solution (run 1).

As can be seen from Figure 6.17, a 3% increase in the initial, tangent stiffness was achieved. The total gas mass of the structure was maintained at 6.4 kg. Although the increase in stiffness was not substantial, the optimized design values did converge to informative final values. The distribution of inflation pressures and braid angles for tori T1 through T7 for all three optimization runs can be seen in Figure 6.18, below.

157
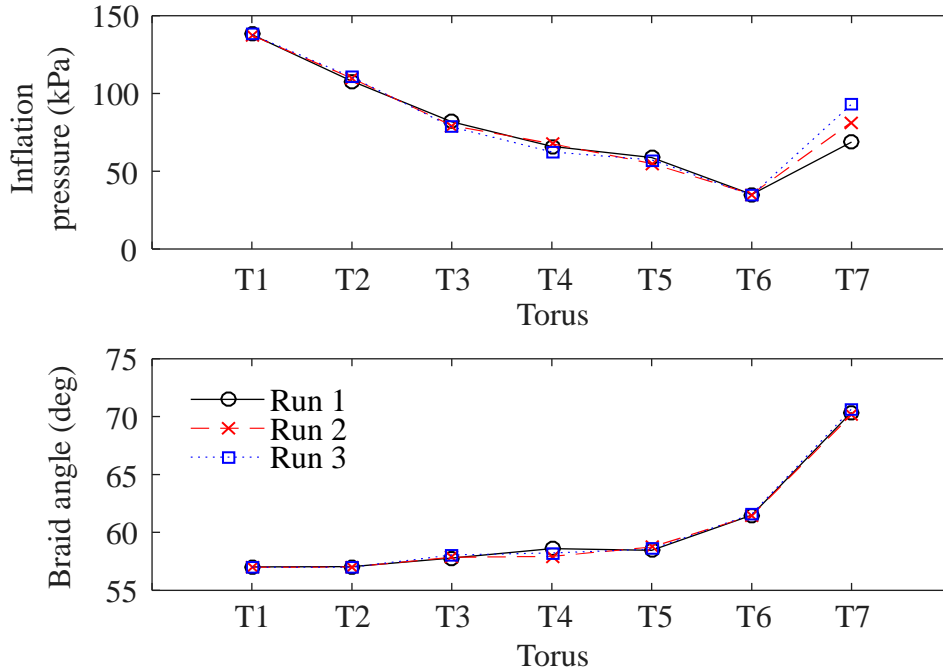
Figure 6.18. Converged design variables.

Clear trends can be seen for the distribution of both the internal inflation pressures and braid angles. Inner tori were more highly inflated than outer tori (with the exception of the shoulder torus, T7) and braid angle increased from the inner to outer tori. As the HIAD is loaded with a uniform external pressure, the aeroshell tends to deflect inward. The inward deflection both compresses and rotates the tori. While the outer tori are compressed to a greater extent, the inner tori experience a greater amount of rotation. It is reasonable that the converged solution increased inflation pressure while decreasing the braid angle of the inner tori (therefore increasing the shear stiffness of the tori), and increased the braid angle on the outer tori (therefore increasing the force in the cords and increasing axial stiffness). The design variables in all three runs converged to comparable values, with the exception of the T7 inflation pressure. The shoulder, T7, torus contributes minimally to the stiffness of the HIAD structure, and accommodates

much less gas than other tori because of the comparably small section diameter.

Although there is some spread in the final inflation pressure for the T7 torus, each run

produced a similar increase in inflation pressure from the T6 torus and may converge

further with the use of other solution techniques. The full load-deformation response of

both the nominal system and the converged solution are shown in Figure 6.19.
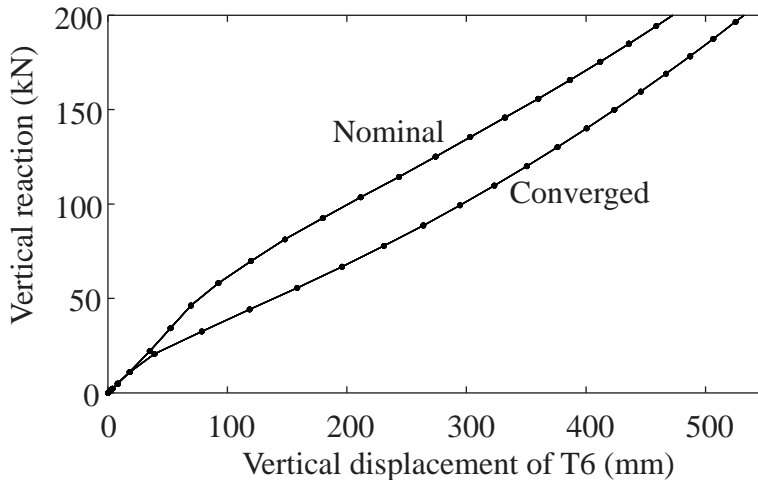
Figure 6.19. Load-deformation response of 6 meter HIAD configuration with uniform

pressure load, nominal and converged HIAD configurations.

While the converged solution met the optimization objectives and constraints, the load at

which the HIAD loses stiffness is significantly lower than for the nominal case. As the

outer tori become less inflated, the external load level required for the cords to lose their

prestrain due to inflation pressure decreases. Because the operational load is expected to

be approximately 130 kN, the converged solution may not be feasible as it would

experience larger deformations than the nominal HIAD. An additional, maximum

allowable deflection constraint could be added into the formulation of the optimization

problem in order to constrain the HIAD response from deforming significantly at

operational load levels.

The coupling of analysis and optimization tools can be used to better understand the response of the system, as demonstrated here for the HIAD structure. The structure can be further optimized and refined with the incorporation of additional constraints and modifications to the objective function. Whether trying to understand the influence of individual parameters or trying to refine the structural design, the coupling of analysis and optimization routines can be a powerful tool.

Chapter 7

SUMMARY, CONCLUSIONS AND FUTURE RESEARCH DIRECTIONS

In this chapter the current research is summarized and conclusions are drawn with respect to the applicability of the HIAD modeling methodologies that were developed. Potential directions for future research are also discussed, including logical extensions to the modeling and analysis methodologies and tools that were developed here.

7.1 Summary and Conclusions

The HIAD structure, under development by NASA researchers, has the potential to provide a decelerator with a significantly decreased mass when compared to traditional, rigid decelerators, and provide the required frontal area to effectively decelerate the sized payloads that will be required for future, human-scale missions. The HIAD system can be deflated and packed within the launch vehicle shroud for deployment on the way to the destination planet. Upon deployment the major diameter of the structure would be significantly greater than the diameter of the launch vehicle, an advantage over a comparable rigid decelerator that is constrained by the launch vehicle size. An important consideration with these inflatable, relatively compliant systems is the structural response during atmospheric reentry. A HIAD configuration that is too compliant may experience a global buckling failure as the structure is loaded, while a system that is over-designed may have more mass than is necessary. While ground development and testing of structural components and small-scale HIAD systems are important for understanding the structural response, human-scale HIAD systems may be larger than can be physically tested in an economic manner.

Numerical modeling techniques for the HIAD system are therefore important for understanding the structural response of full-scale HIAD systems. Others have developed continuum-based FE modeling methodologies for analyzing the HIAD system. These modeling tools, although able to capture the response of the HIAD system, are time consuming to develop, difficult to parameterize and computationally demanding to run because of the relatively compliant nature of the HIAD system, and the added complexities that arise when working with an inflatable system. In the current research a simplified, beam-based FE model approach for the analysis of inflatable members and the HIAD system was developed. The beam-based modeling approach incorporates the challenges that are encountered in analyzing an inflatable, textile system, such as the influence of internal inflation pressure, nonlinear material response, the loss of pretension due to inflation pressure, and the large deformations that occur as a result of having relatively compliant system.

A number of research goals and objectives were addressed in the current research.

- Material models for the braded shell that compose the HIAD tori and the internal axial reinforcing cords that give the members axial and bending rigidity were developed for both shell and beam-based FE modeling approaches.

- Computationally efficient, beam-based FE modeling and analysis methodologies were developed for use with the slender, inflatable members that that make up the HIAD system.

- The modeling methodology was validated at the component level by making comparisons to both straight tube and individual torus loading test data.

- The modeling methodology was further extended to model the full HIAD system, including the interaction between tori and the strap systems that attach tori to each other and to the rigid center-body.

- The full HIAD modeling tools were validated using pressure tub test data produced by NASA researchers.

- The modeling methodologies were extended and applied to the analysis of full-scale HIAD structures.

- Various methodologies for incorporating strap prestress were investigated.

- The structural response of a non-axisymmetric HIAD configuration was investigated that could be used to control the orientation of the inflatable body during atmospheric reentry. The modeling tools were demonstrated for non-uniform designs and non-uniform external loading.

- The beam-based modeling and analysis tools were coupled to optimization techniques to further understanding of the structural response drivers, and to demonstrate the feasibility of automating the structural design process.

The beam-based HIAD structural analysis methodologies that have been developed here are shown to be capable to capturing the structural response of the HIAD system. The modeling tools will complement the high fidelity, shell-based FE modeling tools under development by others. While the beam-based modeling tool can be used to efficiently explore the HIAD design space, explore various configurations and parameters, and perform trade, sensitivity and optimization studies, the shell-based modeling tools can be utilized for refined analysis once a final configuration has been down-selected.

7.2   **Applications and Future Research Directions**

There are a number of applications, potential research directions and extensions for the modeling tools and methodologies that build on the research detailed here. The first potential research extension is to apply the methodologies and tools developed in this dissertation to the analysis of other HIAD configurations.

HIAD parameterization

The modeling tools have been parameterized for the analysis of the HIAD system and can be used explore the HIAD design space and perform trade studies. HIAD design parameters include:

- Torus inflation pressure

- Torus minor radius

- Torus shell properties

- Braid angle

- Number of cords

- Cord location

- Cord response

- HIAD cone angle

- Location of torus cross-sections

- Strap connectivity

- Strap properties

- Strap prestress

- Magnitude of external pressure load

The modeling tools are currently parameterized for an axisymmetric HIAD system, based on the current state-of-the-art design. As the configuration of the HIAD evolves and additional features are required, the MATLAB based preprocessing routines will be relatively straight-forward to modify.

Application of the strap prestress analysis

As was discussed in Section 6.1, finding the initial, prestressed state of a HIAD system can be an involved process, even for the beam-based FE model. The complexity of the process is increased substantially when going from a beam to a shell-based FE modeling approach. In a shell-based modeling approach the pressurization step has to be included, and the analysis time to get to the preloaded state is prohibitively long to be able to apply the prestress search method that was developed here. Although more advanced form-finding analysis methodologies such as the dynamic relaxation or force-density methods (Adriaenssens et al. 2014) may decrease the analysis time for a single execution of the objective function, the prestress search methodology would still be prohibitively time consuming. The final results of the beam based strap prestress search methodology developed in Section 6.1 (level of strap prestrain and initial HIAD shape), could be used to inform the initial state of the shell-based FE model, eliminating the need for solving the computationally expensive inverse problem with the shell-based FE model. Likewise, the methodology could also be used to inform the initial strap lengths and torus configurations of an actual HIAD system, decreasing manufacturing complexity and time. Further exploration and validation of the initial state analyses could be performed by quantifying the shape and strap loads of just two tori before and after coupling the two tori together and tensioning the straps.

Incorporation of the cord hysteresis algorithm

The response of the torus axial reinforcing cords was shown to follow different loading-unloading paths, and was shown to be load history dependent (Chapter 2). A preliminary cord hysteresis algorithm was developed in Chapter 2 that was capable of tracking the load response by using the strain and strain history of the loading regime. In order to more accurately capture the response of a HIAD subjected to multiple loading cycles or for load cases where cords experience both loading and unloading, the cord hysteresis algorithm should be incorporated into the finite element framework. The force-strain lookup table that is currently utilized would be replaced by the cord hysteresis algorithm and input parameters would be updated every global FE iteration.

Incorporation of strap indentation response

At high loads or low inflation pressures individual straps that connect tori to each other and to the center-body may indent into the torus shell. This phenomenon was observed during out-of-plane torus testing conducted by Whitney (2016). This indentation has the potential to significantly influence the load deformation response of the HIAD at high loads. Strap indentation can be incorporated into the HIAD by tailoring the response of the link elements. A nonlinear moment-curvature relationship would be defined such that the gross response of the straps and indentation is captured. However, before the indentation response can be incorporated into the beam based HIAD modeling tools, the phenomenon must be better understood. This can be accomplished through parameterized indentation testing and a higher fidelity modeling approach.

HIAD shape morphing analyses

The benefits developing HIAD configurations that can actively control the orientation of lift and drag vectors relative to the HIAD body during reentry were discussed in Chapter 6, and shape morphing is a topic currently under investigation by NASA researchers. The beam-based FE modeling tools are a good candidate for assessing the structural response of these non-standard configurations. In addition to the tab configuration discussed in Chapter 6, another potentially feasible option is to use actuated cables on the HIAD center-body that connect to the outer torus, as shown in Figure 7.1. The load in individual cables would be controlled in order to morph the HIAD shape and control the aerodynamic response.
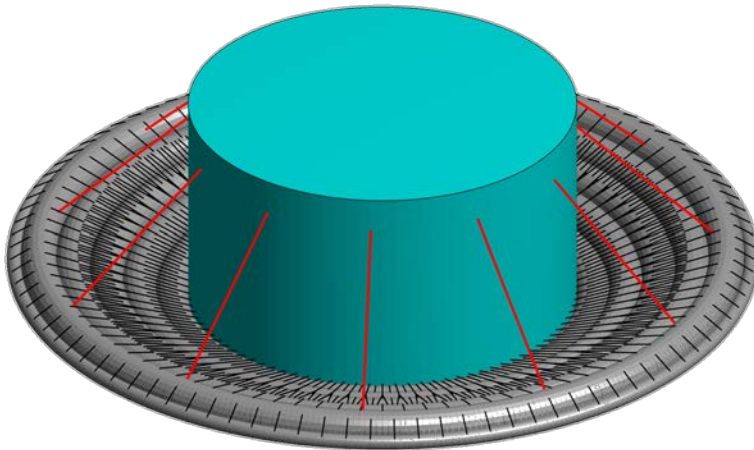
Figure 7.1: HIAD structure with center-body and cables for actively controlling the HIAD shape.

The beam-based FE modeling tools could incorporate these actuated cables to assess structural performance of the HIAD system. A computationally efficient beam-based model could also be incorporated into an experimental controls simulation for the purpose of developing a control algorithm.

167

Incorporation of the thermal protection system

The thermal protection system (TPS) covers the fore side of the HIAD system and

protects the tori and strap system from the high levels of heating encountered during

atmospheric reentry. The structural response of the HIAD system is influenced by the

TPS. In preliminary tests of the 3.7 meter HIAD system conducted by NASA

researchers, the presence of a TPS reduced radial strap loads by almost 40% (personal

communication, February 11, 2014). In addition to providing thermal protection, the TPS

may be tailored to increase the stiffness of the HIAD structure. The TPS could be

incorporated into the beam-based FE modeling approach with the inclusion of membrane

elements. The use of membrane elements would keep the computational overhead of the

modeling tools low (when compared with shell elements) and has the potential to

accurately capture the influence of the TPS.

Development of dynamic and fluid structure interaction analyses

To date, all analyses on the HIAD system using the beam-based modeling methodology

have been static analyses. Understanding the static response of the HIAD system is

critical and is the logical place to begin development of structural analysis

methodologies. However, the entry of the HIAD system into an atmosphere from orbit

may be influenced to a large extent by the structural dynamics of the system. In order to

perform dynamic analyses on the HIAD system using the beam-based modeling tools, the

mass and damping properties must be incorporated. The damping parameters would

likely be derived phenomenologically, as they are a result of a complex interaction with

the textile materials and friction between tori, straps and TPS. While straightforward

eigenvalue analyses could be quickly implemented to assess mode shapes and

frequencies, appropriate explicit or implicit time-stepping algorithms would also need to be implemented to determine the dynamic time-history response.

With the incorporation of mass and damping matrices the modeling tools could be applied to a number of additional analyses to better understand the response of the system. Fundamental mode shapes and frequencies of the HIAD system could be obtained. The HIAD system could be subjected to various dynamic loads representative of the reentry loading profile. The computationally efficient modeling tools could be coupled with CFD analyses or other fluid-structure interaction analyses in order to better understand how the deformed shape of the relatively compliant structure influences the fluid flow and loading on the system. Understanding the coupling between the HIAD structural shape and fluid flow around the structure is not an area that has been investigated to a high degree, but may be critical for the actual deployment during the mission.

Additional HIAD structural optimization analyses

There are significantly more opportunities for the development of structural optimization studies using the HIAD system. Whether or not the modeling tools are advanced to incorporate the extensions suggested in this section, the modeling and optimization tools can be used to further explore the HIAD design space and better understand the influence that various design parameters have on the response of the system. As optimization studies progress, refining the optimization methodologies may be worth considering in order to decrease analysis time. The optimization tools can also be incorporated into a larger-scale multi-disciplinary design optimization study, where the structural response is one of many parameters that is considered in the optimization of the global HIAD system.

BIBLIOGRAPHY

ABAQUS, ABAQUS Standard, User's Manual, Ver. 6.11, Dassault Systemes Inc., Paris, France, 2014.

Adriaenssens, S., Block, P., Veenendaal, D., and Williams, C. (2014). *Shell structures for architecture: form finding and optimization*. Routledge.

Adriaenssens, S., Block, P., Veenendaal, D., and Williams, C. (2014). *Shell structures for architecture: form finding and optimization*. Routledge.

Apedo, K. L., Ronel, S., Jacquelin, E., Bennani, A., and Massenzio, M. (2010). "Nonlinear finite element analysis of inflatable beams made from orthotropic woven fabric." *International Journal of Solids and Structures*, *47*(16), 2017-2033.

Argyris, J. H., and Symeonidis, S. (1981). Nonlinear finite element analysis of elastic systems under nonconservative loading-natural formulation. Part I. Quasistatic problems. *Computer Methods in Applied Mechanics and Engineering*, *26*(1), 75-123.

Berger, K., Horta, L., and Taleghani, B. (2004). Static testing of an inflatable/rigidizable hexapod structure. In *45th AIAA/ASME/ASCE/AHS/ASC Structures, Structural Dynamics & Materials Conference* p. 1801.

Brayley, K., Davids, W. G., and Clapp, J. D. (2012). "Bending Response of Externally Reinforced, Inflated, Braided Fabric Arches and Beams." *Construction and Building Materials* 30, 50-58.

Brown, G., Haggard, R., and Norton, B. (2001). "Inflatable structures for deployable wings." *Proc. 16th AIAA Aerodyn. Decelerator Syst. Technol. Conf. Seminar,* Boston, MA, 19-26.

Cassell, A. M., Swanson, G. T., Quach, B. T., Kushner, L. K., Brown, J. D., Kazemba, C. D., and Cheatwood, F. M. (2013). "Design and execution of the hypersonic inflatable aerodynamic decelerator large-article wind tunnel experiment." *Proc. AIAA Aerodynamic Decelerator Systems Technology Conference*, Daytona Beach, FL.

Cavallaro, P. V, Johnson M. E, and Sadegh A. M. (2003). "Mechanics of Plain-Woven Fabrics for Inflated Structures." *Composite Structures*, 61(4), 375-393.

Clapp, J. D. (2017). Structural behavior of inflatable, reinforced, braided tubular members (Unpublished doctoral dissertation). University of Maine, Orono, Maine.

Clapp, J. D., Davids, W. G., Goupee, A. J., and Young, A. C. (2016a). "Experimental Determination of Inflatable, Braided Tube Constitutive Properties." *Strain*, 52, 148–161.

Clapp, J. D., Young, A. C., Davids, W. G., and Goupee, A. J. (2016b). "Bending response of reinforced, inflated, tubular braided fabric structural members." *Thin-Walled* Structures, 107, 415-426.

Clapp, J. D., Young, A. C., Davids, W. G., and Goupee, A. J. (2015). "Structural response of hypersonic inflatable aerodynamic decelerator braided tube components and elements." Proc. *AIAA Aerodynamic Decelerator Systems Technology Conference*, Daytona Beach, FL.

Clarke, M. J., and Hancock, G. J. (1990). "A study of incremental-iterative strategies for non-linear analyses." *International Journal for Numerical Methods in Engineering*, *29*(7), 1365-1391.

Crisfield, M. A. (1990). "A consistent co-rotational formulation for non-linear, three-dimensional, beam-elements." *Computer methods in applied mechanics and engineering*, *81*(2), 131-150.

Davids, W. G. (2009). "In-plane load-deflection behavior and buckling of pressurized fabric arches." *Journal of Structural Engineering*, *135*(11), 1320-1329.

Davids, W. G., and Zhang, H. (2008). "Beam finite element for nonlinear analysis of pressurized fabric beam–columns." *Engineering Structures,* 30(7), 1969-1980.

Davis, S., and Caldwell, D. G. (2006). Braid effects on contractile range and friction modeling in pneumatic muscle actuators. *The International Journal of Robotics Research*, *25*(4), 359-369.

De Souza, R. M. (2000). *Force-based finite element for large displacement inelastic analysis of frames* (Doctoral dissertation). University of California, Berkeley, CA.

Deb, K., (2001). *Multi-objective Optimization Using Evolutionary Algorithms*. Wiley, Chichester, England.

Elsabbagh, A. (2015). "Nonlinear finite element model for the analysis of axisymmetric inflatable beams." *Thin-Walled Structures*, *96*, 307-313.

Evans, J. T., and Gibson, A. G. (2002). "Composite angle ply laminates and netting analysis." *Proceedings of the Royal Society of London A: Mathematical, Physical and Engineering Sciences*, *458*, 3079-3088.

Fichter, W. B. (1966). *A theory for inflated thin-wall cylindrical beams.* National Aeronautics and Space Administration.

Goupee, A. J., and Vel, S. S. (2006). "Two-dimensional optimization of material composition of functionally graded materials using meshless analyses and a genetic algorithm." *Computer methods in applied mechanics and engineering*, *195*(44), 5926-5948.

Guo, X., Li, Q., Zhang, D., and Gong, J. (2015). Structural Behavior of an Air-Inflated Fabric Arch Frame. *Journal of Structural Engineering*, *142*(2), 04015108.

Hibbeler, R. C. (2015). *Engineering Mechanics: Statics*. Pearson.

Hibbett, Karlsson, & Sorensen. (2014). *ABAQUS/standard: User's Manual* (Vol. 1).

Hughes, S. J., Cheatwood, F. M., Dillman, R. A., Wright, H. S., Del-Corso, J. A., and Calomino, A. M. (2011). "Hypersonic Inflatable Aerodynamic Decelerator (HIAD) Technology Development Overview," *Proc. AIAA Aerodynamic Decelerator Systems Technology Conference*, Dublin, Ireland.

Jha, A. K. (2002). Vibration analysis and control of an inflatable toroidal satellite component using piezoelectric actuators and sensors (Doctoral dissertation, Virginia Tech).

Johnson, R. K., Cheatwood, F. M., Calomino, A. M., Hughes, S. J., Korzun, A. M., DiNonno, J. M., Lindell, M. C., and Swanson, G. T. (2016). "HIAD Advancements and Extension of Mission Applications." *Proc. 13th International Planetary Probe Worksho*p, Laurel, MD.

Kabche, J. P., Peterson, M. L., & Davids, W. G. (2011). "Effect of inflation pressure on the constitutive response of coated woven fabrics used in airbeams." *Composites Part B: Engineering*, 42(3), 526-537.

Le van, A., and Wielgosz, C. (2005). "Bending and buckling of inflatable beams: some new theoretical results." *Thin-Walled Structures*, *43*(8), 1166-1187.

Le van, A., and Wielgosz, C. (2007). "Finite element formulation for inflatable beams." *Thin-walled structures*, *45*(2), 221-236.

Levine, J. (2017). "Loads tests validate design of hypersonic inflatable aerodynamic decelerator." *NASA,* <https://www.nasa.gov/centers/armstrong/Features/HIAD_decelerator_system.html> (Feb. 17, 2017).

Li, L., Gonyea, K. C., and Braun, R. D., (2015). "Finite Element Analysis of the Inflatable Re-Entry Vehicle Experiment." *Proc. AIAA Structures, Structural Dynamics, and Materials Conference*, Kissimmee, FL.

Li, Q., Guo, X., Gong, J., Qing, Q., and Li, Z. (2016). Experimental deployment behavior of air-inflated fabric arches and a full-scale fabric arch frame. *Thin-Walled Structures*, *103*, 90-104.

Lindell, M. C., Hughes, S. J., Dixon, M., and Willey, C. E. (2006). "Structural analysis and testing of the Inflatable Re-entry Vehicle Experiment (IRVE)." Proc. *AIAA Structures, Structural Dynamics, and Materials Conference,* Newport, RI.

Lohn, J., Linden, D., and Hornby, G. (2008). "Advanced antenna design for a NASA small satellite mission," in Proceedings of the 22nd AIAA/USU Conference on Small Satellites, Logan, Utah

Lyle, K. H. (2014). "Preliminary Structural Sensitivity Study of Hypersonic Inflatable Aerodynamic Decelerator Using Probabilistic Methods." NASA Report.

Lyle, K. H. (2015). "Comparison of Analysis with Test for Static Loading of Two Hypersonic Inflatable Aerodynamic Decelerator Concepts." NASA Report.

Marini, A., and Spacone, E. (2006). "Analysis of reinforced concrete elements including shear effects." *ACI Structural Journal*, *103*(5), 645-655.

MathWorks (2015) *MATLAB v. 2015b*. MathWorks, Inc., Natick, MA.

Molloy, S. J., Plaut, R. H., and Kim, J. Y. (1999). Behavior of pair of leaning arch-shells under snow and wind loads. *Journal of engineering mechanics*, *125*(6), 663-667.

Neuenhofer, A., and Filippou, F. C. (1997). "Evaluation of nonlinear frame finite-element models." *Journal of Structural Engineering*, *123*(7), 958-966.

Neuenhofer, A., and Filippou, F. C. (1998). "Geometrically nonlinear flexibility-based frame finite element." *Journal of Structural Engineering*, 124(6), 704-711.

Nguyen, Q. T., and Thomas, J. C. (2015). "Inflation and bending of an orthotropic inflatable beam." *Thin-Walled Structures*, *88*, 129-144.

Pazhooh, M. D., Dokainish, M. A., and Ziada, S. (2011a). Experimental Modal Analysis of an Inflatable, Selfrigidizing Toroidal Satellite Component. In *Experimental and Applied Mechanics, Volume 6* (pp. 187-199). Springer New York.

Pazhooh, M. D., Dokainish, M. A., and Ziada, S. (2011b). Finite element modal analysis of an inflatable, self-rigidizing toroidal satellite component. In *Experimental and Applied Mechanics, Volume 6* (pp. 281-288). Springer New York.

Plaut, R. H., Goh, J. K., Kigudde, M., and Hammerand, D. C. (2000). Shell analysis of an inflatable arch subjected to snow and wind loading. *International journal of solids and structures*, *37*(31), 4275-4288.

Poirier, J. D., Vel, S. S., and Caccese, V. (2013). "Multi-objective optimization of laser-welded steel sandwich panels for static loads using a genetic algorithm." *Engineering Structures*, *49*, 508-524.

Raouf, R. A., and Palazotto, A. N. (1996). Nonlinear dynamics of unidirectional, fiber-reinforced tori. *Journal of engineering mechanics*, *122*(3), 271-276.

Roekens, J., De Laet, L., Mollaert, M., & Luchsinger, R. (2016). Experimental and numerical investigation of a tensairity arch. *Thin-Walled Structures*, *105*, 112-120.

Roychowdhury, S., and DasGupta, A. (2015a). On the response and stability of an inflated toroidal membrane under radial loading. *International Journal of Non-Linear Mechanics*, *77*, 254-264.

Roychowdhury, S., and DasGupta, A. (2015b). Inflating a flat toroidal membrane. *International Journal of Solids and Structures*, *67*, 182-191.

Sigmund, O., and Maute, K. (2013). "Topology optimization approaches." *Structural and Multidisciplinary Optimization*, *48*(6), 1031-1055.

Smalley, K., Tinker, M., and Taylor, W. (2001). Structural modeling of a five-meter thin film inflatable antenna/concentrator with rigidized support struts. In *19th AIAA Applied Aerodynamics Conference* p. 1412.

Spacone, E., Filippou, F., and Taucer, F. (1996a). "Fibre beam-column model for non-linear analysis of R/C frames: Part I. Formulation." *Earthquake Engineering and Structural Dynamics*, *25*(7), 711-725.

Spacone, E., Filippou, F., and Taucer, F. (1996a). "Fibre beam-column model for non-linear analysis of R/C frames: Part I. Formulation." *Earthquake Engineering and Structural Dynamics*, *25*(7), 711-725.

Spacone, E., Filippou, F., and Taucer, F. (1996b). "Fibre beam-column model for non-linear analysis of R/C frames: Part II. Applications." *Earthquake engineering and structural dynamics*, *25*(7), 727-742.

Swanson, G. T., Kazemba, C. D., Johnson, R. K., Hughes, S. J., Calomino, A. M., Cheatwood, F. M., Cassell, A. M., Anderson, P., and Lowery, A. (2015). "Overview of the 2nd Gen 3.7 m HIAD Static Load Test." *Proc., 12th Int. Planetary Probe Workshop*, NASA, Washington, DC.

Tamadapu, G., and DasGupta, A. (2013). Finite inflation analysis of a hyperelastic toroidal membrane of initially circular cross-section. *International Journal of Non-Linear Mechanics*, *49*, 31-39.

Tamadapu, G., and DasGupta, A. (2014). Effect of curvature and anisotropy on the finite inflation of a hyperelastic toroidal membrane. *European Journal of Mechanics-A/Solids*, *46*, 106-114.

Taucer, F., Spacone, E., & Filippou, F. C. (1991). A fiber beam-column element for seismic response analysis of reinforced concrete structures (Vol. 91, No. 17). Berkekey, California: Earthquake Engineering Research Center, College of Engineering, University of California.

Veldman, S. L., and Vermeeren, C. A. J. R. (2001). "Inflatable Structures in Aerospace Engineering-An Overview." *Proc. European Conference on Spacecraft Structures, Materials and Mechanical Testing*, Noordwijk, Netherlands, 93-98.

Veldman, S. L., Bergsma, O. K., Beukers, A., and Drechsler, K. (2005). "Bending and optimisation of an inflated braided beam." *Thin-Walled Structures*, *43*(9), 1338-1354.

Verge, A. S. (2006). "Rapidly deployable structures in collective protection systems." Army Soldier and Biological Chemical Command, Natick, MA.

Wang, C., Tan, H., and Du, X. (2009). "Pseudo-beam method for compressive buckling characteristics analysis of space inflatable load-carrying structures." *Acta Mechanica Sinica*, *25*(5), 659-668.

Weeks, G. E. (1967). Buckling of a pressurized toroidal ring under uniform external loading. National Aeronautics and Space Administration.

Whitney, D. J. (2016) Experimental methods and practices for the study of toroidal inflated, braided fabric members (Master's Thesis). University of Maine, Orono, Maine.

Wright, H., Cutright, A., Corliss, J., Bruce, W., Trombetta, D., Mazaheri, A. R., Coleman, M., Olds, A., and Hancock, S. (2012). "HEART flight test overview." *Proc. 9th International Planetary Probe Worksho*p, Toulouse, France.

Young, A. C. (2013). Investigations into the use of a composite tower on floating offshore wind turbine platforms (Master's Thesis). University of Maine, Orono, Maine.

Young, A. C., Davids, W. G., Goupee, A. J., and Clapp, J. D. (2017a). "Computationally Efficient Finite-Element Modeling of Braided Inflatable Structural Members with Axial Reinforcing." *Journal of Engineering Mechanics*, 143(6).

Young, A. C., Davids, W. G., Whitney, D. J., Clapp, J. D. and Goupee, A. G. (2017b). "Structural testing and analysis of a braided, inflatable fabric torus structure." *Acta Astronautica*, 139, 189-200.

Zu, L. (2012). *Design and optimization of filament wound composite pressure vessels* (Doctoral dissertation). TU Delft, Delft, Netherlands.

BIOGRAPHY OF THE AUTHOR

Andrew Young was born in Boston, Massachusetts on January 31, 1983. He graduated from Poland Regional High School in Poland Springs, Maine in 2001. After high school Andrew pursued a career in carpentry, cabinet and furniture making and worked in the Midcoast region of Maine until 2008. He graduated from the University of Maine's Civil and Environmental Engineering program *summa cum laude* with a Bachelor's degree in December of 2011. In December of 2013 Andrew obtained a Master's of Science degree from the University of Maine's Civil and Environmental Engineering program with the thesis '*Investigations into the use of a composite tower on floating offshore wind turbine platforms*'. As a Doctor of Philosophy student Andrew was a NASA Space Technology Research Fellow. He is a candidate for the Doctor of Philosophy degree in Civil Engineering from the University of Maine in August of 2017.